Liquid Sodium Stratification Prediction and Simulation in a Two-Dimensional Slice

Dual Degree Technische Universität Darmstadt and Virginia Polytechnic Institute and State University

Master-Thesis von Robert Langhans aus Frankfurt am Main

Tag der Einreichung: 22. Januar 2017

1. Gutachten: Prof. Yang Liu
2. Gutachten: Prof. Manfred Hampe
3. Gutachten: Prof. Jan-Helge Bøhn
4. Gutachten: Prof. Michael Schäfer

TECHNISCHE UNIVERSITÄT DARMSTADT

Fachbereich Maschinenbau
in Collaboration with the Mechanical Engineering Department at
Virginia Polytechnic Institute and State University

Liquid Sodium Stratification Prediction and Simulation in a Two-Dimensional Slice
Dual Degree Technische Universität Darmstadt and Virginia Polytechnic Institute and State University

Vorgelegte Master-Thesis von Robert Langhans aus Frankfurt am Main

1. Gutachten: Prof. Yang Liu
2. Gutachten: Prof. Manfred Hampe
3. Gutachten: Prof. Jan-Helge Bøhn
4. Gutachten: Prof. Michael Schäfer

Tag der Einreichung: 22. Januar 2017

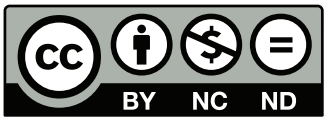

Erklärung zur Master-Thesis

Hiermit versichere ich, die vorliegende Master-Thesis ohne Hilfe Dritter nur mit den angegebenen Quellen und Hilfsmitteln angefertigt zu haben. Alle Stellen, die aus Quellen entnommen wurden, sind als solche kenntlich gemacht. Diese Arbeit hat in gleicher oder ähnlicher Form noch keiner Prüfungsbehörde vorgelegen. In der abgegebenen Thesis stimmen die schriftliche und elektronische Fassung überein.

Darmstadt, den 22. Januar 2017

(Robert Langhans)

Liquid Sodium Stratification Prediction and Simulation in a Two-Dimensional Slice

TECHNISCHE UNIVERSITÄT DARMSTADT

Master Thesis
Starting Date: August 22, 2016
Co-Advisor Virginia Tech: Prof. Yang Liu
Co-Advisor TU Darmstadt: Prof. Manfred Hampe

Project Description

To better understand the complicated, coupled thermal and flow phenomena in the upper plenum of a sodium fast reactor (SFR), the Multiphase Flow and Thermal-hydraulics Lab (MFTL) at Virginia Tech is planning to construct a scaled down test facility of the upper plenum. The Advanced sodium-cooled Fast Reactor (AFR-100) design developed by Argonne National Lab will serve as the design basis. The test facility will use liquid gallium as the test fluid to avoid the experimental and safety complications associated with sodium. The facility will also allow the investigation of both steady-state and transient conditions over a wide range of Reynolds and Richardson numbers.

The goal of this thesis is to understand the flow and stratification patterns during normal operation and special circumstances such as start-up/ shut-down, and accident conditions. The focus is on predicting the mixing and heat transfer in low Prandtl number (liquid metal) flows though Computational Fluid Dynamics (CFD) simulations. Further, insight from the simulations will be used to design the test facility in future projects.

The thesis will serve as a guideline for experiment planning, and provide data for later validation by experimental studies.

Tasks

- Extensive literature survey of previous upper plenum CFD simulations

- Perform CFD simulations for various steady and transient conditions using FLUENT software
- Analyze the resulting data, and document the results and conclusions

Approved/ accepted by:

_____	_____	_____
Prof. Manfred Hampe	Prof. Yang Liu	Robert Langhans

Abstract

In light of rising global temperatures and energy needs, nuclear power is uniquely positioned to offer carbon-free and reliable electricity. In many markets, nuclear power faces strong headwinds due to competition with other fuel sources and prohibitively high capital costs. Small Modular Reactors (SMRs), such as the proposed Advanced Fast Reactor (AFR) 100, have gained popularity in recent years as they promise economies of scale, reduced capital costs, and flexibility of deployment. Fast sodium reactors commonly feature an upper plenum with a large inventory of sodium. When temperatures change due to transients, stratification can occur. It is important to understand the stratification behavior of these large volumes because stratification can counteract natural circulation and fatigue materials.

This work features steady-state and transient simulations of thermal stratification and natural circulation of liquid sodium in a simple rectangular slice using a commercial CFD code (ANSYS FLUENT). Different inlet velocities and their effect on stratification are investigated by changing the inlet geometry. Stratification was observed in the two cases with the lowest inlet velocities. An approach for tracking the stratification interface was developed that focuses on temperature gradients rather than differences. Other authors have developed correlations to predict stratification in three dimensional enclosures. However, these correlations predict stratified conditions for all simulations even the ones that did not stratify. The previous models are modified to reflect the two-dimensional nature of the flow in the enclosure. The results align more closely with the simulations and correctly predict stratification in the investigated cases.

Contents

List of Figures

List of Tables

List of Abbreviations

AFR Advanced Fast Reactor

ANL Argonne National Laboratory

BWR Boiling Water Reactor

CEA Alternative Energies and Atomic Energy Commission

CFD Computational Fluid Dynamics

CRP Coordinated Research Project

DRACS Direct Reactor Auxiliary Cooling System

FH Flow Holes

GDP Gross Domestic Product

IAEA International Atomic Energy Agency

IGCAR Indira Gandhi Centre for Atomic Research

IHX Intermediate Heat Exchanger

IPCC Intergovernmental Panel on Climate Change

IPPE Institute of Physics and Power Engineering

JAEA Japan Atomic Energy Agency

KAERI Korea Atomic Energy Research Institute

LWR Light Water Reactor

MFTL Multiphase Flow and Thermal-hydraulics Lab

PDE Partial Differential Equation

PWR Pressurized Water Reactor

RSM Reynolds Stress Model

SFR Sodium Fast Reactor

SKE Standard k-ϵ Turbulence Model

SMR Small Modular Reactor

SST Menter's Shear Stress Transport Model

UCS Upper Core Structure

UIS Upper Instrumentation Structure

ULOF Unprotected Loss of Flow

UF Univeristy of Fukui

1 Introduction

Electric energy is fundamental to the way of life as we know it today. From traffic lights to fridges, air-conditioners, lights, and many more applications, electricity sustains basic human needs and provides comfort. Electricity use and Gross Domestic Product (GDP) have been found to be interconnected in multiple studies [1, 2]. As developing countries turn into developed countries, their electricity demand rises and must be met by an equal amount of production. Today, this increase in production will likely be met by fossil fueled generation, especially coal. Global population growth, along with plans to electrify the transportation sectors of developed countries, will further increase global electricity demand.

In light of rising global temperatures, the Intergovernmental Panel on Climate Change (IPCC) has concluded that increasing reliance on fossil fuels will have dramatic impacts on the global climate. A rise of 2 Kelvin has been postulated as the threshold value beyond which serious consequences can be expected [3, 4]. Many countries around the world have agreed to reduce emissions of green house gases, most notably carbon dioxide, in an effort to slow climate change and prevent some of its negative effects [3,5]. A rising demand coupled with the desire to reduce carbon dioxide emissions challenges the status quo and requires changes in all aspects of energy consumption (transportation, heating, electricity generation etc.). Numerous solutions such as renewables (solar, wind, hydroelectric), carbon capture and storage, and nuclear have been suggested to reduce the carbon footprint of electricity generation [3].

Hydroelectric generation has been used to generate electricity for a long time and continues to provide largest amount of carbon-free energy [6]. The share of hydroelectric generation is limited by local geography but has seen significant increases in capacity over the last decade especially in non-OECD countries. Hydropower is able to ramp up and down quickly making it suitable for implementation along other, more intermittent renewables. Additionally, pumped hydro is one of the most mature methods of energy storage on the market [4]. However, controversies remain over population resettlements to accommodate large reservoirs and the impact of dams on wildlife.

Solar and wind are also counted among the carbon-free energy sources and have seen large increases in market share over the last decade. These increases are due to environmental concerns, falling investment costs, and favorable regulatory structures [4]. However, both sources are considered intermittent meaning they do not supply a constant amount of electricity. This intermittency is intrinsic to solar and wind generation as both sunshine and wind vary over the course of a day, as well as seasonally. These fluctuations need to be compensated by other sources of electricity or smoothed by appropriately sized storage facilities. Both approaches are not without controversy as they require over capacities. Nevertheless, it has been shown that both can successfully be integrated into existing generation networks to reduce the carbon intensity of electricity generation. Some technologies such as Concentrated Solar Power aim to incorporate solutions to these problems through thermal storage tanks [4].

The decline in natural gas prices due to hydraulic fracturing (“fracking”) has led to an increase in demand for natural gas, and increases the incentive for coal-to-gas switching [4]. The substitution of coal generation with gas generation can reduce carbon emissions by approximately one half and also releases fewer or no emissions of heavy-metals, sulfur, and particulates. However, some, if not all, of these benefits are cancelled by methane leaks during production and transmission due to the much higher global warming potential of methane compared to carbon dioxide [4, 7].

Nuclear power provides base load power and trails only hydropower in terms of low-carbon electricity production [4]. Contrary to hydropower, nuclear energy relies on an exhaustible fuel but is easily scalable and is less dependent on local geography. Nuclear power plants have also been suggested for direct and indirect hydrogen production and seawater desalination [8]. The biggest hurdles for nuclear power

today are the unsolved waste-disposal problem, public opposition, high capital costs, and competition from cheap natural gas [9].

In light of increasing global energy demand and concerns about climate change, many countries are increasing their share of renewable electricity generation. Nuclear energy has been suggested as a complement to renewable energy to provide dependable energy [10, 11]. However, most of the growth in electricity demand is likely to come from developing countries where no nuclear infrastructure exists. Further, it is less likely for these countries to have utility companies that are large enough to shoulder the initial investment of a nuclear power plant. For these reasons, Small Modular Reactors (SMRs) have been developed with the explicit intention of lowering the barriers of entry for nuclear power generation, as well as decreasing the necessary capital [12, 13]. One of these SMRs is the AFR-100 reactor developed by Argonne National Laboratory (ANL).

The Nuclear Engineering Program at Virginia Tech is planning to build a test facility to investigate the thermal hydraulics of the upper plenum of the AFR in collaboration with ANL. Computational Fluid Dynamics (CFD) simulations will be performed to identify experiments of particular interest and to validate the CFD results when the test facility becomes available. This work documents the CFD analyses that will form the basis for later experiments.

2 Background

2.1 Nuclear Energy

The first commercial nuclear power reactor was built in Shippingport, Pennsylvania in 1957, following successful earlier construction of multiple reactors for plutonium production during the Second World War. The United States Navy was heavily involved in the construction of the Shippingport reactor which was chosen to be a pressurized light water reactor similar to those used by the Navy [14]. The 1950s and 1960s were a time of public enthusiasm about nuclear power brought on in part by the belief that nuclear reactors would supply almost endless energy that would be "too cheap to meter" [15]. Although these aspirations later proved unrealistic, 14 new reactors were ordered in the US between 1953 and 1960. Nine of these reactors were Light Water Reactors (LWRs), while the other five were of various other designs [14]. The 1960s and '70s continued to be a period of rapid expansion of nuclear power driven by a positive attitude towards the new technology [14, 15]. Although other reactor designs and types were investigated and received plenty of attention, the LWR continued to be the most prevalent reactor type [15].

Today, LWRs remain the most common reactor with a market share of around 82 %, followed by Heavy Water Reactors with 11 %. The majority of the LWRs are Pressurized Water Reactors (PWRs) (77.5 %), the rest are Boiling Water Reactors (BWRs) [9]. It can be speculated that the early momentum supplied to LWRs, and especially PWRs, by the Shippingport reactor is responsible for this distribution. Significant operation and construction experience has been gained for these types of reactors, solidifying their commanding market share. However, other reactors types have been tried, tested, and built successfully. Today, the only commercially operating reactors in Germany and the US are LWRs [16, 17].

In 2013, the share of nuclear power of total energy generation was approximately 10.6 % globally [6]. However, there are wide variations across countries, from France with 76.3 % to Iran with 1.3 %. Japan's share was even lower at 0.5 % due to the Fukushima Daiichi accident and subsequent reviews (2015 data) [18]. Future expectations also vary widely across the globe. Germany has decided to permanently cease nuclear electricity generation in 2022 [19]. In the US, a numbers of reactors are scheduled to close while only a few are being built. Reasons for shutdowns are usually unfavorable economics in unregulated markets due to low natural gas prices. China on the other hand is rapidly expanding its nuclear capacity with 22 reactors under construction. China's expansion of nuclear power is due to sustained electrification of the country coupled with public health concerns about coal pollutants, China's main source of energy [4, 16, 17].

Other developing countries are looking into nuclear power for the same reasons: a growing demand for electricity in light of global efforts to curb climate change. Unlike China, these countries often lack the resources and demand to build plants that produce upwards of 1000 MWe (Megawatts electric) and cost billions of dollars [10].

2.1.1 Fast Reactors

The neutron spectrum in nuclear reactors is usually divided into two broad categories: thermal and fast. Energies below 0.1 eV are considered thermal, as they roughly translate to the kinetic energy of neutrons at ambient temperatures. All neutrons with energies above 0.1 eV, and thus higher velocities, are considered fast. Neutrons born in fission are released with energies on a continuous spectrum with an average energy of 1.98 MeV and a most likely energy of 0.73 MeV.

Since fission neutrons are released at fast energies, they must be slowed to lower energies in thermal reactors. This so called moderation is achieved by collisions with surrounding nuclei. The lighter the

collision partner, the more energy is lost by the incident neutron. Good moderators, in addition to being light, should have a low capture cross-section to reduce the number of neutrons lost in non-fission events. Commercial thermal reactors overwhelmingly use light water or graphite as moderators due to their favorable properties. In most light water reactors, water fulfills the dual tasks of moderation and heat removal. In contrast, fast reactors utilize neutrons at fast energies and thus do not require a moderator. In fact, special care is taken to avoid materials that reduce neutron energies. The neutron economy is significantly impacted by the incident neutron energy because it affects important properties such as the capture cross-section, the average number of neutrons released during fission, the type of fission products, and the fission neutron energy [20].

Nuclear reactors can be designed to yield a surplus of neutrons beyond what is needed to sustain a chain reaction. These neutrons can then be used to transform non-fissile nuclei into fissile nuclei through a process called "breeding". One example of such a reaction is the transformation of uranium-238 to plutonium-239. The process and subsequent decay steps are shown in Eqn. 2.1. A similar reaction takes place in the thermal spectrum for thorium-232, resulting in uranium-233 [20].

$$^{238}\mathrm{U}(\mathrm{n},\gamma)^{239}\mathrm{U} \xrightarrow{\beta^-} {}^{239}\mathrm{Np} \xrightarrow{\beta^-} {}^{239}\mathrm{Pu} \tag{2.1}$$

Breeder reactors were once hailed as the solution to the world's energy problem. The promise of creating more fuel than is used has captured the imagination of engineers and the public alike. Since its conception in the 1940s the fast breeder reactor has received much attention and development, although not on the same level as light water reactors [15]. During the time of rapid expansion of nuclear power in the 1960s and 1970s it was expected that the uranium-235 resources would be exhausted quickly. Breeder reactors that could run on depleted or natural uranium would be able to extend the uranium supply almost indefinitely. These predictions about uranium have proven false for two reasons. First, the expansion of nuclear power was much slower than expected leading to reduced demand. Second, the discovery of additional uranium resources drastically increased the amount of available uranium. Combined, these factors lead to the relatively low price of uranium today of just $ 71.76 per kilogram uranium ($ 27.60 per pound of U_3O_8) [21,22]. Both, low uranium prices and an abundance of uranium have led to decreased urgency in the development of breeder reactors. However, strong research interest remains around breeding especially in India where abundant thorium resources can be converted to fissile uranium-233 [23].

Numerous concepts for fast reactors have been proposed and some have been tested extensively. Liquid sodium is the coolant of choice for most fast reactors because of its low neutron capture cross-section and excellent heat transfer properties. Hejzlar et al. compared four different fast reactor coolants (liquid salt, liquid lead, liquid sodium, supercritical CO_2) and concluded that designs using liquid sodium would have the highest power density, specific power, and best natural convection characteristics of the investigated concepts. All liquid cooled reactors were found to withstand unprotected loss of heat sink, unprotected loss of flow, and unprotected overpower accidents safely. Unprotected accidents are those in which no control rods are inserted to decrease reactor power. Sodium poses some operational problems because it reacts violently with water, and, more slowly, with air. Safety concerns usually necessitate an intermediate loop that separates the irradiated primary sodium from water, preventing sodium fires involving radioactive species. This intermediate loop leads to an efficiency penalty that reduces the thermal efficiency of sodium reactors below that of the other investigated coolants. Additionally, liquid sodium is opaque which complicates inspection and maintenance operations [24]. Years of operating experience have shown that the operational problems with sodium cannot be neglected and have led to much lower capacity factors than those encountered in LWRs. More operating experience and further design improvements will likely increase capacity factors as has been the case with LWRs which increased

their capacity factors over time [21].

Sodium fast reactors are generally built in two different arrangements: pool and loop type. The major difference between the two designs is the placement of the Intermediate Heat Exchanger (IHX). A loop type reactor is similar in principle to a PWR in which the coolant is transferred from the core to the heat exchanger through external pipes. After giving off heat in the heat exchanger, the coolant is pumped back to the core. As opposed to a PWR, there is no boiling on the secondary side of the heat exchanger in a SFR. In contrast to this design, the pool type SFR includes the IHX and primary pumps in the reactor vessel. This provides the advantage that no radioactive sodium leaves the reactor vessel. Additionally, the risk of primary pipe breaks is eliminated as no primary piping exists. This greatly reduces the risk of core uncovering during accident conditions. The greater sodium inventory of the pool type reactor also adds thermal inertia that can help to stabilize temperatures during critical conditions.The disadvantage of a pool type reactor is that the reactor vessel size is increased compared to a loop type reactor because it needs to house the IHX and primary sodium pumps. Since SFRs are usually only slightly pressurized the vessel is much less costly than that of current LWRs and even a larger vessel for a pool type reactor will not be excessively expensive. Maintenance and observation of the IHX and primary pumps are more complicated in pool type reactors because they are covered by radioactive, opaque sodium that reacts with air. This necessitates the removal of sodium before most maintenance operations. Although both types of reactors have been built, there seems to be a slight favor towards pool type reactors [20, 25, 26].

The planned test facility will be based on the AFR-100 (Advanced Fast Reactor) concept developed by ANL. The AFR-100 is intended as a Small Modular Reactor with a rated electric output of 100 MWe and a core lifetime of 30 years. The reactor will be built as much as possible in central factories and then shipped to customers. Even though extensive on-site work will be necessary, shifting the core assembly and other tasks to a centralized location is expected to provide economies of scale that will help the adoption of SMRs. Pre-licensing is further expected to facilitate the adoption of SMRs [11]. The small size, both in terms of geometry and in terms of power output, will make the reactor relatively inexpensive and easily scalable to match demand. This will allow smaller utility companies to more easily afford the reactor and will also provide emerging economies with an option of adding more generation as demand grows. The reduced power output compared to today's nuclear plants makes the AFR-100 more suited for small, less developed grids that might not be able to accommodate 1000 MWe. A smaller overnight cost will provide advantages in the procurement of financing and reduce financing costs. Further, refueling is expected to be provided as a service by the manufacturer. This ensures that no fuel is diverted because the special tools and machinery necessary for refuelings will not be made available to reactor operators. The reactor's small size allows the partial or complete submersion of the core underground, adding protection from the oft cited airplane impact [12, 13].

The AFR-100 pictured in Fig. 2.1 is still in the design stage, allowing results from this thesis and the subsequent experiments to influence the design. The main goals of the AFR are to provide a small reactor (core barrel diameter less than 3.0 m with an active height of less than 1.5 m) with a thermal efficiency of at least 40 % that is refueled in intervals of approximately 30 years. The design should be kept as simple as possible to reduce cost, and to provide easy operation and maintenance even in countries that do not posses a strong nuclear workforce. Actinide transmutation to reduce the long-time radioactivity of the eventual waste products, and hydrogen and desalination capabilities further add to the attractiveness of the design. Cutting edge technology is included in the design, some of which is not yet ready for commercial deployment. The target date for shipping the first AFR-100 is the year 2050. Extensive research has been performed on the core configuration, fuel type, and passive cooling systems as these systems are integral to meeting the design specification listed above [27]. Flow analyses, especially three dimensional, have been somewhat neglected so far, and this work aims to close some of that gap.

The AFR is designed with core inlet and outlet temperatures of 395 °C and 550 °C, respectively. The four primary pumps will be self-cooled electromagnetic pumps that are expected to reduce maintenance requirements. The kidney-shaped, tube and shell IHXs surrounding the core will feature an innovative twisted tube design to increase heat transfer while minimizing the dimensions of the IHX. Three Direct Reactor Auxiliary Cooling Systems (DRACSs) heat exchangers with a capacity of 0.25 percent of nominal power will serve as the decay heat removal system. The metallic uranium-zirconium fuel will be enriched to less than 20 percent U-235. A complex in-vessel fuel handling machine has been developed but will only be on-site during refueling. Otherwise a shield plug will hold its place. Finally, the balance of plant will run on a supercritical CO_2 Brayton Cycle [11, 27].

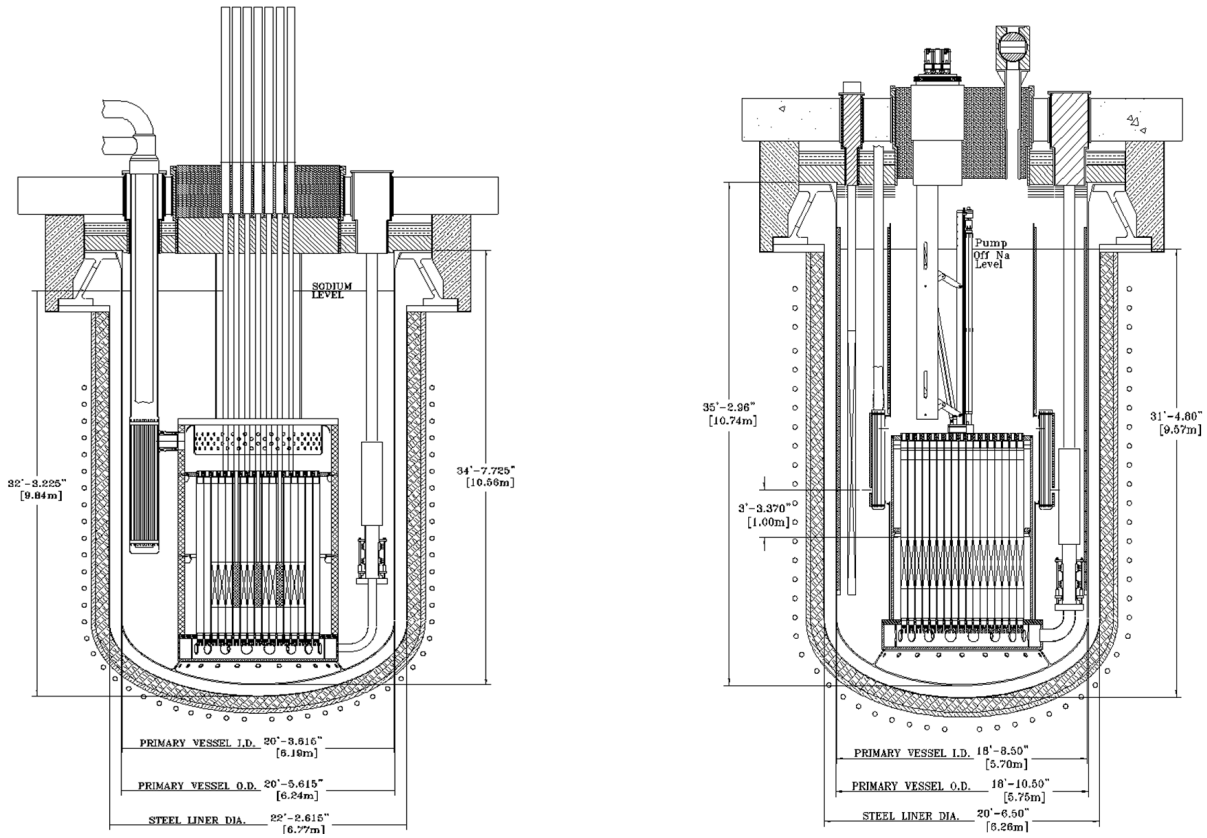

Figure 2.1: Designs 3TT (left) and 4TT (right) for the proposed AFR-100 reactor reproduced with permission from the IAEA [11].

2.2 Thermal Hydraulics

The flow in the upper plenum is complex due it is low Prandtl number and strong buoyancy effects. The Prandtl number is the ratio of viscous to thermal diffusion as defined in Eqn. 2.2 where ν is the kinematic viscosity, α the thermal diffusivity, μ the dynamic viscosity, c_p the specific heat at constant pressure, and k the thermal conductivity. At the expected core outlet temperature of 550 °C the Prandtl number for sodium is 0.004. In comparison, the Prandtl number for water at room temperature is approximately 10. A low Prandtl number ($<< 1$) suggests a much thicker thermal boundary layer than viscous boundary layer. Additionally, heat conduction generally dominates over convective heat transfer. An overview of the most relevant physical properties of sodium is given in Table 2.1.

$$Pr = \frac{\nu}{\alpha} = \frac{\mu c_p}{k} \tag{2.2}$$

Table 2.1: Selected physical properties of Sodium at 550 °C. Property values from University of Fukui [28].

Property	Value	
Density	827.14	kg/m^3
Thermal Conductivity	67.32	W/m-K
Specific Heat	1 257.60	J/kg-K
Dynamic Viscosity	$2.1457 \cdot 10^{-4}$	kg/m-s
Fast Absorption Cross-Section	0.0008	barns †

† One group fast cross-section from [29]

The Reynolds number of the flow is defined as shown in Eqn. 2.3 where ρ is the density, u is the velocity, and D is the diameter. It represents the ratio of inertial to viscous forces. This number changes as a function of temperature and for different conditions in the reactor. During accident conditions with low flow rate, the value will be much lower than at steady-state operating conditions.

$$Re = \frac{\rho u D}{\mu} \tag{2.3}$$

Another useful dimensionless number in the classification of natural convection flows is the Richardson number as defined in Eqn. 2.4 which can be used to quantify the importance of natural convection. In flows with $Ri < 0.1$ natural convection can be neglected, while flows with $Ri > 10$ are dominated by natural convection. For $0.1 < Ri < 10$ both natural and forced convection are important.

$$Ri = \frac{(\rho_1 - \rho_0) g D}{\rho_1 u^2} \tag{2.4}$$

The fluid flow is described by the Navier-Stokes equations that are given below. They consist of five equations in total: the continuity equation (Eqn. 2.5), a momentum equation for each spatial dimension (Eqn. 2.6), and finally the energy equation (Eqn. 2.7). In the equations below, $\vec{\nabla}$ is the divergence operator, $\vec{v}$ is the velocity vector, p is the pressure, $\vec{\vec{\tau}}$ is the stress tensor, $\vec{g}$ is the gravity vector, e_t is the total or stagnation energy, $\dot{q}$ is the volumetric heat generation, and T is the temperature. The stress tensor is defined in Eqn. 2.8 [30].

$$\frac{\partial \rho}{\partial t} + \vec{\nabla} \cdot (\rho \vec{v}) = 0 \tag{2.5}$$

$$\frac{\partial (\rho \vec{v})}{\partial t} + \vec{\nabla} \cdot (\rho \vec{v} \vec{v}) = -\vec{\nabla} p + \vec{\nabla} \cdot \vec{\vec{\tau}} + \rho \vec{g} \tag{2.6}$$

$$\frac{\partial (\rho e_t)}{\partial t} + \vec{\nabla} \cdot (\rho \vec{v} e_t) = \rho \dot{q} + \vec{\nabla} \cdot (k \vec{\nabla} T) - \vec{\nabla} \cdot (p \vec{v}) + \vec{\nabla} \cdot (\vec{\vec{\tau}} \cdot \vec{v}) + \rho \vec{g} \cdot \vec{v} \tag{2.7}$$

$$\vec{\vec{\tau}}_{ii} = 2\mu \frac{\partial v_i}{\partial x_i} - \frac{2}{3}\mu (\vec{\nabla} \cdot \vec{v}), \quad \vec{\vec{\tau}}_{ij} = \mu \left(\frac{\partial v_i}{\partial x_j} + \frac{\partial v_j}{\partial x_i} \right) \quad \text{for} \quad i, j = 1, 2, 3 \tag{2.8}$$

The flow is considered incompressible due to the low flow velocity compared to the speed of sound. The physical properties are assumed to vary with temperature according to the equations given by the University of Fukui in the Coordinated Research Project (CRP) report [28].

Equations 2.5 to 2.7 form a set of coupled, non-linear Partial Differential Equations (PDEs) for which no analytical solution is known. To solve the equations numerically, they are converted to algebraic equations by discretizing them on a mesh or grid. Depending on the formulation of these discretized equations the method can be described through either Finite Difference, Finite Volume, or Finite Element methods. Today, most commercial Computational Fluid Dynamics software packages rely on Finite-Volume formulations. The advantages of finite-volume compared to finite-difference are:

- unstructured meshes can be accommodated,
- mesh elements can be a mix of different types (eg. tetrahedral and hexahedral),
- the method is inherently conservative.

These advantages easily outweigh the difficulties that arise in developing discretizations of greater than second order.

Conceptually, the first step of the finite volume method is to write balance equations for all conserved quantities (mass, momentum, energy, turbulent quantities) for a control volume. These integral balances are then converted to surface integrals using the Gauss theorem, except for the source terms which cannot be converted. The surface and volume integrals are then approximated using quadrature. One point quadrature is common due to its low computational cost and second order accuracy. Each volume element is connected to its neighbors by the fluxes that cross the shared boundary. Writing the balance equations for each volume element leads to a system of coupled, algebraic equations that can be solved using iterative methods [31].

2.3 Turbulence Modeling

Numerous models have been proposed to model turbulence in CFD applications. The most popular models, such as the Standard k-ϵ Turbulence Model (SKE), realizable k - ϵ (RKE), re-normalization group (RNG), and the k-ω shear stress transport (SST) model are based on Reynolds averaging. SST was chosen for the simulations presented in later sections. This selection was based on a recommendation from Choi et al. who suggest using more sophisticated turbulence models that treat the turbulent heat fluxes explicitly. The authors themselves used the SST model in their simulations because the suggested models are not yet available in commercial CFD software packages [32]. The following section provides a quick introduction to the SST turbulence model.

Menter developed the SST in 1992 to alleviate the shortcomings of both the traditional $k-\epsilon$, and $k-\omega$ turbulence models. The $k-\omega$ model performs better in the shear layer close to walls but suffers in free stream fields. The $k-\epsilon$ has the opposite properties which led Meter to develop a model that combines the strengths of the $k-\epsilon$ and $k-\omega$ models. Additionally, Menter added a second blending function for the calculation of the turbulent viscosity.

Using the blending function F_1 and defining mixed constants $\phi = F_1\phi_1 + (1-F_1)\phi_2$ results in the following equations for k and ω as presented by Menter [33, 34]:

$$\frac{\partial(\rho k)}{\partial t} + \frac{\partial(\rho v_j k)}{\partial x_j} = \widetilde{P}_k - \beta^*\rho\omega k + \frac{\partial}{\partial x_j}\left[(\mu + \sigma_k\mu_t)\frac{\partial k}{\partial x_j}\right] \tag{2.9}$$

$$\frac{\partial(\rho\omega)}{\partial t} + \frac{\partial(\rho v_j \omega)}{\partial x_j} = \alpha\frac{1}{\nu_t}\widetilde{P}_k - \beta\rho\omega^2 + 2\rho(1-F_1)\sigma_{\omega 2}\frac{1}{\omega}\frac{\partial k}{\partial x_j}\frac{\partial \omega}{\partial x_j} + \frac{\partial}{\partial x_j}\left[(\mu + \sigma_{\omega 1}\mu_t)\frac{\partial \omega}{\partial x_j}\right] \tag{2.10}$$

In Eqns. 2.9 and 2.10, k is the turbulent kinetic energy, P_k is the production of turbulent kinetic energy due to shear (Eqns. 2.11, 2.12), ω is the dissipation rate of k, α, β, and β^* are closure coefficients, σ_k and σ_ω are empirical diffusion constants, and μ_t and ν_t are the dynamic and kinematic turbulent viscosity, respectively. Eqns. 2.11, 2.12 define the turbulent kinetic energy production and the limiting function thereof [33, 34].

$$P_k = \mu_t \frac{\partial v_i}{\partial x_j}\left(\frac{\partial v_i}{\partial x_j} + \frac{\partial v_j}{v_i}\right) \tag{2.11}$$

$$\widetilde{P_k} = min(P_k; 10 \cdot \beta^* \rho k \omega) \tag{2.12}$$

The boundary layer is divided into two parts to blend the $k-\omega$ and $k-\epsilon$ models. From the wall up to half the boundary layer thickness, F_1 is equal to one which corresponds to a pure $k-\omega$ model. Over the second half of the boundary layer, F_1 decreases to zero so that a pure $k-\epsilon$ model is used in the free stream. The blending function is described in Eqn.2.13.

$$F_1 = \tanh(arg_1^4) \tag{2.13}$$

$$arg_1 = min\left(max\left(\frac{\sqrt{k}}{\beta^* \omega y}; \frac{500\nu}{y^2\omega}\right); \frac{4\rho\sigma_{\omega 2}k}{CD_{k\omega}y^2}\right) \tag{2.14}$$

$$CD_{k\omega} = max\left(2\rho\sigma_{\omega 2}\frac{1}{\omega}\frac{\partial k}{\partial x_i}\frac{\partial \omega}{\partial x_i}; 10^{-10}\right) \tag{2.15}$$

Further, the turbulent eddy viscosity is defined by Eqns. 2.16 and 2.17 where S is the strain rate tensor.

$$\nu_t = \frac{a_1 k}{max(a_1\omega; SF_2)} \tag{2.16}$$

$$S = \sqrt{2S_{ij}S_{ij}} \quad \text{where} \quad S_{ij} = \frac{1}{2}\left(\frac{\partial v_i}{\partial x_j} + \frac{\partial v_j}{\partial x_i}\right) \tag{2.17}$$

$$F_2 = \tanh(arg_2^2) \tag{2.18}$$

$$arg_2 = max\left(2\frac{\sqrt{k}}{\beta^*\omega y}; \frac{500\nu}{y^2\omega}\right) \tag{2.19}$$

The closure constants are defined in Table 2.3.

Table 2.2: Closure constants for Menter's SST turbulence model [34].

	Value	
Constant	Near Wall	Free Stream
α	0.56	0.44
β	0.0750	0.0828
β^*	0.09	0.09
σ_k	0.5	1.0
σ_ω	0.5	0.856

2.4 Monju Reactor Experiments and Simulations

Although fast reactors are rare today, they play an important part in many advanced closed fuel cycles [8]. The fast reactors built to date have been used to conduct research on the special phenomena encountered in fast reactors [28, 35]. The Monju reactor pictured in Fig. 2.2 and completed in Japan in 1995 is an important example of this. The reactor was built as a commercial power reactor with the intention of delivering important information for the design of future fast reactors. Monju generated 280 MW of electricity at a thermal output 714 MW and was permanently shutdown in 2016 due to operational issues [28]

One of the experiments performed on Monju was a simulated turbine failure in 1995. The reactor's automatic emergency shutdown procedure was initiated by sending a "condenser vacuum low" signal to the control system. During the shutdown procedure the control rods were inserted, the main coolant pumps were tripped, and the pony motors for the pumps were started. The resulting flow in the reactor core and upper plenum was a mixture of natural convection and forced convection with a flow rate much lower than during normal operation. The temperature of the coolant entering the upper plenum also decreased due to the reduction in reactor decay heat after the reactor scram [28].

During normal operation, the main flow path for the coolant in the upper plenum is radially outward and upward from the inlet at the center of the plenum. The coolant rises obliquely to the top of the inner barrel and then descends in the annulus between inner and outer barrel. The flow leaves the upper plenum through three outlet pipes that are each connected to one of the cooling loops.

During emergency cooling, the flow loses momentum due to the lower pressure generated by the circulation pumps. The fraction of coolant flowing over the top of the inner barrel and down through the annulus decreases, and more coolant flows through the flow holes at the bottom of the inner barrel. This redirection of the flow leads to a relatively stagnant volume of sodium above the second row of flow holes which reduces mixing and eventually leads to thermal stratification in the upper plenum. The stratification develops because colder, more dense sodium enters the plenum and leaves through the flow holes without disturbing the hotter sodium in the upper parts of the plenum. The stratification interface is characterized by steep temperature gradients which lead to thermal stresses on the plenum structures. The temperatures were measured by 35 thermocouples distributed along the height of the upper plenum. Using these temperature measurements, it is possible to approximate the location of the thermal stratification interface.

2.4.1 Coordinated Research Project

In 2008 the IAEA instituted a CRP to simulate the rising of the thermal stratification interface in Monju using CFD. Eight research institutions from around the globe participated in the project. The task was the same for all research groups: to accurately compute the rising of the thermal stratification inter-

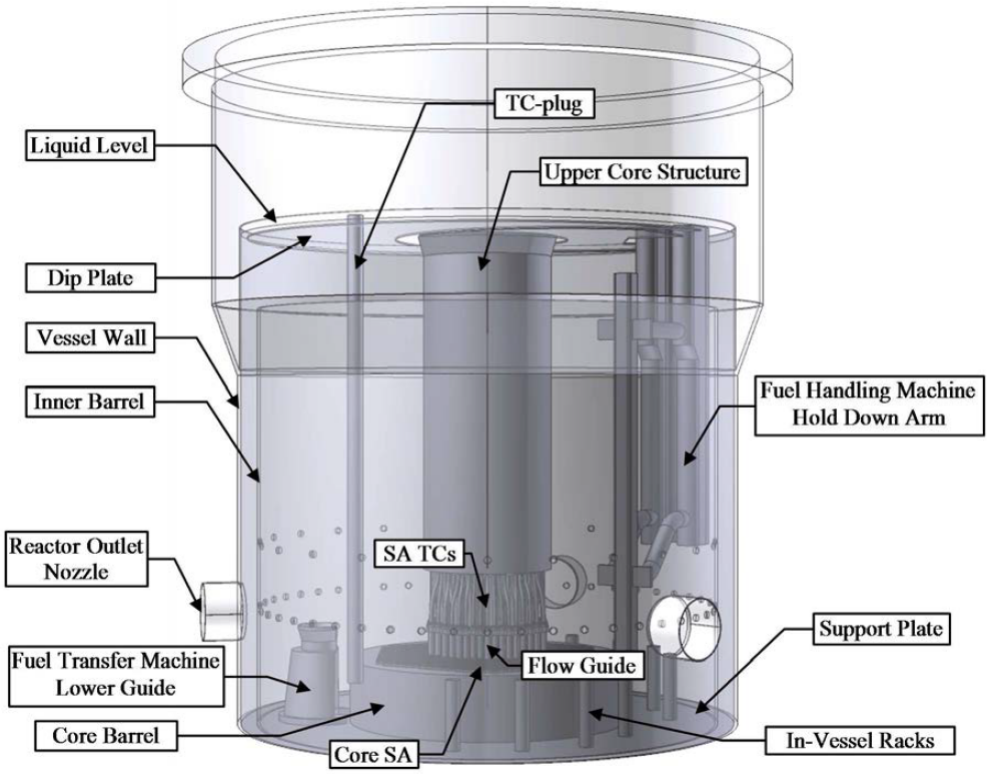

Figure 2.2: Schematic of the Monju reactor upper plenum reproduced with permission from the IAEA [28].

face over the course of the experiment. Fundamental parameters and values such as the dimensions of the reactor were provided by the Japan Atomic Energy Agency (JAEA) at the beginning of the CRP. The individual organisations were free to make their own assumptions or simplifications where necessary, leading to a broad range of different approaches. One example is the simulation domain that was modeled and distributed by Argonne National Laboratory. The model simplifies the geometry to a quarter sector model of the actual upper plenum. The assumption is that structures such as the fuel handling machine can be neglected and that the flow in the upper plenum is axisymmetric. Not all institutions agreed with this simplification and thus developed full sector models for their simulations [28].

The following sections will compare how various details were treated by the participating organizations and what influence these differences had on the quality of the solution. In addition to the results presented in the final CRP report other published results will also be considered.

Geometric Model

Most simulations were conducted using the quarter sector model shown in Fig. 2.3. However, it is clear that the model represents a simplification of the actual geometry. The upper plenum is not axisymmetric as Figure 2.2 clearly shows. To achieve symmetry with the hexagonal core outlet, the outlet pipe has to be rotated by 12.5 degrees. Furthermore, the hexagonal structure of the inlet into the upper plenum cannot be represented exactly by a quarter sector geometry. This leads to the over- and under-representation of some inlet channels [28].

Shibahara et al. conducted simulations using a full sector model. They confirmed that the non-axisymmetry does not significantly influence the rising of the thermal stratification interface in a quarter sector model compared to a full sector model. Their results also show that the flow is close to axisymmetric [36]. This result was confirmed by Yao et al. and Mochizuki et al. [37,38]. Ohira et al. compared

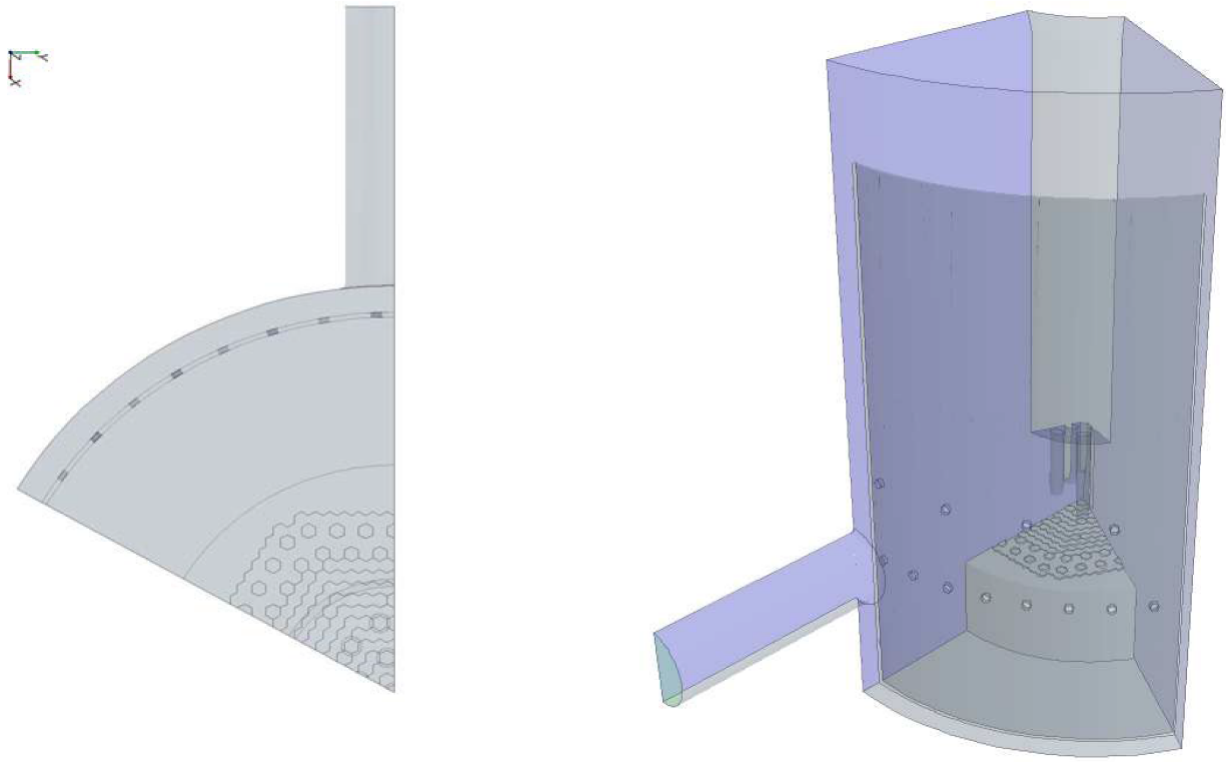

Figure 2.3: Schematic of the quarter sector model of Monju reactor upper plenum reproduced with permission by the IAEA [28].

multiple studies performed on full and quarter sector models and concluded there were no significant differences [39].

The quarter sector model also features a longer outlet pipe than specified by JAEA. This was done to ensure that the numerical outlet condition does not unduly influence the flow in the upper plenum. It is generally believed that this will reflect the actual flow conditions more accurately [28].

The complicated structures at the inlet of the upper plenum collectively referred to as Upper Core Structure (UCS) were simplified in the quarter sector model by treating this region as a porous medium instead of explicitly modeling the geometry [40]. This reduces the complexity of the model and reduces the node count of the mesh. The fine details of the omitted structures would otherwise necessitate very small mesh elements which increases calculation time. The effect of this simplification can be estimated by looking at simulations conducted by Shibahara et al., and Mochizuki and Yao. Shibahara et al. used the porous media approach to reduce the cell count of their full sector model and compared this to a quarter sector simulation with an explicitly modeled UCS. The flow patterns for both cases are similar although the quarter sector model shows a higher maximum velocity at the UCS. The temperature contours show no significant differences in the rising of the thermal stratification interface for both cases [41].

Mochizuki and Yao performed two simulations: one including the fingers for flow and temperature measurements and one without. Although the flow pattern for the two cases differs, the rising of the thermal stratification interface is very similar [37]. It should be noted that Mochizuki and Yao did not approximate the fingers by a porous medium for their comparison but rather omitted them altogether. However, the flow pattern without fingers is very similar to that reported by other researchers using the porous media approach, suggesting that the conclusions derived from the case without fingers are also valid for the porous media model. The porous media model will naturally have a higher pressure drop

than the case without fingers.

Although neither the investigation by Shibahara et al. nor that of Mochizuki and Yao explicitly compares the same geometry with and without the porous media assumption, taken together there is strong evidence that the results are not impacted negatively by the simplification.

Temperature measurements during the experiment were provided by an array of thermocouples inside the so called thermocouple plug. The location of the plug is shown in Fig. 2.2. The 35 thermocouples are located 150 mm to 6050 mm below the liquid level. Although some authors have modeled the thermocouple plug explicitly, most simulations have neglected the plug due to the assumption of symmetry for the quarter sector model. It is difficult to evaluate the effect of modeling the plug or neglecting it, as the various simulations differ in more than the modeling of the plug. Since most of the thermocouples face the flow the influence of the plug on the flow is unlikely to affect the temperature measurements.

Mesh counts differ widely between the simulations conducted under the CRP and in additional studies. Numbers range from approximately 35 000 cells used by the Russian Institute of Physics and Power Engineering (IPPE) to 25 000 000 by the Univeristy of Fukui (UF), Japan. As mentioned before, it is hard to attribute differences in the results to specific assumptions or details. As a general trend, it can be observed that some of the lower mesh count simulations underperform at short simulation times. The IPPE simulation shows significant differences to the experimental results at shorter times but improves for long times especially at 600 seconds and beyond. The results by UF match the experimental data well for short times but show more discrepancies at 600 s. No results are provided by UF past 900 s likely due to the high computational cost of running a long transient simulation on a fine mesh. Most meshes employed during the CRP have mesh counts between 1 and ∼5.5 million [28]. There seems to be no clear relation between mesh size and the quality of the result.

Software

The participants of the CRP were free to use whatever software tools they deemed necessary to solve the posed problem. A wide variety of commercial (STAR-CD, STAR-CCM, Fluent, CFX) and proprietary (GRIF, Trio_U, FrontFlow) software tools were used. Although these tools can affect the simulation results, their individual effects are very hard to determine and lie outside the scope of this work.

Flow Rate Correction/ Energy Imbalance

During their analysis of the CRP the participants from the Univeristy of Fukui noticed an energy imbalance in the boundary conditions provided by JAEA. This energy imbalance leads to a lower temperature at the liquid surface at the top of the plenum [38]. To mitigate this problem, UF used the 1D plant analysis code NETFLOW++ to simulate the reactor during the experiment. Based on these simulation results, the inlet conditions were changed to eliminate the energy imbalance. This correction was only used by UF and might explain their excellent results. It should be noted that the effect of the boundary condition correction on long simulation times cannot be verified as UF did not provide results past 900 s. Further, the study conducted by IPPE yields better predictions than UF at 900 s even without the correction [28]. It stands to reason that the correction should be employed in all future simulations as any energy imbalance at least partially discredits the validity of the results. However, UF did not publish the changed boundary conditions and thus they might not be available to other researchers.

Top Surface

The top surface of Monju is a free surface with a gas-liquid interface of argon and liquid sodium. A dip plate is inserted about 35 mm below the free liquid surface to prevent sloshing of the interface. The interface is modeled as a solid wall in the simplified quarter sector geometry and is treated as adiabatic in all simulations that provide information about the thermal boundary condition [28, 42–44].

Physical Properties

Physical properties of sodium and stainless steel were provided by JAEA as equations. However, IPPE and UF used different sets of equations to describe the variation of physical properties with temperature. The French Alternative Energies and Atomic Energy Commission (CEA) and Korea Atomic Energy Research Institute (KAERI) used constant values for the properties of liquid sodium. The other groups did not provide information on whether or not temperature dependent properties were used [28]. Since measured temperatures range from ∼325 °C to ∼475 °C it seems prudent to allow for temperature dependent properties.

Upper Instrumentation Structure

The Upper Instrumentation Structure is a cylinder located in the middle of the upper plenum. It is made of stainless steel and is filled with the necessary instrumentation for the fingers that measure flow rates and temperatures at the top of the honeycomb structure. The instruments in the Upper Instrumentation Structure (UIS) are surrounded by liquid sodium. In the simplified model, the UIS is treated as an adiabatic wall. However, due to the heat capacity of the stainless steel walls and the sodium inventory the UIS stores a large amount of energy. The Indian Indira Gandhi Centre for Atomic Research (IGCAR), UF, and Mochizuki and Yao included the thermal capacity of the UIS in their simulations to gauge the effect of the additional energy on the rising of the thermal stratification interface [28, 37]. The effect of modeling the thermal capacity is disputed even within the report published by IAEA. UF concluded in their analysis that the thermal capacity could not be neglected. Contrary, IGCAR concluded that the effect of the thermal capacity of the UIS was insignificant with respect to the rising of the stratification interface. In the final conclusions of the report the effect of the thermal capacity is also deemed “not significant” [28].

Flow Holes

The Flow Holes (FH) on the inner barrel are one of the most important factors on the quality of the simulation. During steady state operation the main flow path is upwards from the UCS and over the top of the inner barrel. After the reactor trip, a thermal stratification layer forms that acts as a plug and prevents the flow from rising to the top of the inner barrel. Instead, the flow is diverted to two rows of flow holes on the inner barrel. Numerous studies have confirmed that the fraction of inlet flow going through the FHs increases with time as the transient develops [28, 37, 41, 45]. The first round of simulations for the CRP was conducted with flow holes with straight edges. These edges lead to a high pressure drop and thus decrease the flow through the FHs. This is thought to be the major reason for poor results during the first round of simulations. It was decided to perform a second round of simulations with rounded edge FHs. JAEA was not able to provide detailed information on the actual geometry of the flow holes in Monju. The exact shape and geometry of the FH in Monju remains unknown and until measurements can be performed on Monju, the shape of the FHs will remain a source of uncertainty [28].

Even with the uncertainty pertaining to the exact shape of the flow holes, it is clear from the results that they have a major influence on the rising of the thermal stratification layer. Reducing the pressure drop of the FHs by rounding the edge reduces the resistance of that path and thus increases the flow. This in turn leads to a slower rise of the stratification layer which is important because most simulations overpredict the rising speed of the interface. Fig. 2.4 by Sofu et al. compares the experimental results to simulations with sharp and round edged flow holes. It can be seen that adding rounded flow holes greatly reduces the discrepancies between experiment and simulations for medium to long simulation times. For short times, sharp edged flow holes seem to yield more accurate results. This implies additional sources of error other than the flow holes.

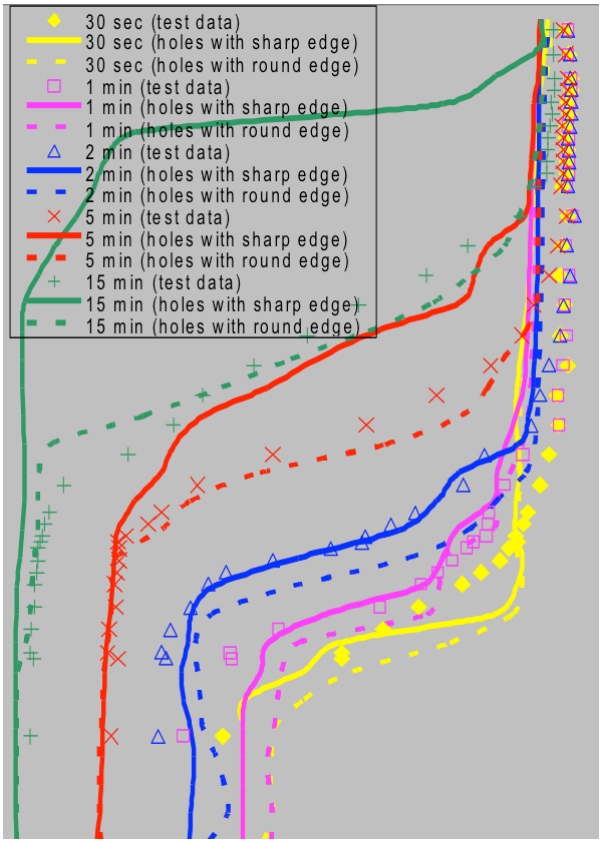

Figure 2.4: Computed and experimental temperature profiles according to Sofu et al. reproduced with permisson from the IAEA [43].

Inner Barrel Conductivity

The inner barrel separates the upper plenum into two parts: an inner annulus around the Upper Instrumentation Structure and an outer annulus between the inner and outer barrels. The inner barrel is made of 40-mm-thick stainless steel. Most simulations, including the simplified quarter sector model, treat the inner barrel as a gap in the model. Meaning that both sides, and the top are modeled as adiabatic walls. This treatment further simplifies the problem but neglects conduction through the inner barrel wall. This assumption was called into question by some researchers and the barrel was modeled explicitly in some simulations. IPPE performed a parameter analysis on the thermal conductivity of the inner barrel and found the duration of the stratified stage to be extremely sensitive to the magnitude of the thermal conductivity of the inner barrel (see Fig. 134 in [28]). It should be noted that the length of the stratified stage decreases with increasing conductivity of the barrel. Simulations up to this point over-predict the rising speed of the interface. Including the conductivity will likely produce results that are further from the experimental values. Nevertheless, it should be included in further calculations because heat transfer through the inner barrel will certainly be present in the actual reactor.

Turbulence Model

Accurate turbulence modeling is still one of the biggest issues faced in CFD applications today. This is especially true in flows that are dominated by natural or mixed convection [32]. The selection of the most appropriate turbulence model for a problem is anything but trivial and often requires some trial and error. Investigations into turbulence models for liquid sodium flows in nuclear reactors have been conducted for a number of years. Muramatsu and Ninokata performed experiments of water and liquid sodium flows in simplified cylindrical containers in 1994 and compared the results to those obtained by simulations using the k-ϵ model with constant and variable turbulent Prandtl number, and the algebraic

stress model. The results indicated that the algebraic stress model predicted the rising speed of the interface most closely. The researchers also suggested using higher order discretization schemes for modeling the convective terms [46]. Ohno et al. performed a similar experiment and simulated the experiment using three different CFD codes (AQUA, STAR-CD, FLUENT) and three different turbulence models (Standard k-ϵ, RNG k-ϵ, Reynolds Stress Model). They found all three models to yield satisfactory results although the RNG model overpredicted the rising of the stratification interface when using Fluent [47]. Shibahara et al. investigated the effect of the Standard k-ϵ Turbulence Model, RNG, and Reynolds Stress Model (RSM) turbulence models in simulations of the Monju experiment. It was concluded that although the models differ at lower times, these differences become almost non-existent at simulation times of 240 seconds and above. This is attributed to the fact that the flow is dominated by natural rather than forced convection at longer times [41].

The participants of the CRP concluded that there was no significant difference in the performance of turbulence models based on the high Reynolds number standard k-ϵ model in predicting the rising of the thermal stratification interface [28].

Choi et al. investigated the suitability of different turbulence models for the simulation of natural convection flows. They contend that most turbulence models were derived for forced convection and do not perform well in natural convection simulations. They suggest using turbulence models that explicitly treat the turbulent heat fluxes, for example the generalized gradient diffusion hypothesis, the algebraic flux model, or the differential flux model. The authors recommend using an elliptic blending or elliptic relaxation model for simulating the thermal stratification in Monju but acknowledge the difficulties in implementation as these models are not available in most commercial software. Choi et al. used the SST model in their simulations because they deemed it the most capable turbulence model available in their software (CFX) [32, 48, 49].

Although Choi et al. put a strong emphasis on the turbulence model, their results are not as good as other simulations using different turbulence models, especially the IPPE simulation in the CRP report. These differences are likely due to the fact that Choi et al. did not use rounded flow holes. To this author's knowledge, no simulation has been performed with rounded flow holes using the SST model.

Ideally, further simulations will include more advanced turbulence models as suggested by Choi et al. when these models become available in commercial codes.

Final Evaluation of Results

In summary, much research has been conducted on the thermal stratification behavior in the Monju reactor. The participants of the Coordinated Research Project and the associated conference papers present a host of valuable information some of which is summarized in Tables 2.3 and 2.4. The most important influence on the quality of the solution seems to be the geometry of the flow holes on the inner barrel. A rounded edge produces much less pressure drop and improves the simulation result compared to the experiment. Even though the exact geometry is unknown, it is safe to assume that the actual geometry features some kind of rounded edge. Nevertheless, the prediction of the interface is difficult for long simulation times. The best results to date have been produced by the Russian Institute of Physics and Power Engineering. IPPE's simulation is fairly accurate even at simulation times up to 30 minutes. This is somewhat surprising considering the low mesh count (~35 000) and the simple algebraic turbulence model that was used. The low mesh count enabled simulation up to 120 minutes but the differences between simulation and experiment become more pronounced at longer simulation times. IPPE's simulation also struggles at shorter simulation times. The results presented by the University of Fukui seem to be the best up to 10 minutes of simulation time. This is likely due to the correction of the inlet conditions that UF performed, as well as the inclusion of many details such as rounded flow holes,

thermal capacity of the Upper Instrumentation Structure, inner barrel conductivity, and temperature dependent properties. Further research is necessary to achieve a simulation that can accurately predict the rising of the stratification interface on all time scales.

Table 2.3: Overview of simulations for the IAEA Monju benchmark (Part 1).

Source	Rounded Flow Holes	Thermal Capacity UIS	Inner Barrel Conductivity	Flow Rate Correction	Heat Transfer on Outer Surfaces	Temperature-dependent properties	UCS modeled	Thermo-couple plug	Upper boundary
CRP Report [28]:									
CIAE	x								
CEA									
IGCAR	x	x	x						adiabatic
JAEA	x		x						adiabatic
Univ Fukui	x	x	x	x		x		x	
KAERI									
IPPE	fixed loss coefficient		x			x			
ANL	x								
Bieder [42]	x								symmetry
Mochizuki [37]		x	x		x		x		
Ohira [44]	x		x					x	adiabatic
Sakamoto [45]						x	x	x	
Shibahara [36]						x	x	x	
Shibahara [41]						x		x	
Shibahara [50]						x		x	
Sofu [40]									
Sofu [43]	x								rigid wall, adiabatic, constant temp

Table 2.4: Overview of simulations for the IAEA Monju benchmark (Part 2).

	Software	Turbulence Models	Mesh	Mesh count	Sector
CRP Report [28]:					
CIAE	STAR-CCM+	SKE			Full
CEA	Trio_U	high reynolds k-e	tetrahedral	335 000	1/6
IGCAR	STAR-CD	SKE	hexahedral	760 000	1/6
JAEA	FrontFlow/Red	RNG k-e	mixed	18 000 000	Full
Univ Fukui	FLUENT		tetrahedral	25 000 000	Full
KAERI	CFX-13	k-w SST	tetrahedral	1 300 000	1/6
IPPE	GRIF	algebraic	non-uniform	34 056	1/6
ANL	STAR-CD	RKE	polyhedral	840 000	1/6
Bieder [42]	TRIO_U	SKE	tetrahedral	1 250 000	
Mochizuki [37]	Fluent 13	RKE	polyhedral-hexahedral mixed	5 970 000	
Ohira [44]	FrontFlow/Red	RNG k-e	mixed	18 000 000	
Sakamoto [45]	FLUENT 12.0	SKE		510 000	
Shibahara [36]	FLUENT 12.1	SKE		11 400 000	1/3
Shibahara [41]	FLUENT 12.0	SKE, RNG, RSM		510 000	
Shibahara [50]	FLUENT 12.1	SKE		5 110 000	
Sofu [40]	STAR-CD	RKE	polyhedral	840 000	
Sofu [43]	STAR-CD, STAR-CCM+	RKE	polyhedral	840 000	

3 Test Facility

The Multiphase Flow and Thermal-hydraulics Lab at Virginia Tech proposed building a test facility for upper plenum thermal hydraulics in the spring of 2016 in collaboration with Argonne National Laboratory. The stated goal of the facility was "to conduct experimental studies on pool mixing and thermal stratification and its influence on natural circulation in a scaled liquid metal facility" [51]. To this end, experimental results would be compared with results from CFD simulations. The experimental facility would thus result in a better understanding of the flow pattern in the upper plenum, and also help to validate and possibly improve the simulation capabilities for mixed convection.

The planned facility uses gallium as a working fluid to avoid the experimental risks associated with sodium. At the same time, the low Prandtl number of gallium would establish the necessary similarity with sodium to make the results applicable for planned sodium reactors. Gallium's lower melting point and higher boiling point compared to sodium will also help to facilitate experiments. However, gallium reacts with both cooper and aluminum which will be taken into account when constructing the facility. Gallium is also more expensive than sodium, and the material cost will be a significant portion of the expenditure for the facility. Data collection through advanced measurement techniques will yield high fidelity, three dimensional data on both steady-steady operation and transients as encountered during loss of flow accidents. The instrumentation can be see in Figure 3.1b.

3.1 Geometry of the Test Facility

The proposed facility is shown in Figure 3.1a. The main components are the plenum, the heat exchanger, the pump, and the heater. These components will be used to simulate the flow during normal operation. To investigate natural convection flows, a bypass is added that circumvents the pump and introduces a fixed pressure drop via an orifice plate. Depending on the experiment, an upper internal structure can be added as shown in the figure. The main test section is housed in a temperature controlled enclosure to limit or simulate heat-losses. Flow meters, thermocouples and pressure transducers are placed at the plenum inlet, and heat exchanger inlet and outlet as shown in Figure 3.1a. This setup will help to accurately determine the boundary conditions that are used for future CFD simulations. The facility will be two meters tall, 0.75 meters wide, and 2.5 centimeters thick. A comparison between the AFR-100 design and the test facility is provided in Table 3.1. Figure 3.1b shows a cross-section of the facility. Pictured are an infrared camera with associated high emissivity coating on the surface facing the enclosure. The camera will provide two dimensional images of the wall surface temperature that can be extrapolated to yield temperatures at other locations in the enclosure. Additionally, three dimensional temperature measurements are provided by an optical fiber. The fiber is capable to providing measurements of ±0.4 °C with a spatial accuracy of 1.25 mm. Still further measurements are provided by thermocouples.

3.2 Scaling of the Test Facility

To make the results obtained from the test facility applicable to full size reactors, scaling has to be conducted in a way that preserves the important effects. Geometrically, the aspect ratio of the enclosure is maintained. Physically, the main effects under investigation are thermal stratification and mixing. For a buoyant jet as encountered in this problem, two time scales of interest can be identified. The thermal penetration time t_{th} is the time it takes for heat to conduct through a stagnant upper plenum. This time is closely related to the thermal penetration depth. The entrainment time t_{se} is the theoretical time it would take to entrain the whole upper plenum. If $t_{se} >> t_{th}$ thermal stratification is present for times less than t_{th}. If on the other hand $t_{th} >> t_{se}$, the pool is well mixed [51]. Table 3.1 shows that the entrainment time and time ratio of the reactor are matched by the test facility. The thermal penetration time is not matched exactly but is on the same order of magnitude. In any case, the relative magnitude of

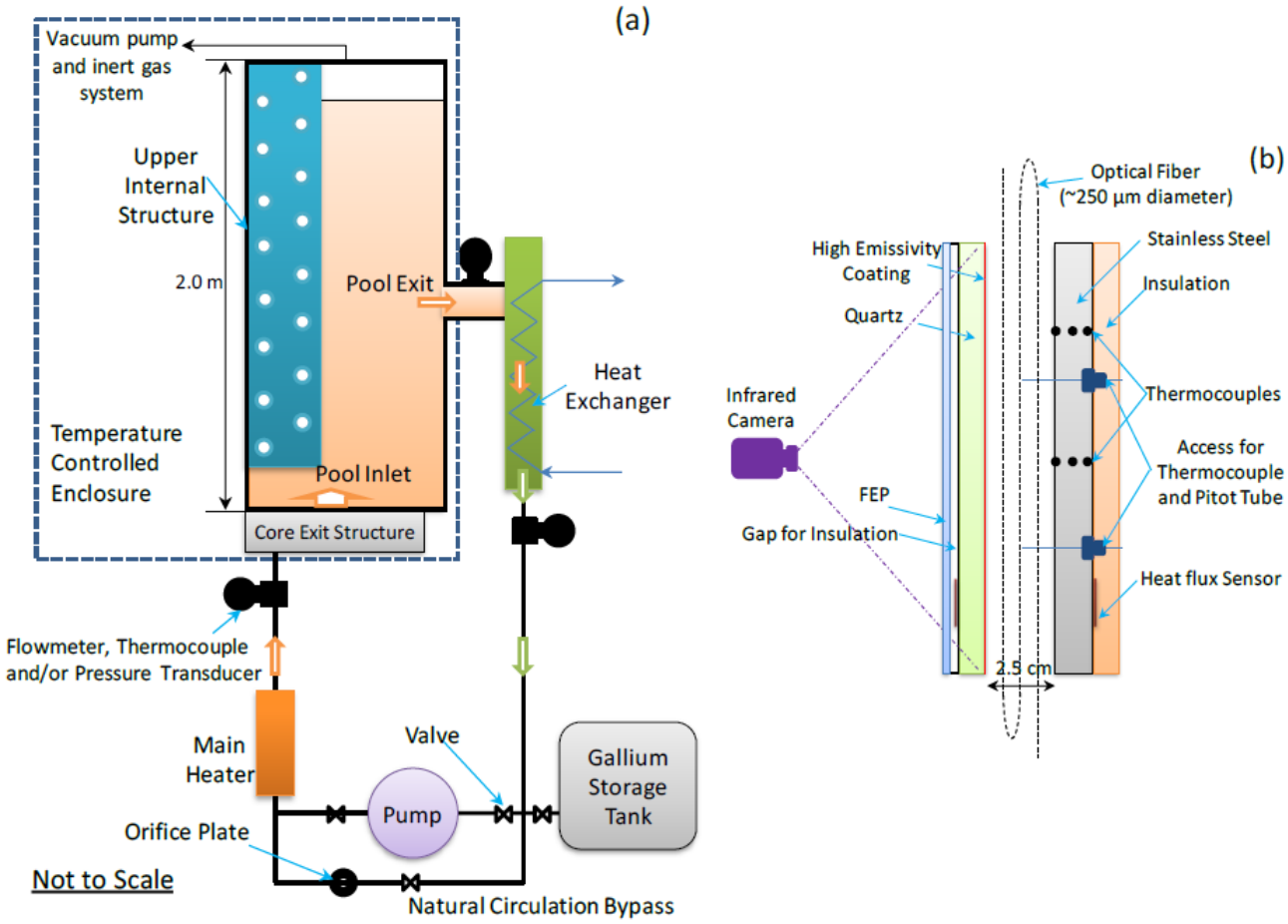

Figure 3.1: (a) Preliminary design of the proposed test facility, (b) schematic of the instrumentation layout. Figure used with permission from author [51].

both effects is preserved because the time ratio is preserved [51]. Scaling of the inlet velocity is provided in Section 4.1.

Table 3.1: Comparison of relevant upper plenum parameters of AFR-100 and proposed test facility [51].

	AFR-100 (normal operation)		Test Facility	
Upper plenum dimension	H: 4.3	m	H: 2.0	m
	R: 1.62	m	W: 0.75	m
			Thickness: 2.5	cm
Height/radius (or width) ratio	2.65		2.65	
Maximum temperature difference ΔT	150	°C	230	°C
Richardson number Ri	39		1 - 1000	
Entrainment time t_{se}	61	s	22 - 224	s
Thermal penetration time t_{th}	9.27×10^4	s	8.48×10^4	s
Time ratio t_{se}/t_{th}	1.52×10^3		$0.39 - 3.85 \times 10^3$	

4 Simulation

The following sections present the setup of the CFD simulation along with a description of the investigated conditions and cases, and their results.

4.1 Setup

The goal of the CFD study is to provide qualitative information for the design of the test facility, identify interesting experimental conditions, provide results for validation and verification, and compare different design alternatives for the AFR-100. To achieve these goals, the simulation has to represent reality accurately. Part of this representation is achieved by appropriate scaling of the facility and simulation domain as mentioned in Section 3.2. Further details on scaling will be provided below. However, it should be mentioned that even the best scaling laws need accurate information about the prototype facility they are referencing. In the case of the AFR-100, details of the upper plenum geometry such as inlet nozzle size and quantity, inlet velocity, outlet position and geometry are scarce. Where no information was available literature searches were conducted to identify typical values used in other designs.

The simulation domain is the pool of the test facility described above with a height of 2 m, a width of 0.75 m, and a depth of 2.5 cm. Fluid enters the domain at the bottom and leaves through an outlet in the right wall. The outlet starts at an elevation of 0.92 m measured from the inlet, and is 18.6 cm in height. The dimensions of the outlet were determined by averaging measurements of the drawings provided by Grady et al. in [11] for both the 3TT and 4TT design, and then scaling by the geometric scaling factor of the facility (0.465). The position of the outlet differs between designs 3TT and 4TT, and averaging of the result was not deemed prudent as neither design would be accurately represented. Tanaka et al. performed experiments on the thermal stratification in liquid metal upper plenum geometries and determined that a low inlet, as present in the AFR-100 design, is best matched with a high outlet [52]. The "high" outlet in the experiment translates into a plenum diameter to outlet height ratio of 1.63. The same ratio was used to determine the position of the outlet in the simulation model, yielding the aforementioned elevation of 0.92 m. Table 4.1 shows the wide spread of outlet positions of reference designs. The position of the outlet chosen for the simulation falls squarely within this range.

The inlet geometry is also not sufficiently described in the currently available design information on the AFR-100. The drawings for both designs indicate one large opening that spans almost the entire diameter of the upper plenum. This design is highly unusual and considered unfinished. It is expected that further features such as nozzles and instrumentation pipes will be added in future design iterations. The size and layout of these features can only be speculated at this point. To take these uncertainties into account, three cases of inlet designs will be simulated. The first assumes that the single, large inlet shown in current design drawings is in fact the final design. The size of the inlet is scaled to preserve the same D_{inlet}/D_{plenum} as in the drawings, leading to an inlet diameter of 0.64 m. The two remaining configurations feature inlet nozzles instead of a single big opening. Although Monju is a loop type reactor of greater capacity than the AFR-100 (280 MWe compared to 100 MWe) the nozzle size given in the CRP was used because it is the only available information on nozzle sizes in fast reactors [28]. Scaling using the geometric scaling factor yields a nozzle size of 3.16 cm. Case 2 has 4.5 nozzles, and Case 3 has 1.5 nozzles. The number of nozzles is not an integer because one nozzle is cut in half by the symmetry plane.

Inlet Velocity

As mentioned before, care has to be taken when scaling the domain and boundary conditions. Peterson found that two bouyant jets are similar if their Richardson numbers are equal [61]. Equation 4.1 defines the Richardson number where g is the gravitational acceleration, β is the volumetric expansion coefficient, ΔT is the temperature difference, H is the height of the plenum, and u is the inlet velocity. It should be noted that the Ri is defined here using the height whereas Peterson used the jet diameter.

Table 4.1: Comparison of outlet position in different SFR designs.

Reference	Reactor	Type of Reactor	IHX Outlet Position	D_{plenum}/h_{outlet}
Hahn et al. [53]	KALIMER-600	Pool	Top	0.79
Chang et al. [54]	ABTR	Pool	Middle	1.3
Kim et al. [55]	No information	Pool	Middle but barrel with high lip	1.07
Grandy et al. [11]	AFR Design 3TT	Pool	Top	6.32
	AFR Design 4TT	Pool	Bottom	∞
Chang et al. [56]	SMFR	Pool	High-Middle	0.52
Yoshikawa, Minami [57]	MONJU	Loop	Top but low flow holes	1.33
Srinivasan et al. [58]	No information	Loop	Middle	3.83
Chellapandi et al. [59]	PFBR	Pool	Middle	3.7
Walter et al. [60]	SNR-300	Loop	Top with barrel	1.95
	Super Pehnix	Pool	Bottom	21.5
	JSFR	Loop	Middle (vertical pipe)	0.81

Assuming that $g, \beta, \Delta T$ are the same in prototype and experiment the scaling criterion reduces to Eqns. 4.2 & 4.3.

$$Ri = \frac{g\beta\Delta T H}{u^2} \tag{4.1}$$

$$1 = \frac{Ri_{sim}}{Ri_{actual}} = \frac{u^2_{actual} \cdot H_{sim}}{u^2_{sim} \cdot H_{actual}} \tag{4.2}$$

$$u_{sim} = \sqrt{\frac{H_{sim}}{H_{actual}}} \cdot u_{actual} = \sqrt{\frac{2\ m}{4.3\ m}} \cdot u_{actual} = 0.682 \cdot u_{actual} \tag{4.3}$$

The actual inlet velocity is not specified in the available reports on the AFR-100 design but can be calculated using the provided flow rate and an estimated inlet area as shown in Eqn. 4.4 where Q_{in} is the inlet flow rate, and A_{in} is the inlet area. The inlet area is calculated using a measured inlet diameter from the design documents assuming one large inlet. Using the inlet flow rate provided by Grandy et al. the inlet velocity is calculated in Eqn. 4.5 [27]. Applying the scaling factor derived in Eqn. 4.3 yields the inlet velocity for Configuration 1 (Eqn. 4.6).

$$u_{in} = \frac{Q_{in}}{A_{in}} \tag{4.4}$$

$$u_{in,\ actual} = \frac{1.532\ m^3/s}{5.983\ m^2} = 0.256\ m/s \tag{4.5}$$

$$u_{in,\ sim} = 0.682 \cdot u_{in,\ actual} = 0.682 \cdot 0.256\ m/s = 0.175\ m/s \tag{4.6}$$

For Configurations 2 and 3, no Richardson number can be calculated for the prototype because the design drawings do not show any nozzles. It was decided, that the characteristic frequency of the domain should be conserved between the different configurations. Since the volume of the geometry is

unchanged, this criterion reduces to a constant flow rate between configurations. The calculations for Configuration 2 and 3 are shown in Eqns. 4.7 & 4.8, respectively.

$$u_{in,\,2} = \frac{A_{in,\,1}}{A_{in,\,2}} \cdot u_{in,\,1} = \frac{0.016\ m^2}{0.0036\ m^2} \cdot 0.175\ m/s = 0.778\ m/s \tag{4.7}$$

$$u_{in,\,3} = \frac{A_{in,\,1}}{A_{in,\,3}} \cdot u_{in,\,1} = \frac{0.016\ m^2}{0.0012\ m^2} \cdot 0.175\ m/s = 2.33\ m/s \tag{4.8}$$

Cover Gas

During preliminary simulations it was found that it is not necessary to simulate the cover gas above the upper plenum. The comparison of two simulations with and without cover gas showed no significant differences. Additionally, the simulations run much faster without the added equations for species transport as required by adding a cover gas. Furthermore, the ANSYS Fluent code experiences convergence issues when solving the gas transport equations on multiple processors. Single processor calculations can be completed successfully but take much longer than a multi-core calculation. For all these reasons, the cover gas was neglected from the simulations, and the top boundary was modeled as an adiabatic wall. The adiabatic condition is justified based on the large shield plug covering the reactor. The simulated domain can be interpreted as a pool covered by a dip-plate as in the Monju reactor. It should be noted that sloshing and gas entrainment cannot be predicted with this setup. However, these phenomena are not the focus of this work.

Thermal Boundary Conditions

The thermal boundary conditions are expected to have a large influence on the thermal stratification behavior of the upper plenum. Heat losses above the stratification interface will enhance mixing by cooling the hotter sodium at the top of the enclosure. Heat losses below the outlet will have the opposite effect and increase stratification by further cooling the cold fluid at the bottom of the pool. As mentioned in the previous section, the top surface was modeled as an adiabatic wall due to the large amount of insulating material above the upper plenum. An adiabatic boundary condition was also selected by all participants of the CRP that provided information about the top boundary [28]. Near axisymmetry of the upper plenum was confirmed by multiple participants of the CRP and thus the front, back, and center walls were modeled as adiabatic. The spaces between the inlet nozzles were modeled as adiabatic because the combined effect of the thickness of the top plate and the temperature difference across the plate are not expected to lead to significant heat transfer. The space between the inlet and the outer edge of the upper plenum was modeled as adiabatic because insufficient information was available about this boundary. Depending on the design, the surface is either connected to the cold pool or the core. The two configurations are expected to yield very different results. A cold surface would increase stratification while a hot surface would reduce it. The right wall that represents the interface between upper plenum and Intermediate Heat Exchanger has two different temperatures. The sections above and below the outlet have temperatures of 660 K and 640 K, respectively. These values were selected based on simulation results presented by Chang et al. in the Preconceptual Design Report for the Advanced Burner Test Reactor, a predecessor to the AFR [54].

Velocity Boundary Conditions

To simulate the flow correctly, appropriate velocity boundary conditions are very important. All walls except for the left side were defined as no-slip walls, resulting in a local fluid velocity of zero. Modeling a full reactor instead of the test stand requires changing the front and back walls to symmetry boundaries. The effect of this change will be investigated in later sections. The left side wall was modeled using a symmetry boundary condition that enforces a gradient of zero in the directions parallel to the wall. The wall normal velocity is zero as a flow through the wall would violate the symmetry condition. Three

Table 4.2: Solvers used for the simulations.

Equation	Solver
Pressure-Velocity Coupling	SIMPLEC
Gradient	Least Square Cell Based
Pressure	PRESTO!
Momentum	First Order Upwind
Turbulent Kinetic Energy	First Order Upwind
Specific Dissipation Rate	First Order Upwind
Energy	First Order Upwind
Time	First Order Implicit

different inlet velocities were used as explained in Section 4.1. For the cases with one big inlet, 4.5 nozzles, and 1.5 nozzles the inlet velocities were 0.175 m/s, 0.778 m/s, and 2.33 m/s, respectively. The outlet was defined as a pressure outlet at a gauge pressure of zero. The actual pressure at the outlet is not known but is certain to be higher than zero because a positive pressure head is required to drive the flow through the heat exchanger. By solving the pressure field relative to a zero potential, the obtained results can simply be added to the actual outlet pressure. Further, the flow is not influenced by the absolute magnitude of the pressure but rather by pressure differences. A pressure outlet condition, as opposed to an outflow outlet condition, is recommended by the code manufacturer ANSYS for calculations involving unsteady flows of varying density, as well as cases with possible backflow, both of which are present in this simulation [62].

Turbulence Modeling

As mentioned in Sections 2.3 and 2.4.1, Menter's SST model was chosen for modeling turbulence. The turbulent intensity at the inlet was set to 5 % and the hydraulic diameter was set to 0.048 m for Case 1 (one big opening), and to 0.0279 m for Cases 2 and 3. The backflow turbulent intensity at the outlet was set to 5 % with a hydraulic diameter of 0.044 m.

Solver Settings

The SIMPLEC algorithm was chosen for pressure-velocity coupling because it can improve convergence compared to to SIMPLE. Even when it does not provide any benefit, it yields similar conversion to SIMPLE. Further, SIMPLEC can reduce computational time compared to PISO for small time steps [62]. Pressure interpolation was done using the PRESTO! scheme. During preliminary simulations, oscillations were discovered for the inlet jets as shown in Figure 4.1. These oscillations were deemed numerical in nature and thus the spatial discretization of the momentum, turbulent kinetic energy, turbulent dissipation rate, and energy equations was changed to a first order scheme. The oscillations disappeared when using a first order upwind scheme. Although first order discretization yields less accurate results, it reduces computation time in addition to eliminating the oscillations. Typically, second order discretization adds an artificial dissipation that reduces oscillations. The results obtained from preliminary simulations seem to contradict this. A complete overview of the used solvers is given in Tab. 4.2.

4.2 Mesh Sensitivity

In CFD simulations, the mesh has a large influence on the quality of the solution. Coarse meshes may not provide a detailed enough solution, and more importantly, might not resolve important details such as recirculation zones. Fine meshes provide more detail but have a higher computational cost. Especially when using explicit time stepping, fine meshes require small time steps to remain stable thus increasing the computational cost even further. When all important features and effects are resolved,

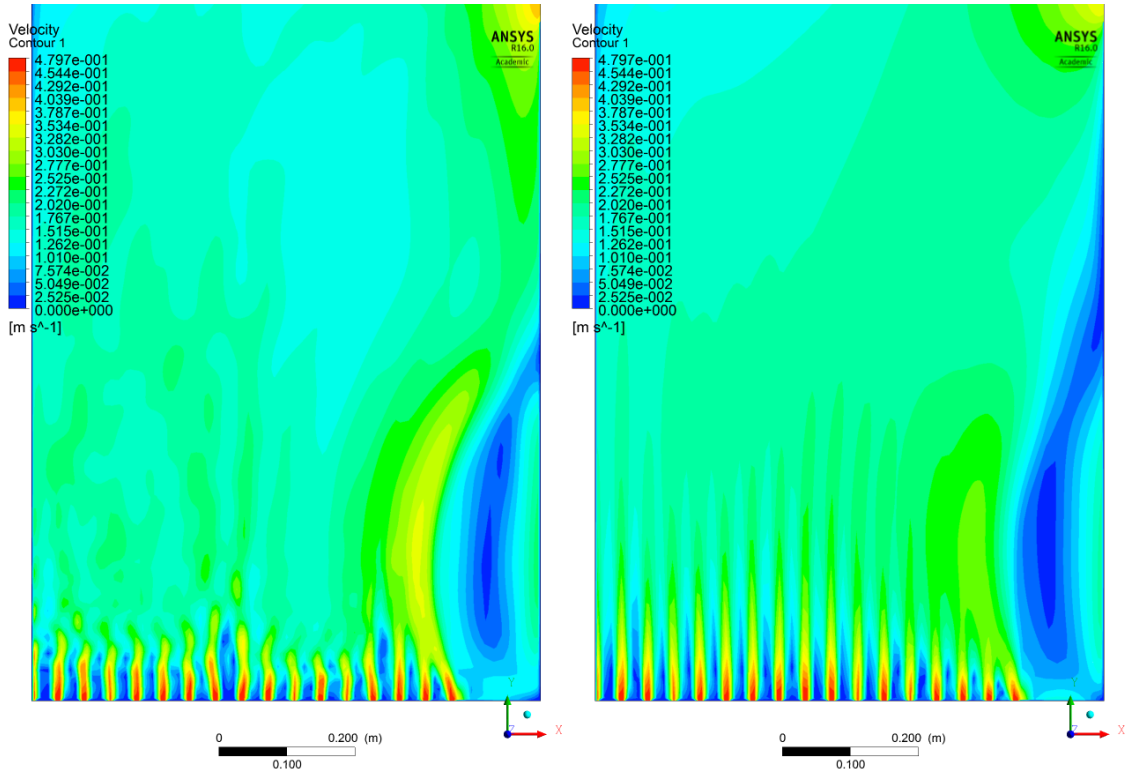

Figure 4.1: Velocity contours for simulations conducted using second order discretization (left), and first order discretization (right).

refining the mesh will not improve the quality of the solution. A mesh should therefore be fine enough to resolve the important features while maintaining an acceptable computational cost. To this end, a mesh sensitivity analysis was performed on Case 3. Case 3 was deemed the most demanding case because it has the highest inlet velocity and was thus chosen for the mesh analysis. The different meshes are described in Table 4.3. All meshes use quadrilaterals and default parameters unless otherwise noted. The mesh was refined in z-direction to better resolve the boundary layer that will form perpendicular to the walls. The refinement is biased toward the front and back walls with a bias factor of 5.

The simulation was run using Fluent's transient solver with settings and boundary conditions as described above. The heat loss boundary condition was deactivated for this simulation to reduce computational requirements. This setup results in a steady-state problem. The transient solver was used nonetheless because it will be necessary in later simulations.

During the mesh sensitivity analysis, two distinct solutions were encountered. Both solutions are pictured in Figure 4.2. The flow pattern on the left side shows a large upward jet as both inlet jets merge on the symmetry wall. The flow bends at the top of the enclosure and finally descends along the right edge. There is a large undisturbed region in the middle of the domain. The left inlet jet in the right image shows a similar flow pattern to that of the left image. However, in this flow pattern the second inlet jet is oriented towards the outlet, causing the first jet to bend around it. Streamlines and vectors reveal that the flow of the left jet eventually merges with the right jet at the bottom of the enclosure. From there the liquid moves obliquely upward toward the outlet. The undisturbed area in the middle is smaller in this second flow pattern and is shifted upward. A similar bifurcation of the solution was found by Bieder and Fauchet, and was also mentioned in the CRP report by the French Alternative Energies and Atomic Energy Commission (CEA) and the Korea Atomic Energy Research Institute (KAERI) [28, 42]. The two

Table 4.3: Parameters of the meshes investigated in the mesh sensitivity analysis.

Mesh	Maximum Face Size in mm	Element Size in Z-Direction in mm	Total Number of Elements	Solution
1	50	1	152 755	Buoyancy
2	30	1	210 800	Momentum
3	10	1	598 900	Momentum
4	10	0.8	816 960	Momentum
5	10	0.6	1 172 180	Buoyancy
6	8	0.6	1 557 864	Buoyancy
7	7	0.6	1 891 890	Buoyancy
8	6	0.6	2 397 402	Momentum

solutions were termed the buoyancy solution (left in 4.2) and momentum solution (right in 4.2). In general agreement with CEA, it was found that:

- the momentum solution is obtained with first order schemes on coarse meshes, and the finest mesh,
- the buoyancy solution is obtained on fine meshes, except for the very finest,
- the buoyancy solution is also obtained with second order schemes on coarse meshes,
- the buoyancy solution converges better,
- the solution cannot be altered by changing the discretization scheme after an initial solution is found.

The participants of the Coordinated Research Project noted that the momentum driven solution is likely the correct flow pattern for the Monju reactor at 40 % rated power. However, whether this translates to the AFR geometry will have to be verified experimentally.

Due to the bifurcated nature of the solution, not all meshes can be compared to each other. Meshes that yield the same solution were compared based on three quantities: mass average outlet velocity, and maximum and minimum outlet velocity. The results are summarized in Table 4.4 and visualized in Figures 4.3 and 4.4. Mesh 6 was chosen as the mesh for further simulations because the differences to Mesh 7 in all three categories are less than one percent.

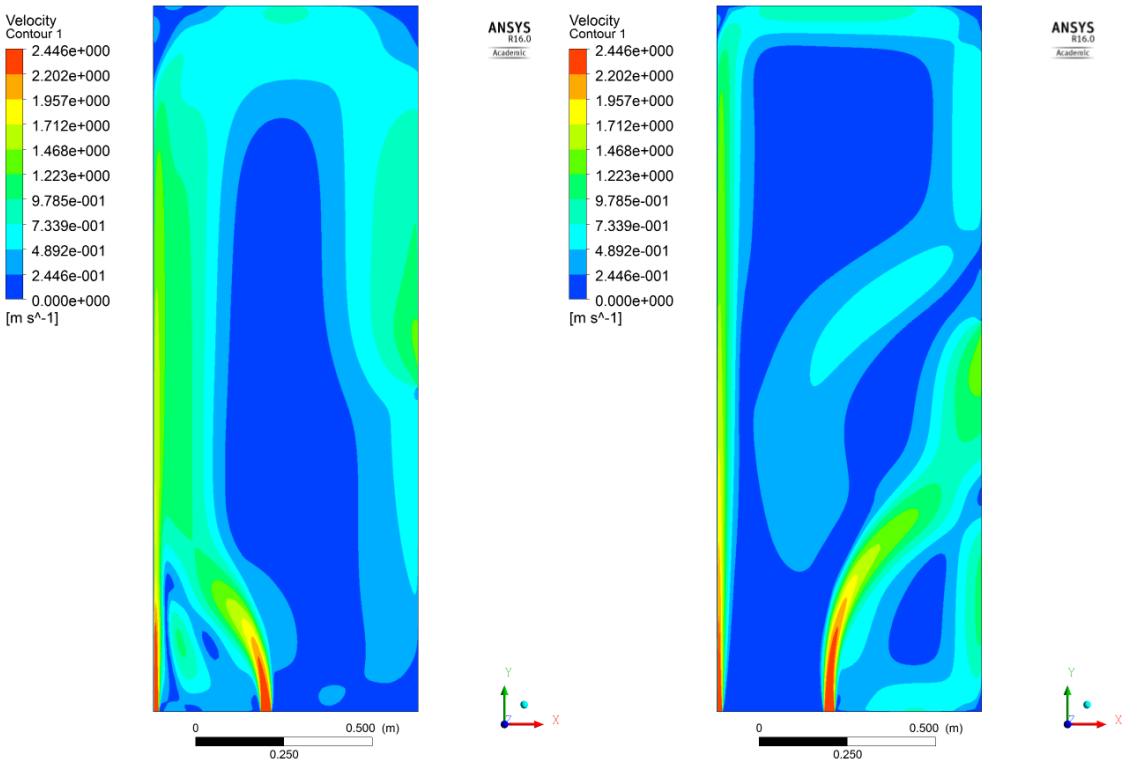

Figure 4.2: Velocity contours for the buoyancy solution (left) and the momentum solution (right).

Table 4.4: Results of mass average outlet velocity, and maximum and minimum outlet velocity for different meshes.

Mesh	Average Outlet Velocity in m/s	Percent change	Max. Outlet Velocity in m/s	Percent change	Min. Outlet Velocity in m/s	Percent change
Buoyancy:						
1	1.10394		1.24595		0.717078	
5	1.17815	6.72	1.3206	5.99	0.674881	-5.88
6	1.18294	0.41	1.31931	-0.10	0.674036	-0.13
7	1.18924	0.53	1.32394	0.35	0.674478	0.07
Momentum:						
2	1.18392		1.32512		0.778929	
3	1.25419	5.94	1.39834	5.53	0.837517	7.52
4	1.26187	0.61	1.40708	0.63	0.79384	-5.22
8	1.29501	2.63	1.46426	4.06	0.777273	-2.09

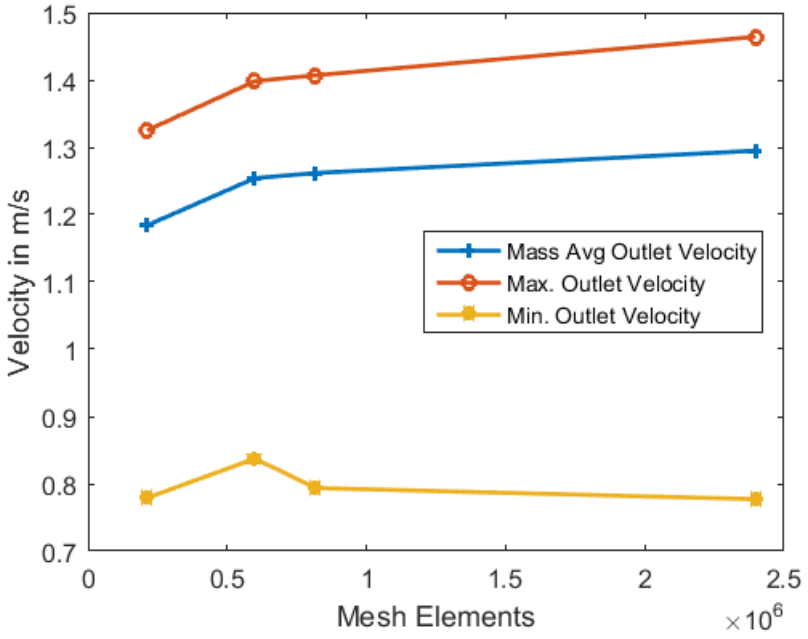

Figure 4.3: Comparison of the four meshes that resulted in the momentum solution.

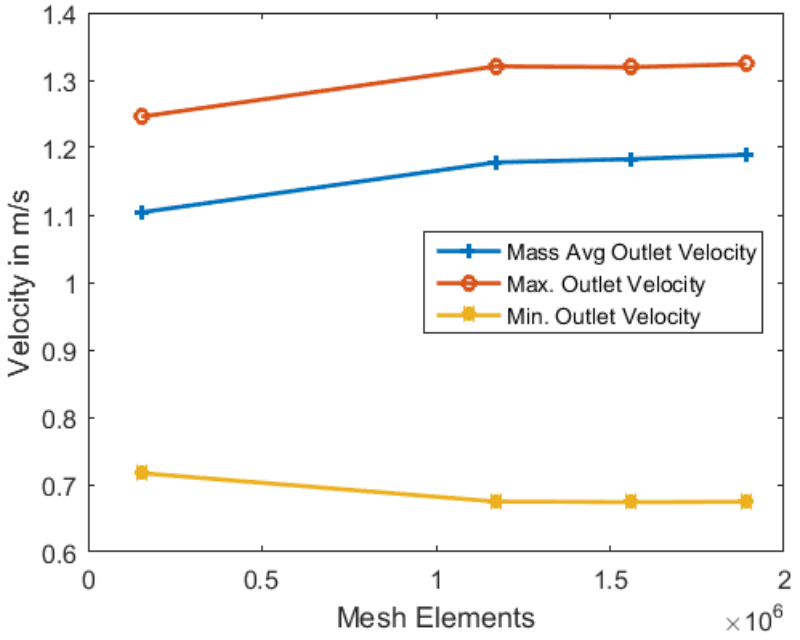

Figure 4.4: Comparison of the four meshes that resulted in the buoyancy solution.

4.3 Steady Operation

During steady reactor operation, the inlet temperature to the upper plenum will remain constant due to a constant power input from the reactor core. After a sufficient time in steady operation, the incoming fluid and the bulk of the pool are expected to have the same temperature (823.15 K). Due to the spatial proximity of the IHX and the upper plenum, the upper plenum will experience heat losses at the right boundary that is connected to the IHX. These heat losses are represented by the thermal boundary conditions as described in the previous section. This simulation is used to determine whether a true steady state can be reached for the flow in the upper plenum when heat losses are considered. Further, the time to reach steady state will be recorded. Additionally, the simulation serves to confirm the simulation setup in a more challenging scenario.

As shown in Figures 4.5 and 4.6 the flow shows the momentum driven solution although Mesh 6 originally showed the buoyancy solution during the mesh analysis. The change in solution is attributed to the slight change in boundary conditions from completely adiabatic to heat losses on the right wall. A possible explanation is that the down flow from the primary jet is now heavier than before and thus diverts the second jet more effectively. However, the change in solution casts doubts on the fidelity of the simulation. As mentioned in Section 4.2 this problem has been encountered by other researchers and has yet to be solved. The right images in the aforementioned figures show the difference between the solution at 80 s and 160 s. As evident, the flow does not change significantly after 80 s, and most of the domain shows no difference at all with only small regions of up to 0.14 m/s difference. The differences for the temperature are similarly small. Most of the enclosure has a temperature difference of less than 0.25 K. The left image in Figure 4.6 shows that the temperature in the enclosure is very uniform at 823 K. Only regions close to the colder walls show slightly lower temperatures. The top and bottom sections of the wall show small downward plumes created by the colder, denser fluid.

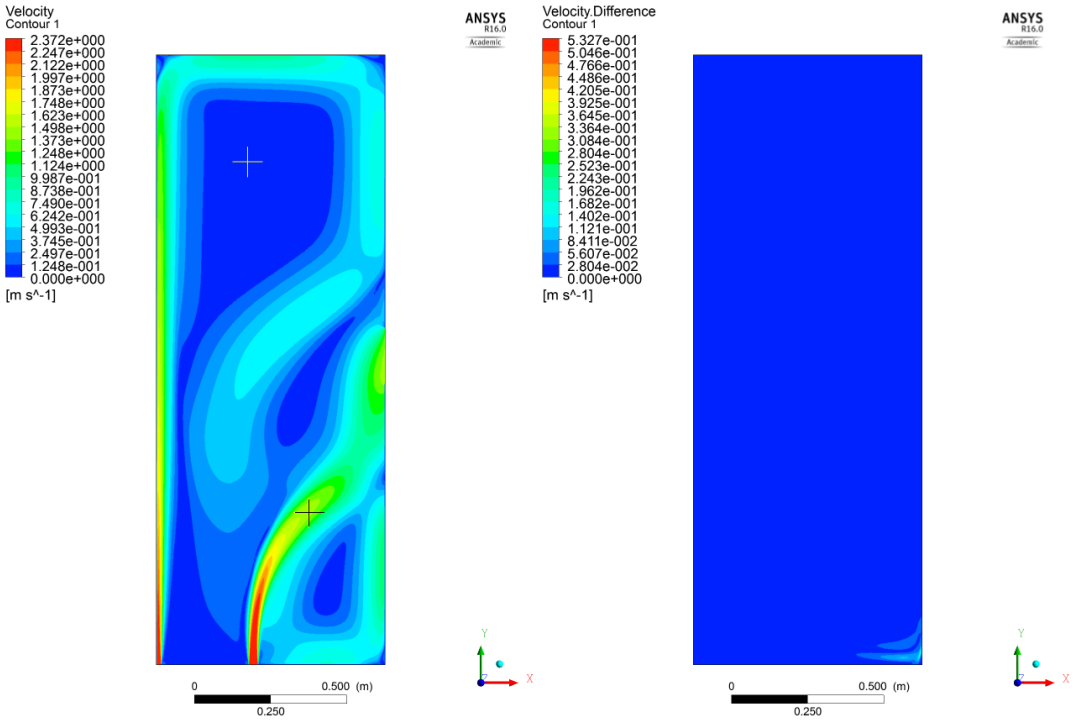

Figure 4.5: Left: Velocity contours for case with heat losses after 160 s. The crosses indicate the test points referenced in Figure 4.7. Right: Difference in velocity for solutions after 80 s and 160 s.

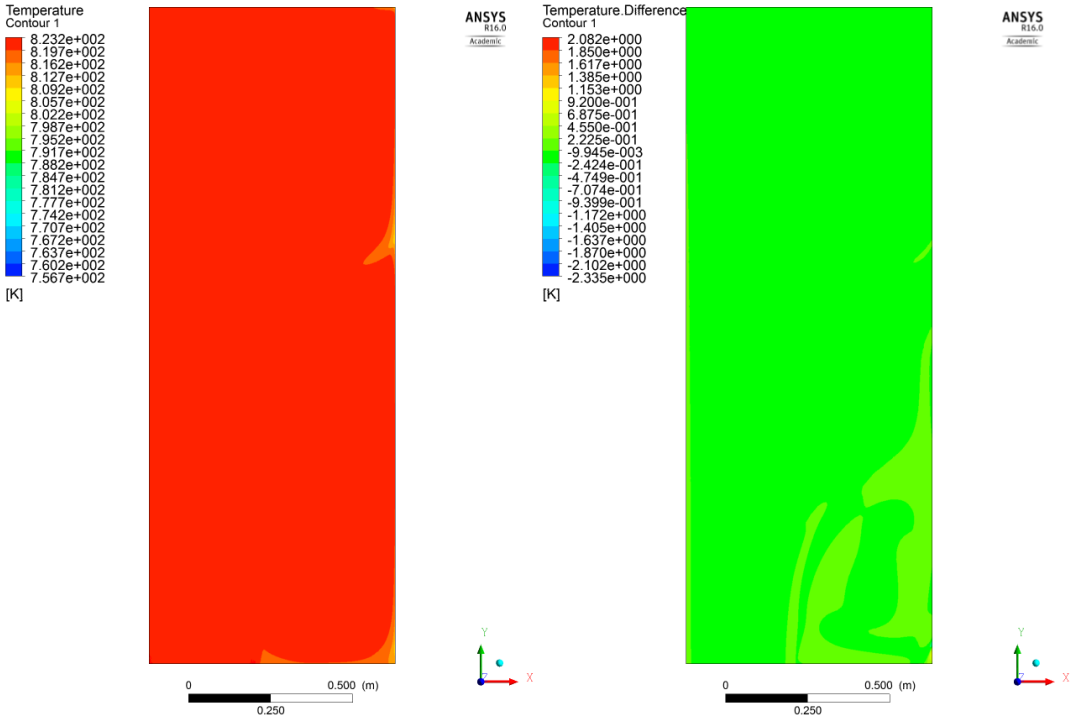

Figure 4.6: Left: Temperature contours for case with heat losses after 160 s. Right: Difference in temperature for solutions after 80 s and 160 s.

Figure 4.7 shows the evolution of the temperature at two test points. Test point 1 was chosen because it is believed to be one of the last points to achieve steady state. Point 1 is located in an area of low flow velocities and thus will be more influenced by slower mechanisms of heat transfer. The graph shows that the temperature fluctuates with an amplitude of up to 0.3 K during the first 60 seconds, then steadies and finally declines. The fluctuations and overall change in temperature are very small. In the steady decline phase, the temperature decreases by 0.2 Kelvin per minute. A likely reason for the slow change in temperature is that the cold fluid along the walls is removed quickly through the downward jet that is then mixed with the second jet and leaves the domain through the outlet. The interaction with the surrounding undisturbed fluid is minimized by this process, explaining the small influence on the temperature at the test point. The fluctuations during the initial phase of the flow are a result of the changing flow field that has not yet reached its steady state configuration. Point 2 is located in the second jet. The temperature at this point drops quickly during the first 20 seconds of the simulation and then becomes fairly steady at approximately 40 seconds. Slight temperature oscillations can be observed due to the inlet jet. The large temperature decrease in the beginning is caused by entrainment of colder fluid from the wall jet.

The steady change in temperature for Point 1 and the slight oscillation for Point 2 are sufficiently small to conclude that the solution has essentially reached steady state. Streamlines and vectors are included in Appendix A.

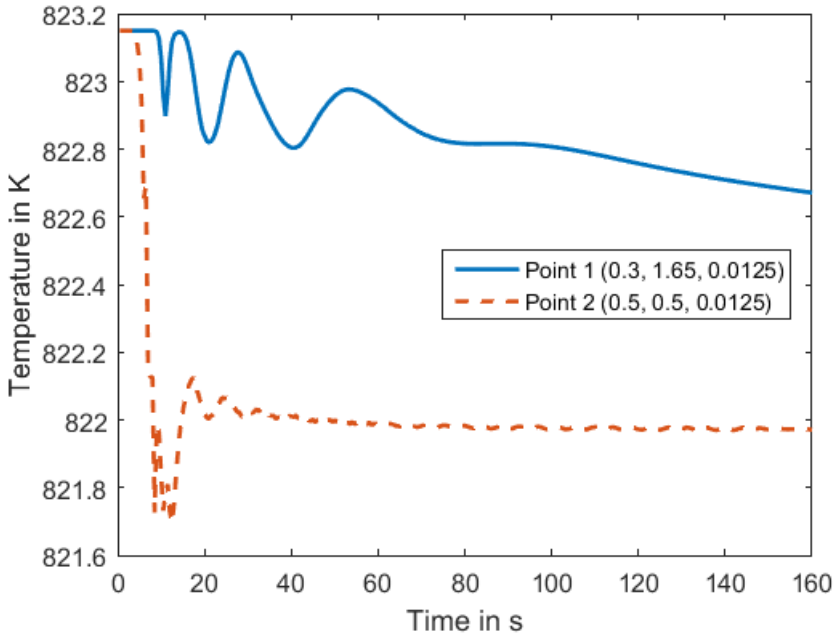

Figure 4.7: Temperature history at two test points. Note the scale of the temperature axis on the left side.

4.4 Simple Transient

After determining the steady state solution, transient simulations were conducted on all three designs. The purpose of these simulations is to investigate thermal stratification in the upper plenum. Stratification occurs primarily when cold fluid is injected into a hot plenum as occurs during a reactor scram. Realistically, the input temperature to the upper plenum will decay after a reactor scram. Grandy et al. show a plot of this temperature variation in their report for the AFR [63]. As a first approximation, a step function is assumed for the temperature variation for this first case labeled 'simple transient'. The simulation is initialized at the steady state operating temperature of 823.15 K. The incoming sodium is at 773.15 K, the coldest temperature during a protected accident. The setup thus corresponds to a 'worst case' scenario in terms of maximum temperature difference. The flow rate is maintained at its steady state value for this simulation. A more challenging case with changing inlet temperature and flow rate based on the Unprotected Loss of Flow (ULOF) accident presented by Grandy et al. will be investigated in Section 4.5.

4.4.1 Case 1

Case 1 refers to an upper plenum with one large inlet as depicted in the AFR-100 report [11]. Due to the large inlet, the inlet velocity for this design is lower than that for the other two cases. A lower velocity leads to a smaller jet which in turn leads to more stratified conditions. Velocity and temperature contours at selected times are shown in Figures 4.8-4.13. The contours show a very clear and stable stratification interface that moves upwards as the transient progresses. The upward movement slows down significantly when the stratification interface is higher than the outlet because the incoming flow passes through the enclosure without interacting with the interface. After the interface completely passes the outlet, the main mode of heat transfer to the hot fluid is conduction through the interface. The resulting temperature gradients lead to a broadening of the previously well defined interface.

Figure 4.14 shows the height of the stratification interface over the course of the transient. The position of the interface is defined as the vertical position where the horizontal line average of $\partial T/\partial y$ is highest. After the interface rises to about 1.3 meters in 20 seconds, its movement slows until about 180 seconds. Between 180 and 250 seconds the interface rises quickly before slowing down again. The second interval of quick movement is characterized by a shift of the peak gradient as shown in Figure 4.15. As the peak broadens and shifts, the calculated position of the interface changes, even though the temperatures are fairly constant.

Figure 4.16 shows the average and maximum temperatures of the upper plenum, as well as the mass flow averaged outlet temperature. The outlet temperature reaches a steady value after about 20 seconds, the same time it takes for the stratification interface to move past the inlet. Once the hot fluid is pushed past the outlet by the incoming cold fluid, the outlet temperature remains fairly constant at approximately the inlet temperature of 773.15 K. It takes much longer, about 180 seconds, for the maximum temperature to change. This is due to the insulation provided by the stratification interface. The average temperature decreases quickly during the first 10 seconds and then continually decreases at a slower pace. At around 600 seconds the average temperature decreases below the outlet temperature. This is due to the increased influence of the cold walls.

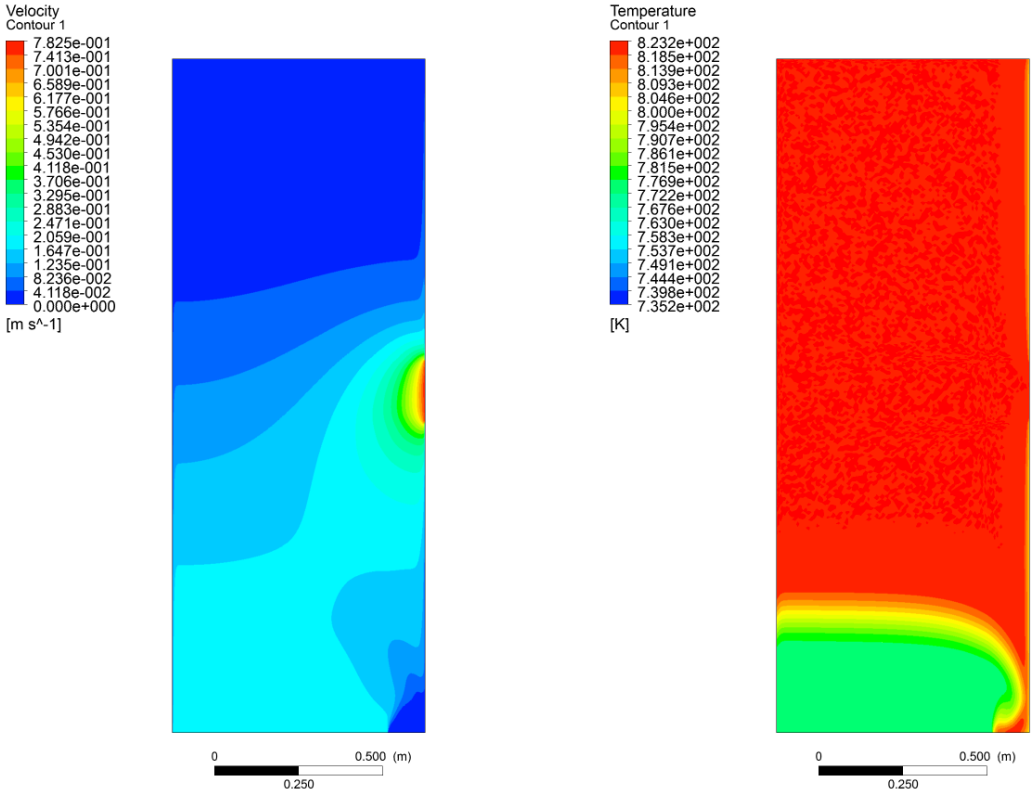

Figure 4.8: Velocity and temperature contours after two seconds for Case 1.

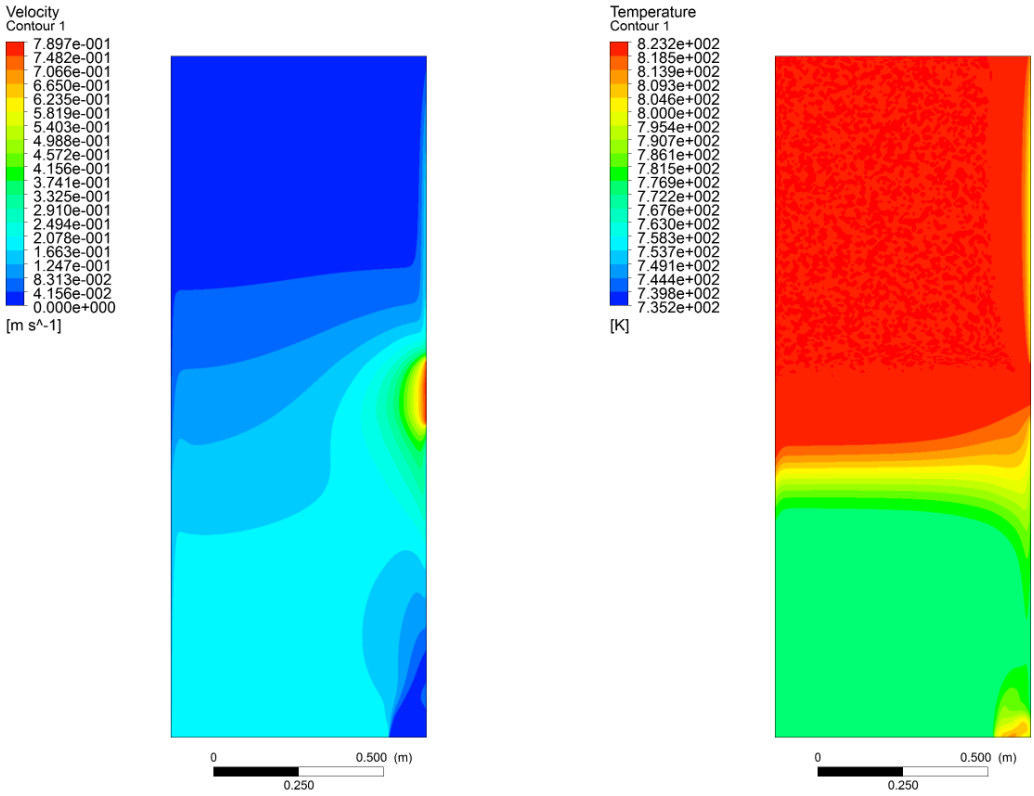

Figure 4.9: Velocity and temperature contours after five seconds for Case 1.

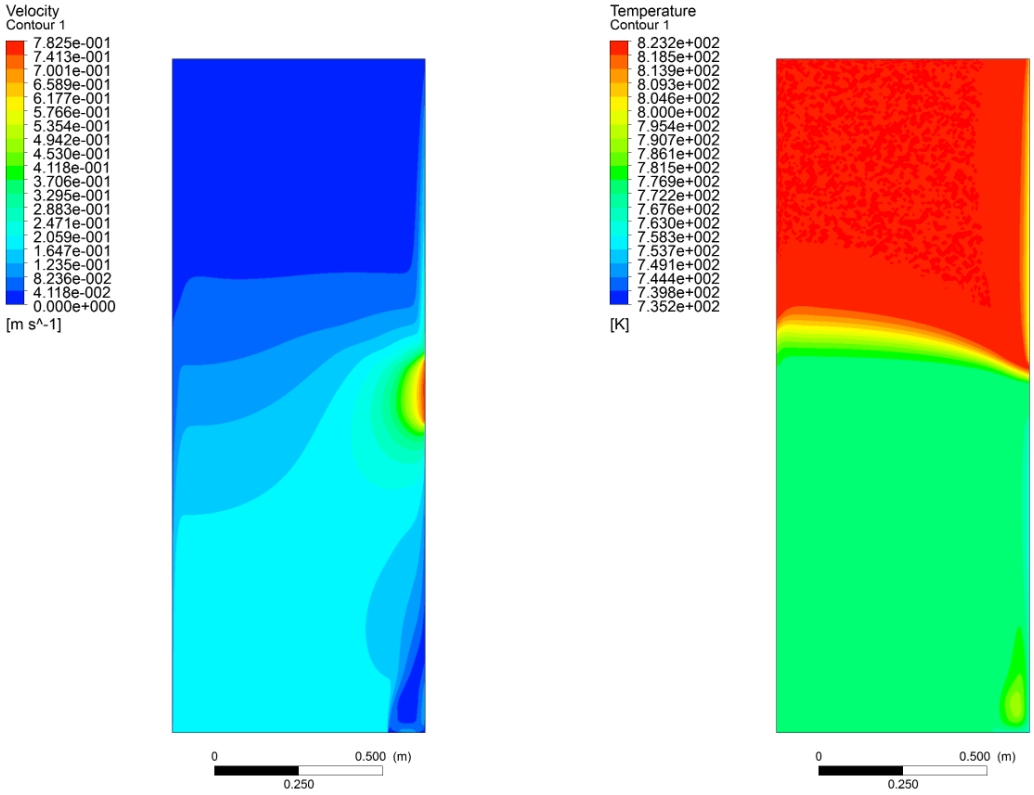

Figure 4.10: Velocity and temperature contours after ten seconds for Case 1.

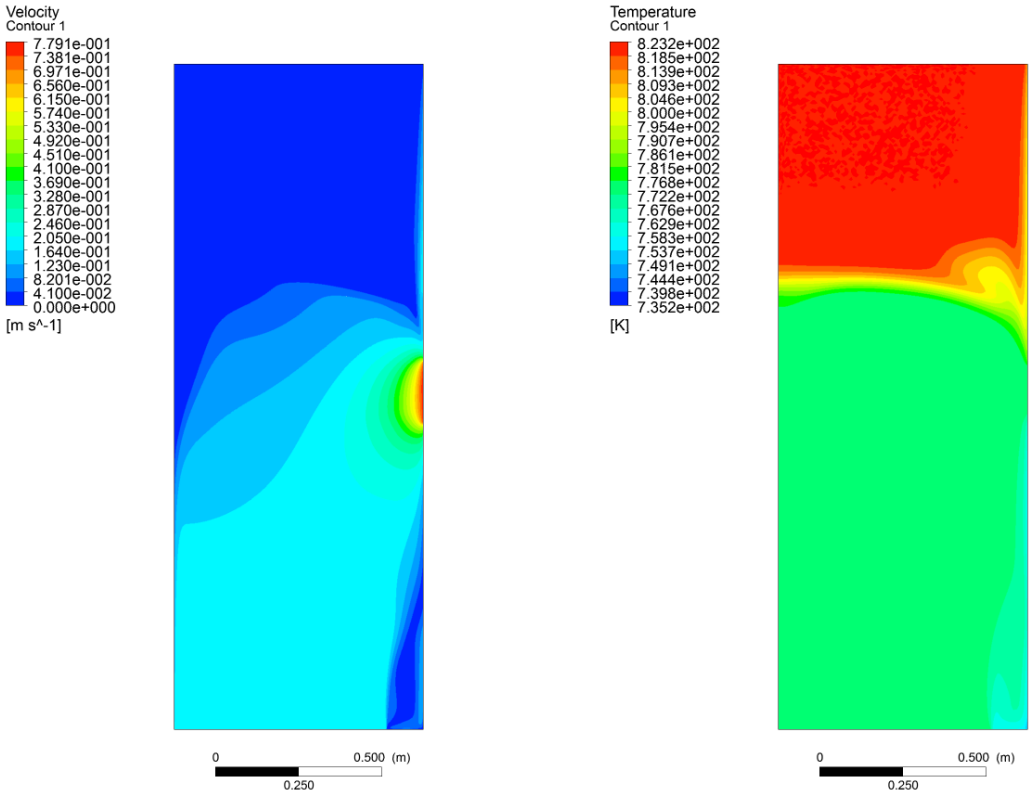

Figure 4.11: Velocity and temperature contours after 25 seconds for Case 1.

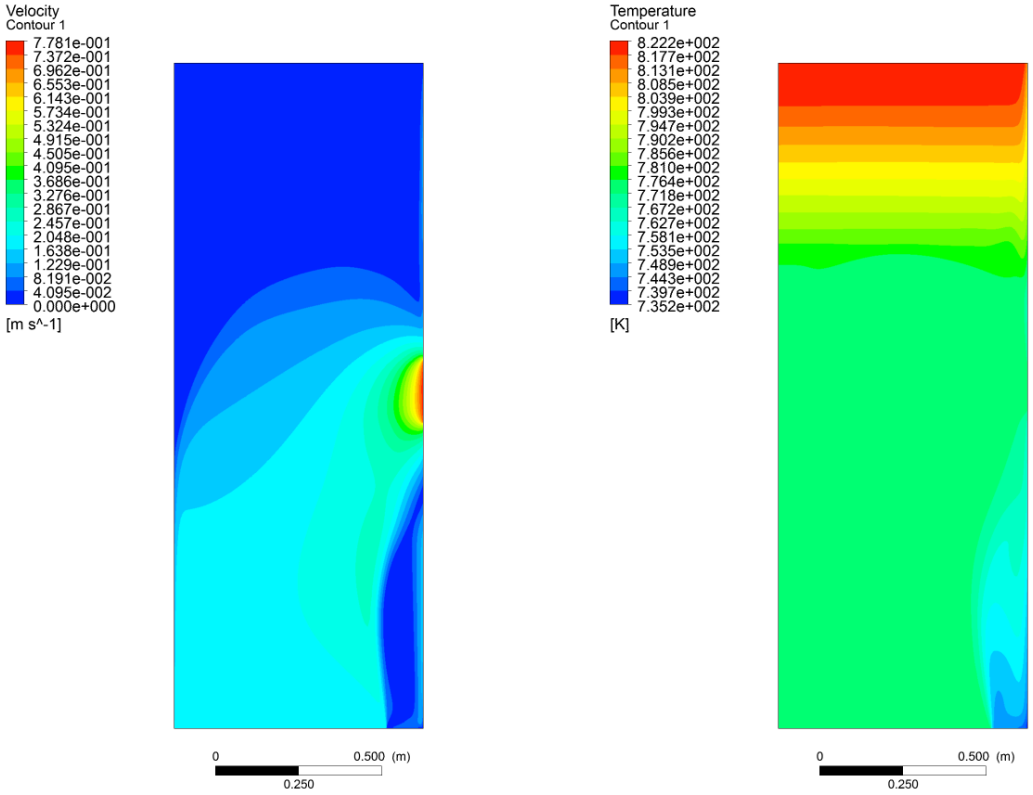

Figure 4.12: Velocity and temperature contours after 160 seconds for Case 1.

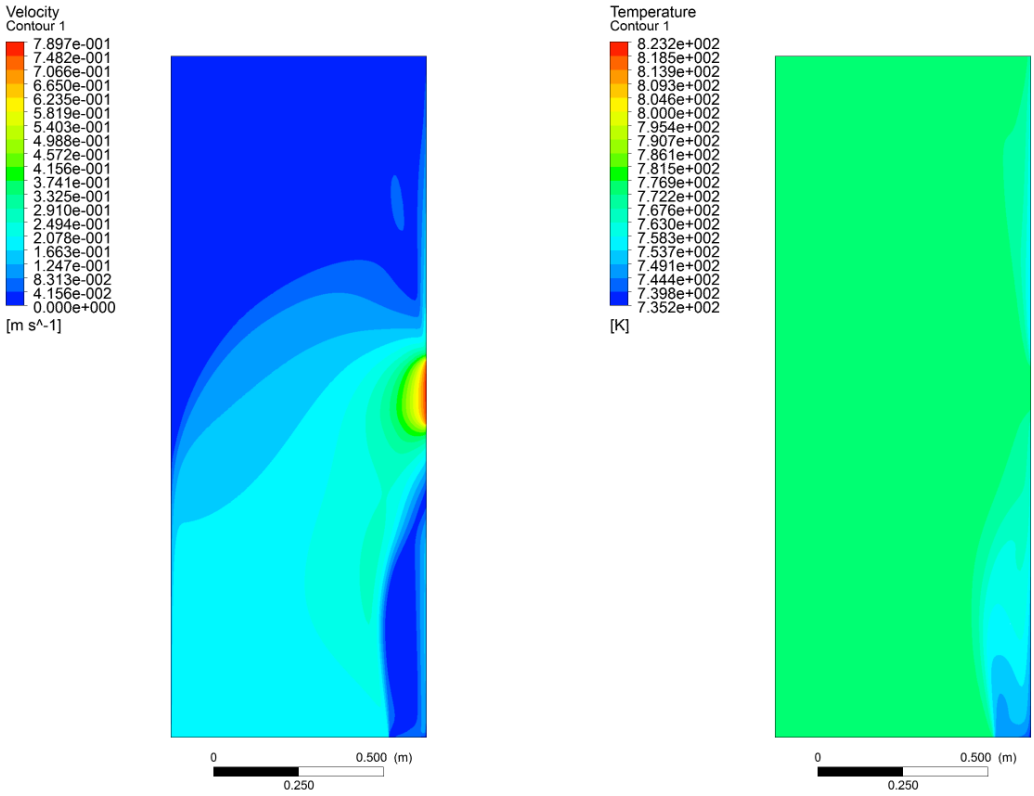

Figure 4.13: Velocity and temperature contours after 12 minutes (720 seconds) for Case 1.

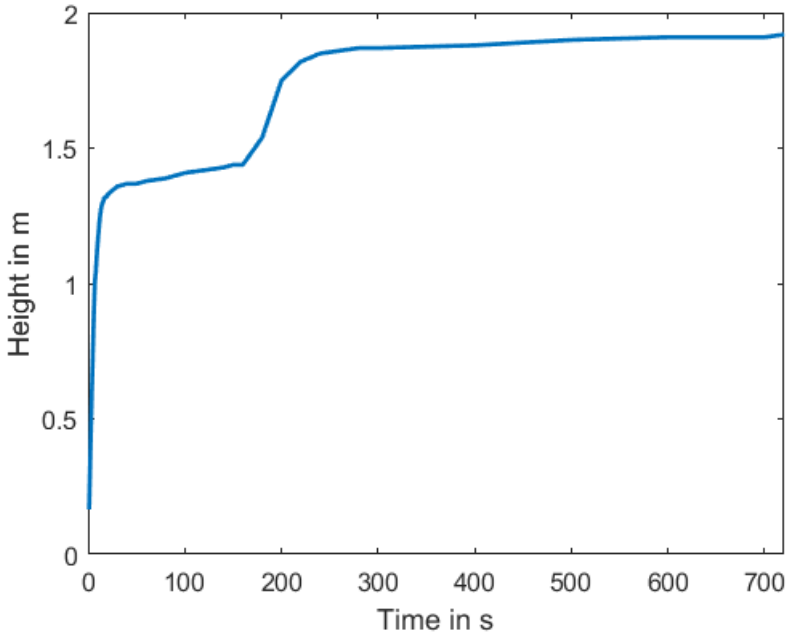

Figure 4.14: Vertical position of the stratification interface over the course of the transient for Case 1.

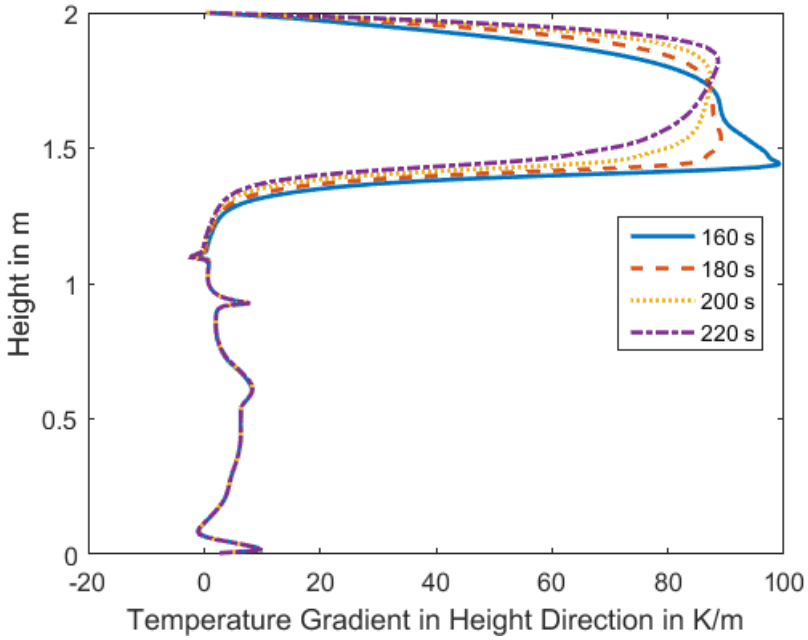

Figure 4.15: Vertical temperatures gradients at selected times for Case 1. Note the upward shift and reduction in magnitude of the maximum gradient.

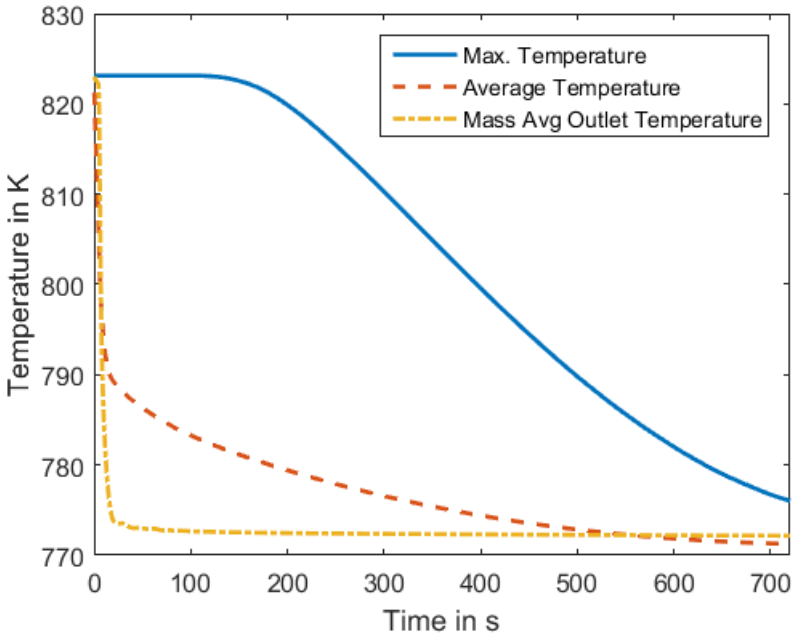

Figure 4.16: Change of maximum temperature, average temperature, and mass flow averaged outlet temperature of the upper plenum for Case 1.

4.4.2 Case 2

In Design 2 the inlet is changed to include 4.5 inlet nozzles. The half nozzle is a result of the symmetry plane in the middle of the enclosure. The flow rate remains unchanged from the previous design but the velocity is increased from 0.175 m/s to 0.778 m/s to compensate for the reduced flow area. The jets are spread evenly from the middle of the enclosure to 0.64 m from the left edge so that the last nozzle coincides with the edge of the large inlet in Design 1.

The temperature and velocity contours presented in Figures 4.17 to 4.21 show a less defined stratification interface than for Case 1. The interface moves up very quickly and completely moves past the outlet at 17 s. The interface is also slanted from left to right with an decreasing angle. The time histories of average temperature and outlet temperature are depicted in Figure 4.23. The average temperature and outlet temperature drop more quickly than for Case 1 due to the higher jets in Case 2. The higher inlet velocity leads to jets that reach further into the domain. The maximum temperature shows the same general trend as for Case 1, remaining constant for 75 seconds before declining rapidly after approximately 90 seconds. The drop in maximum temperature occurs sooner for Case 2 and the decline is steeper than for Case 1. Case 2 also shows more oscillations in the outlet temperature due to fluctuations caused by the higher jet velocity. These fluctuations are visible in the velocity contours of Figures 4.17 and 4.18. The contours also show that the height of the jet on the symmetry plane increases as the transient progresses. As long as the stratification interface persists, the jet is restricted in its height by the interface. As the interface moves upwards so does the jet. The final contour at 150 s shows the jet reaching the top of the enclosure where it changes direction. The jet then descends down toward the inlet where it mixes with the second jet. During the middle part of the transient the first jet is redirected by the stratification interface but shows a similar overall flow pattern with eventual mixing with the second jet. Figure 4.20 shows that a hotter area forms between the down-coming flow of Jet 1 and the combined flow of the other jets. The stratification interface is much broader on the right side than on the left indicating that heat transfer by conduction has a larger influence in this region.

Figure 4.24 shows the temperature distribution in the enclosure at selected times. The overall shape is similar to the results from Sofu et al. (see Fig. 2.4). The shape of the profiles seems to transition around 50 seconds as lower temperatures reach further into the enclosure.

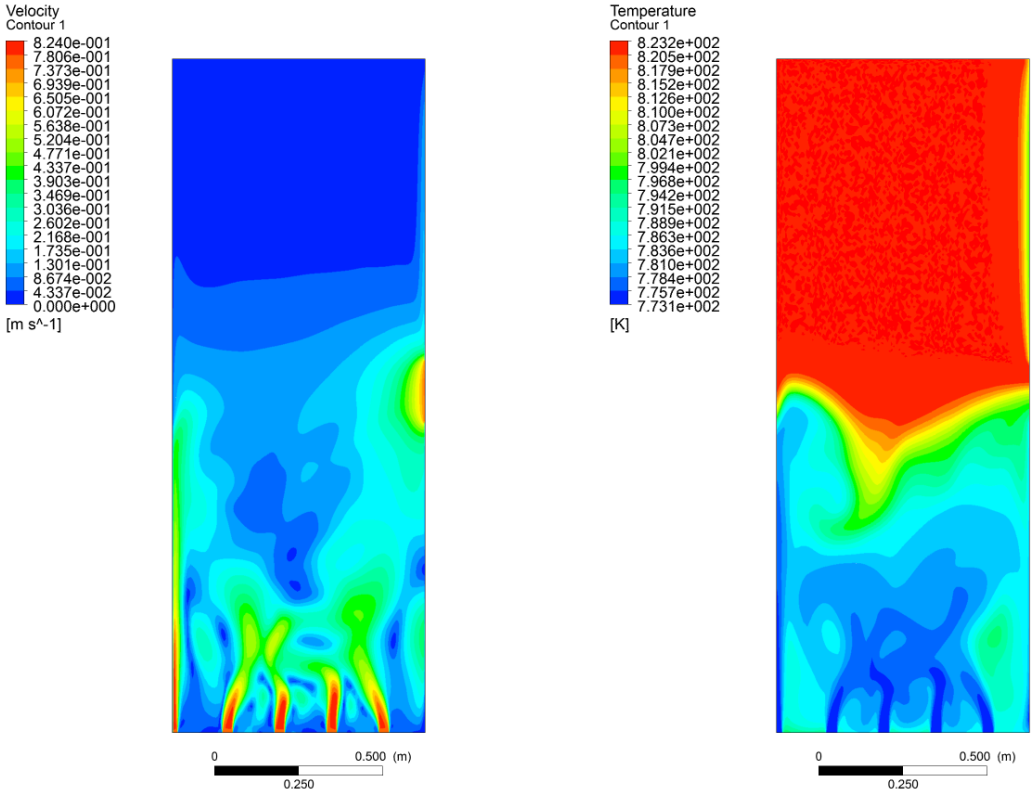

Figure 4.17: Velocity and temperature contours after five seconds for Case 2.

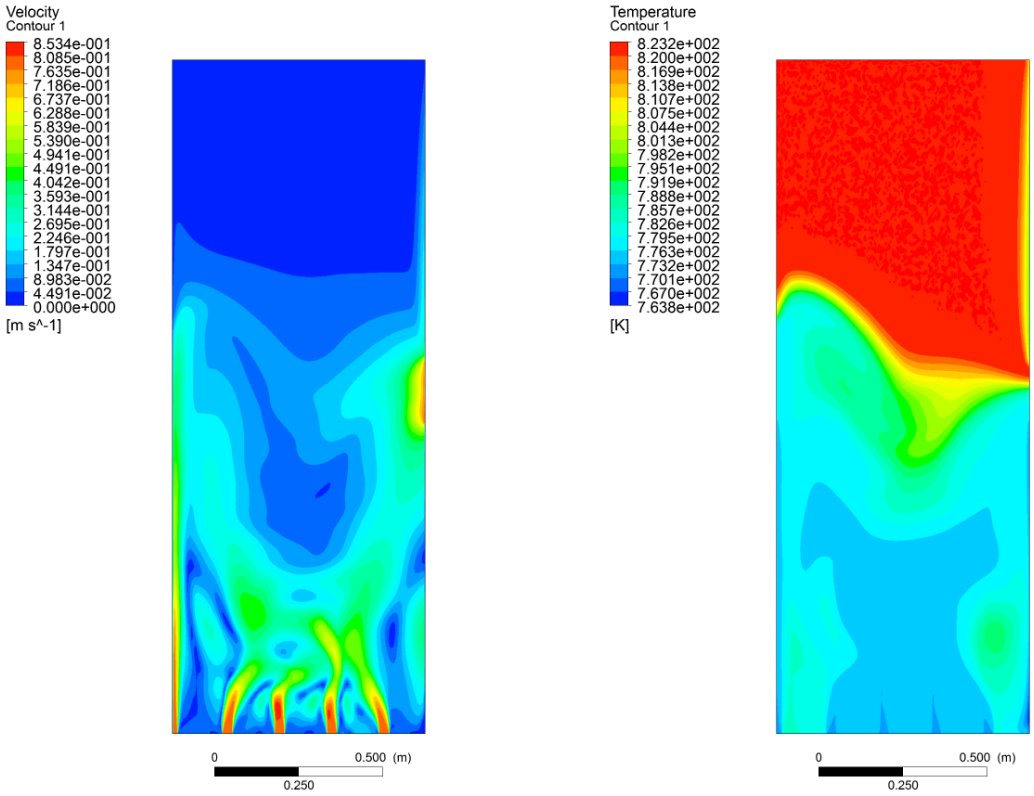

Figure 4.18: Velocity and temperature contours after eight seconds for Case 2.

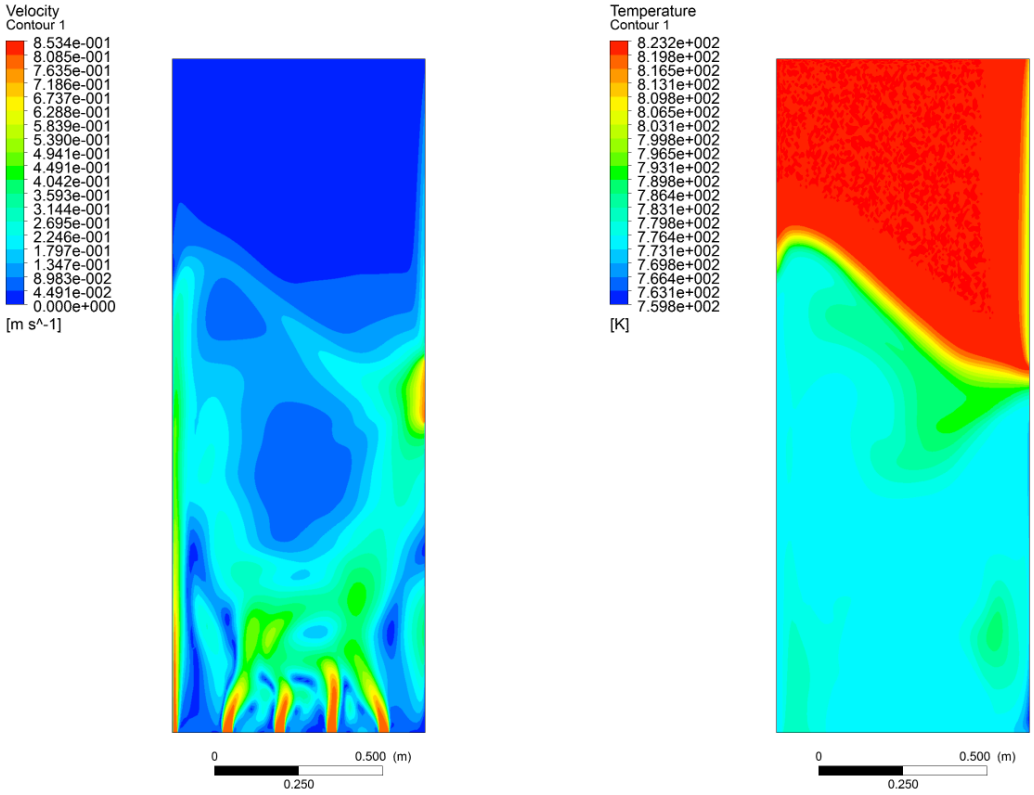

Figure 4.19: Velocity and temperature contours after ten seconds for Case 2.

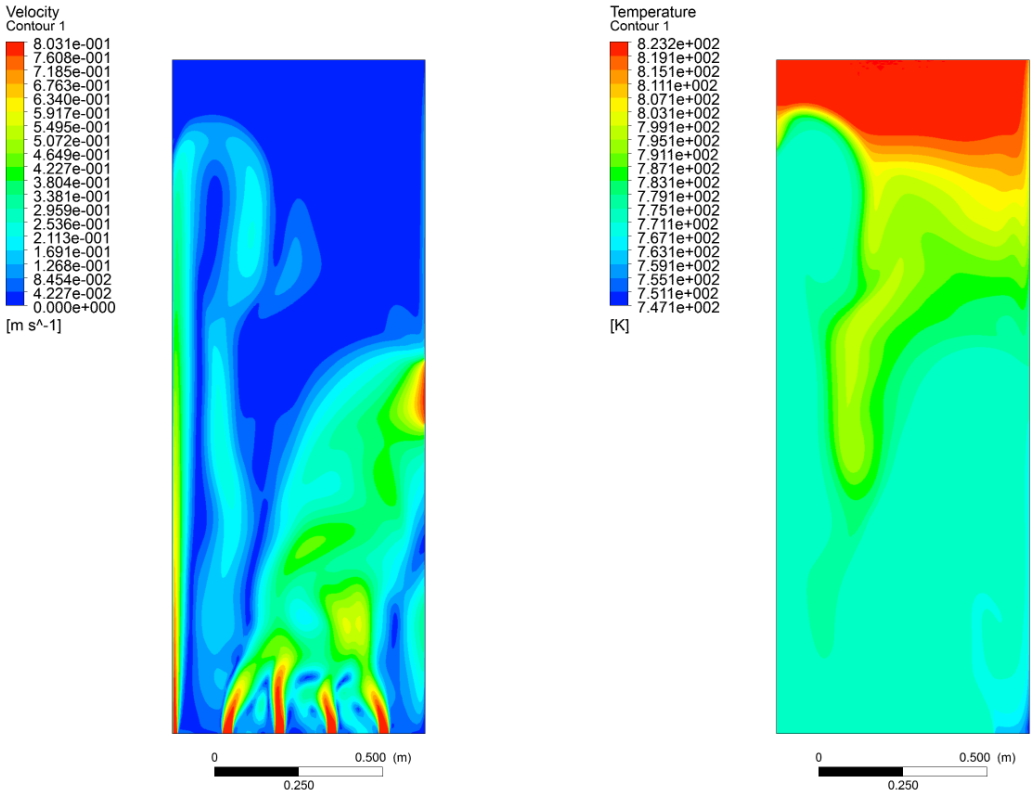

Figure 4.20: Velocity and temperature contours after 50 seconds for Case 2.

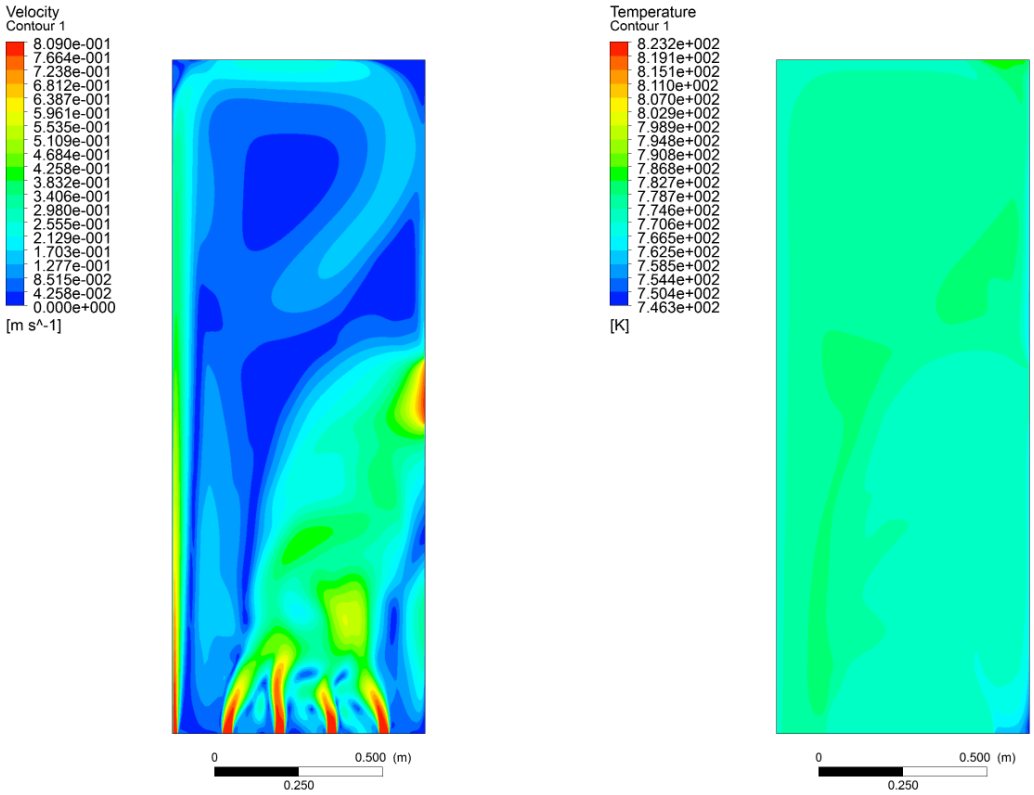

Figure 4.21: Velocity and temperature contours after 2.5 minutes (150 seconds) for Case 2.

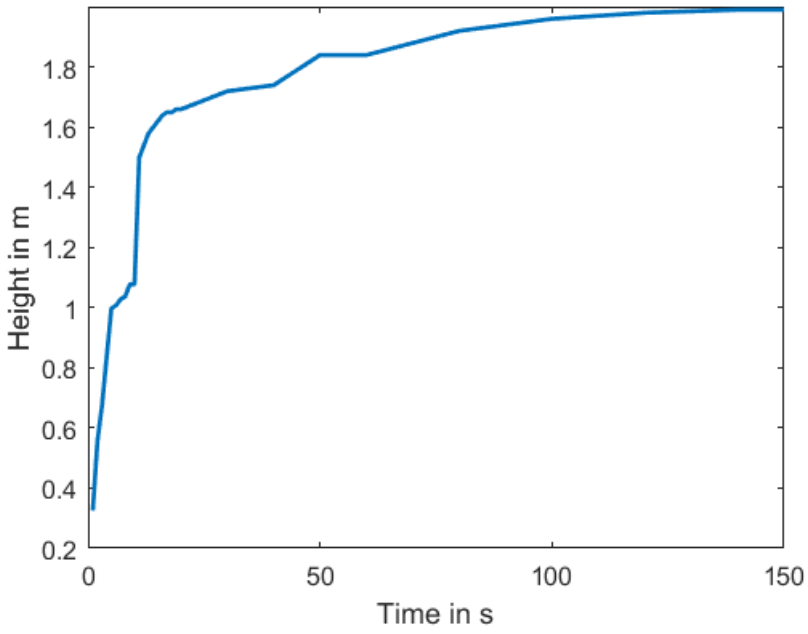

Figure 4.22: Vertical position of the stratification interface over the course of the transient for Case 2.

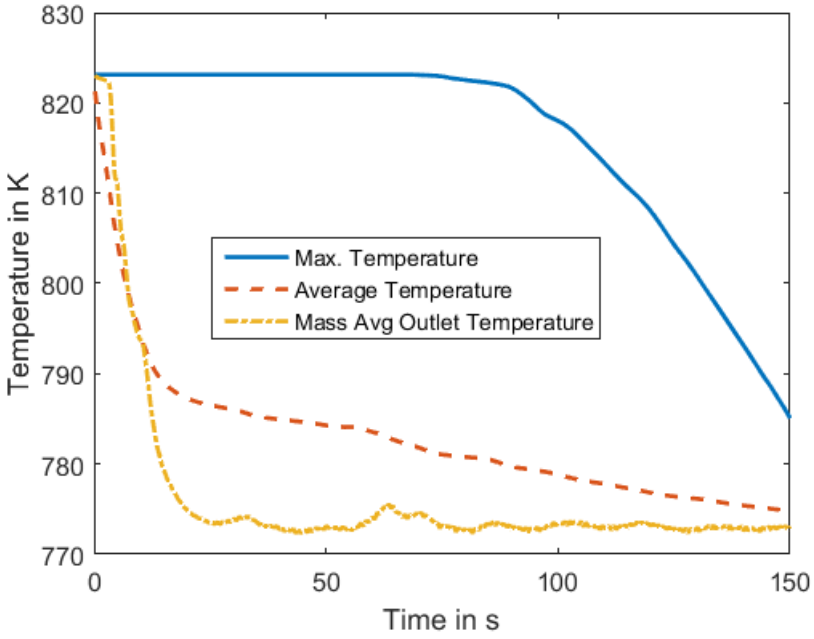

Figure 4.23: Change of maximum temperature, average temperature, and mass flow averaged outlet temperature of the upper plenum for Case 2.

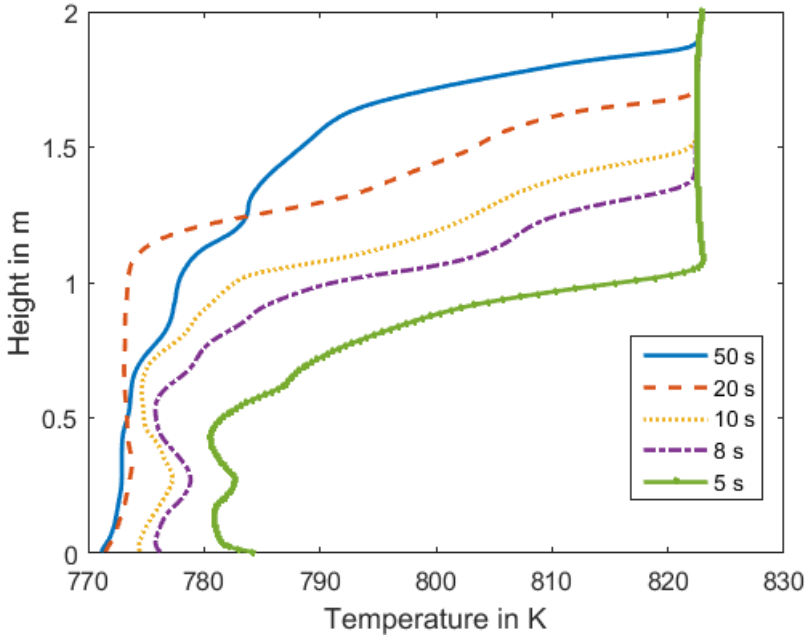

Figure 4.24: Temperature distribution at selected times for Case 2.

Symmetry vs Wall Boundary

Case 2 was also used as a reference design to investigate the influence of two other factors on the simulation, namely the boundary condition at the front and back walls, and the cooling medium. As mentioned in Section 4.1, the front and back walls were modeled with a wall boundary condition. This represents the test stand but not a full reactor. To gauge the effect of this boundary condition on the overall results, and to estimate the differences between a full reactor and test facility, this boundary condition was changed to a symmetry plane. A symmetry boundary condition sets all gradients normal to the wall to zero. In terms of the thermal boundary conditions, this has no influence on the result because the walls were already modeled as adiabatic. Similarly, the symmetry condition does not change the flow velocity normal to the wall which is zero for both boundary conditions. The difference to the wall boundary is observed in the flow velocity parallel to the walls. For a wall boundary, this velocity is set to zero due to the no-slip assumption at the wall. Conversely, the symmetry boundary sets the horizontal gradient of the vertical velocity to zero, making the velocities on both sides of the wall equal.

Figure 4.25 shows a comparison of the position of the stratification interface for both boundary conditions. The results agree very well for the first eight seconds. After that the interface for the symmetry case rises quickly to around 1.35 m at which point the rising slows down drastically. The interface for the wall case rises later, at 10 s, from 1 m to 1.5 m, and reaches 1.62 m after 16 s compared to 1.40 m for the symmetry boundary. The case with the wall boundary rises faster than the symmetry case after the initial jump. Since the flow rates and thus the average velocities of both cases are the same, the maximum velocity in the wall boundary case will be higher to compensate for the velocity drop at the wall. This could lead to a faster rise of the interface. However, this does not explain why the case with the symmetry boundary shows its jump in the interface position two seconds before the wall case. The reason could be that the temperature interface is flatter for the symmetry case. The flatter shape results in a more defined position of the interface. For the distorted shape shown in Figure 4.18 it is difficult to select a single value for the height of the interface. The procedure presented in Section 4.4.1 results in a height of approximately 1 m. The Figure 4.18 shows that any value in the range of 0.95 m to 1.3 m would be valid. The issue of pinpointing the exact location of the interface is likely a major contributing factor to the differences. However, it is also obvious that the interface moves more uniformly for the case with the symmetry boundary condition. The jet on the left side of the enclosure is shorter for the symmetry case which depresses the large spike seen with the wall boundary. Since both cases have the same mass flow rate, this fluid is found elsewhere in the enclosure, raising the interface more uniformly. Due to this uniform movement, the interface passes the outlet first in the symmetry case which explains the earlier jump. The reduction in jet height is caused by the lower maximum velocity in the symmetry case due to a flatter velocity profile in the thickness direction (see Figure 4.27). This is the same effect that is seen comparing the cases with different numbers of nozzles where the maximum velocity is the main cause for high jets.

Figure 4.26 shows the variation of average and outlet temperatures over time. There is good agreement for both cases although the outlet temperature of the wall boundary is not as smooth as for the symmetry boundary. Figure 4.27 shows the velocity profiles for the case with a wall boundary, symmetry boundary, and using gallium. As expected, the velocity for the symmetry case is flat across the thickness direction due to the absence of wall shear, and to conform to the symmetry condition. The wall boundary case shows a well-developed turbulent profile with a maximum around 0.4 m/s. For fully developed turbulent flow in pipes, the average velocity is approximately $0.82 v_{max} = 0.33\ m/s$. The constant velocity for the case with symmetry boundary is around 0.27 m/s. The discrepancy to the theoretical value is due to the fact that the flow is not fully developed and not a pipe flow.

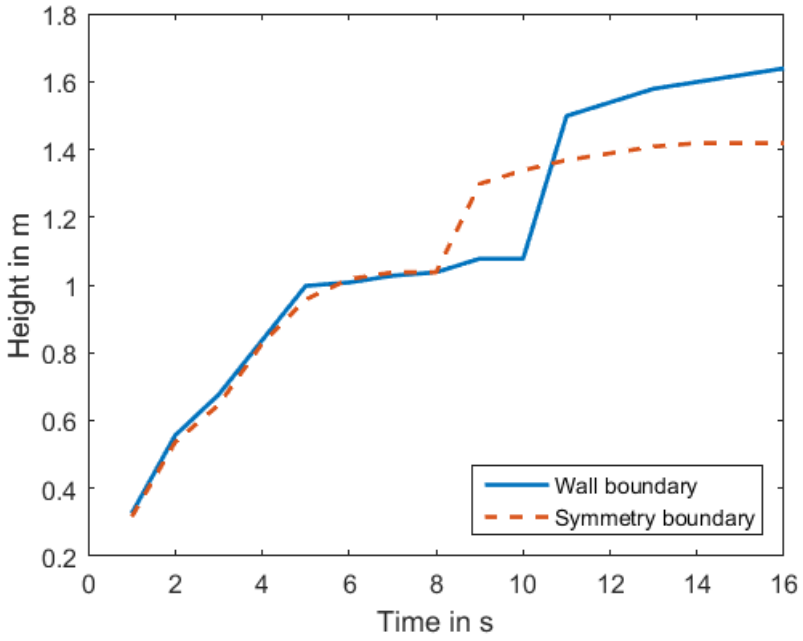

Figure 4.25: Comparison of the vertical position of the stratification interface for symmetry and wall boundary conditions for Case 2.

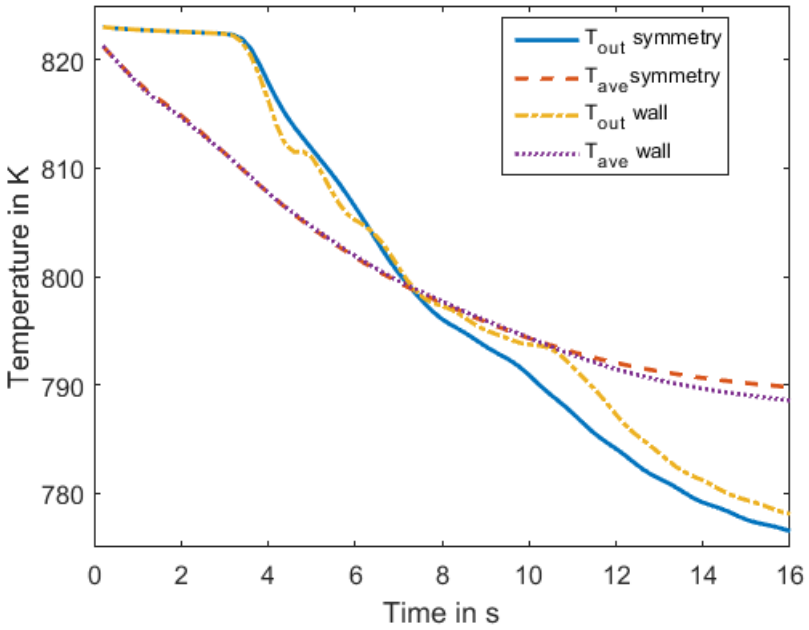

Figure 4.26: Change of the average temperature, and mass flow averaged outlet temperature of the upper plenum for Case 2 using symmetry and wall boundary conditions on the front and back wall.

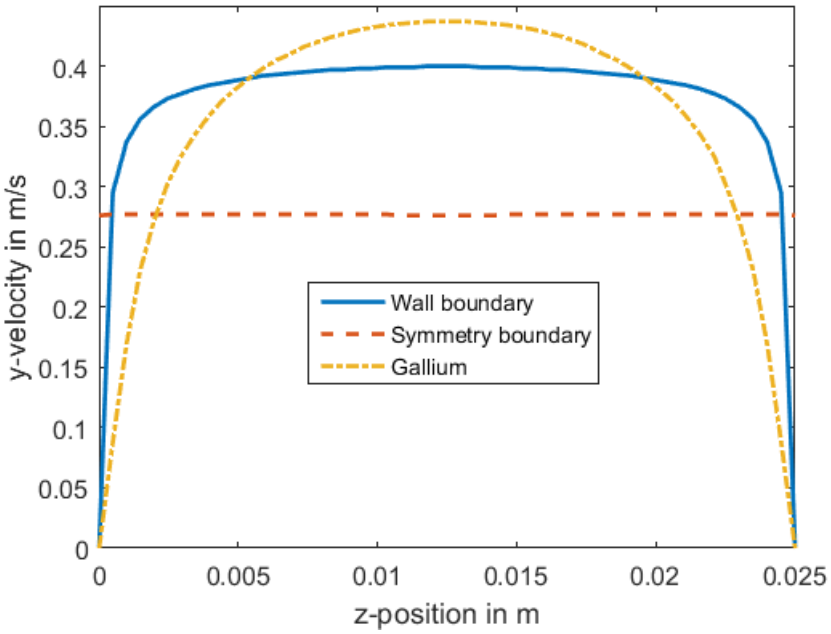

Figure 4.27: Profile of the vertical (y) velocity in thickness (z) direction.

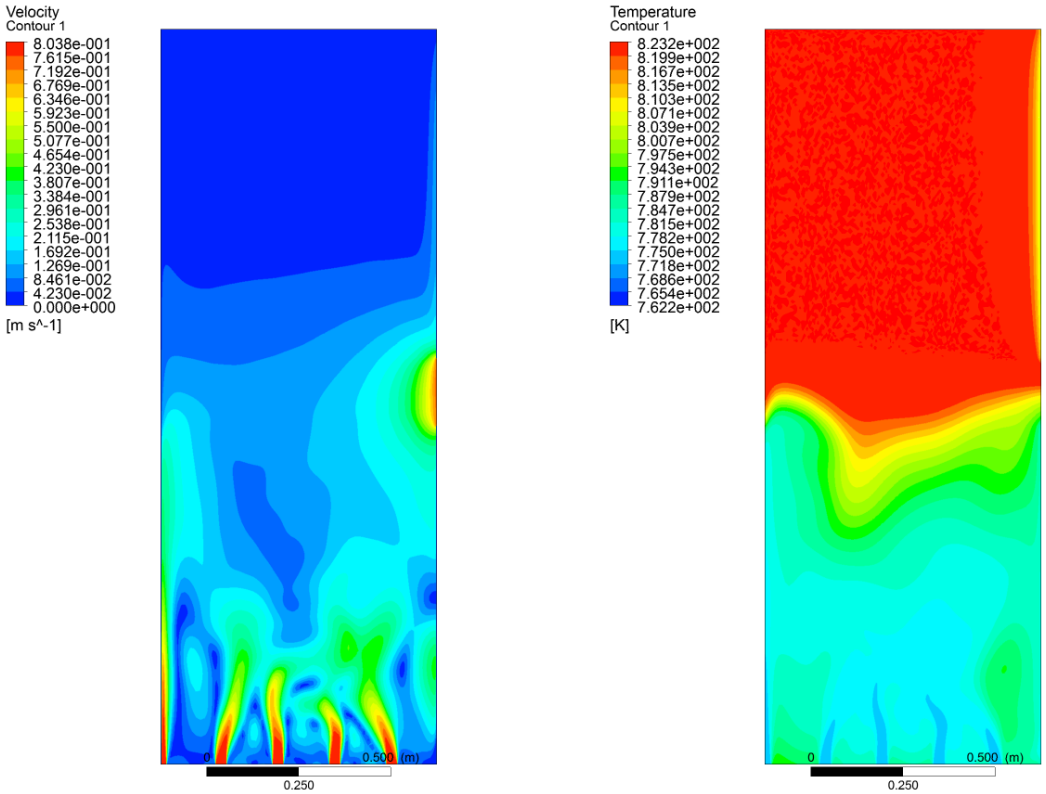

Figure 4.28: Velocity and temperature contours after five seconds for Case 2 with symmetry boundary.

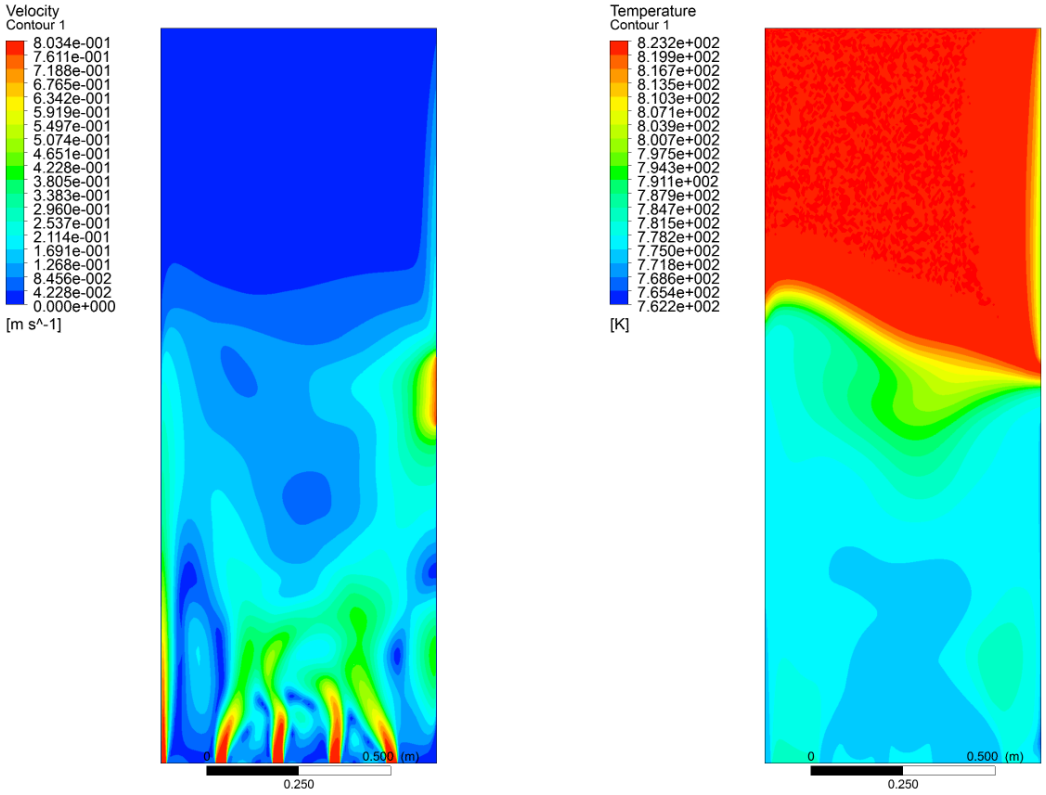

Figure 4.29: Velocity and temperature contours after eight seconds for Case 2 with symmetry boundary.

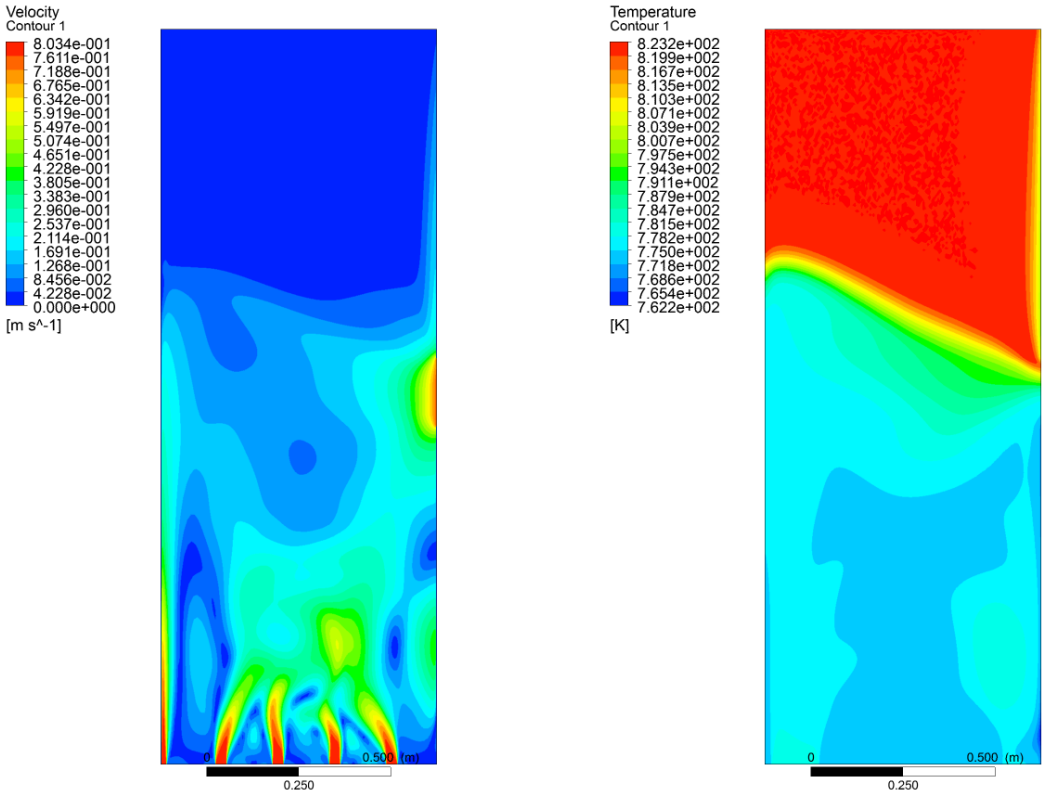

Figure 4.30: Velocity and temperature contours after ten seconds for Case 2 with symmetry boundary.

Sodium vs Gallium

Further studies were performed on Case 2 to evaluate the differences between sodium and gallium as reactor coolant. This is important because the proposed test facility would use gallium as a coolant to reduce the safety risks associated with sodium. The lower melting point of gallium compared to sodium is one of the reasons why it was chosen for the test loop instead of sodium. Both fluids are expected to perform similarly in terms of flow and heat transfer. Two studies were performed to validate this assumption. One simulation was conducted at the same inlet and outlet temperature and flow rate as the original Case 2. A second study was performed with the same flow rate but changed temperatures. This simulation is more relevant because the test loop using gallium would operate at significantly lower temperatures to take advantage of the low melting point of gallium. The inlet velocity was kept the same between the gallium simulations but the temperatures were scaled to leave the Richardson number unchanged.

The rising of the stratification interface for all three cases is shown in Figure 4.31. The plot shows good agreement between the sodium and the unscaled gallium simulation although the interface for the gallium case lags behind the sodium interface. During the first phase of rapid upward movement, the unscaled gallium interface is about half a second behind the sodium interface. Between 6 and 10 seconds both interfaces are at the same location. The fast upward movement occurs at the same time for both cases but the magnitude of the change is about 10 cm less for the gallium simulation. After the jump, the upward movement has the same slope for both fluids.

The scaled gallium simulation agrees well with the unscaled simulation for the first 8 seconds. After that the scaled simulation shows a small jump and then a continuous upward motion. The overall shape is similar to the unscaled gallium and the sodium result. It is clear however, that significant differences are present between the cases. If the reactor is to be simulated using a scaled gallium scenario, the interface will show somewhat different behavior. From 4.31 it can be inferred that the stratified stage will last longer using gallium.

A transient history of the outlet and average temperature for sodium and the unscaled gallium simulation is shown in Figures 4.26. The average temperatures agree very well as expected from the fact that both cases have the same flowrate and inlet temperature. The difference in the average temperature is about 1 Kelvin after 16 seconds. The difference is likely due to a changed heat transfer coefficient at the cold walls. There is less agreement for the outlet temperature. Both curves follow the same general trend and agree well after about 8 seconds. Before 8 seconds there is some disagreement, likely due to the difference in the position of the interface that was described in the previous paragraph. The gallium simulation shows a large bump between 4 and 6 seconds where the temperature increases for about two seconds.

The Richardson scaled gallium simulation shows the same pattern as both of the other simulations. The pronounced bump in the outlet temperature seems to be smaller than in the non-scaled gallium simulation but larger than in the sodium simulation. Overall, there is good agreement between all three simulations.

Figures 4.33 to 4.35 show velocity and temperature contours for the unscaled simulation using gallium. Comparison with the contours for the simulation using sodium reveals that the left jet is less pronounced for the case using gallium. The interface is also less smooth for the gallium case especially at 5 and 8 seconds. The left jet remains lower for the gallium simulation even at 10 seconds and as a result, the stratification interface is less steep. The contours for the scaled simulation can be found in Appendix B. The interface for the scaled case is smoother than for the unscaled case but shows a very similar overall shape. Both gallium simulations have a flatter interface than the sodium case. The velocity contours are

in good agreement between the two gallium simulations.

Overall, there is good agreement between the sodium and gallium simulations and it seems justified to use gallium as a coolant to reduce experimental risk. However, Figure 4.31 clearly shows that the stratification behavior will be different for gallium, especially when the conditions are scaled by Richardson number. The interface in the scaled gallium simulation rises more slowly than sodium in the beginning and has a much smaller jump. This leads to an interface that is about 20 cm lower at 16 seconds than the corresponding sodium simulation. It should be noted that data on the thermal and fluid properties of gallium is sparse. The properties for the simulation were taken from an IAEA publication which in turn republished data from three Russian publications from the 1990s [64]. The dynamic viscosity was not included and had to be calculated from the provided relations for the density and kinematic viscosity using a curve fit. Property data for sodium is much more abundant and was compared between different source to evaluate their agreement. This was not possible for gallium.

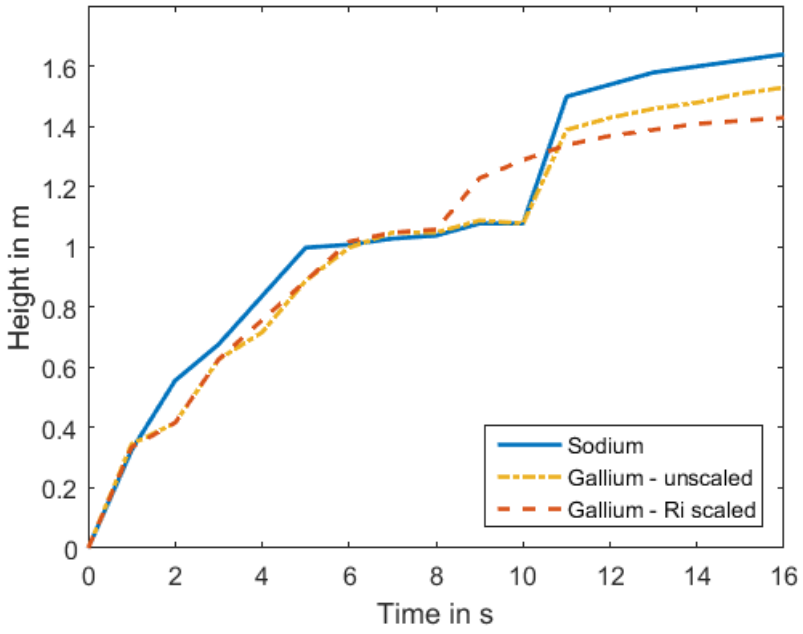

Figure 4.31: Comparison of the vertical position of the stratification interface for sodium and gallium (scaled and unscaled) as coolants for Case 2.

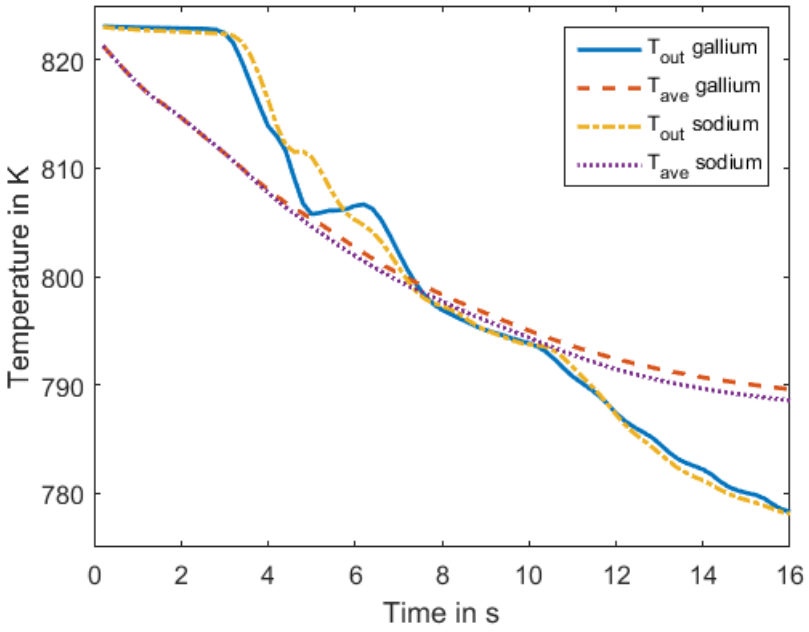

Figure 4.32: Comparison of the change of average temperature, and mass flow averaged outlet temperature for Case 2 using sodium and gallium as coolants.

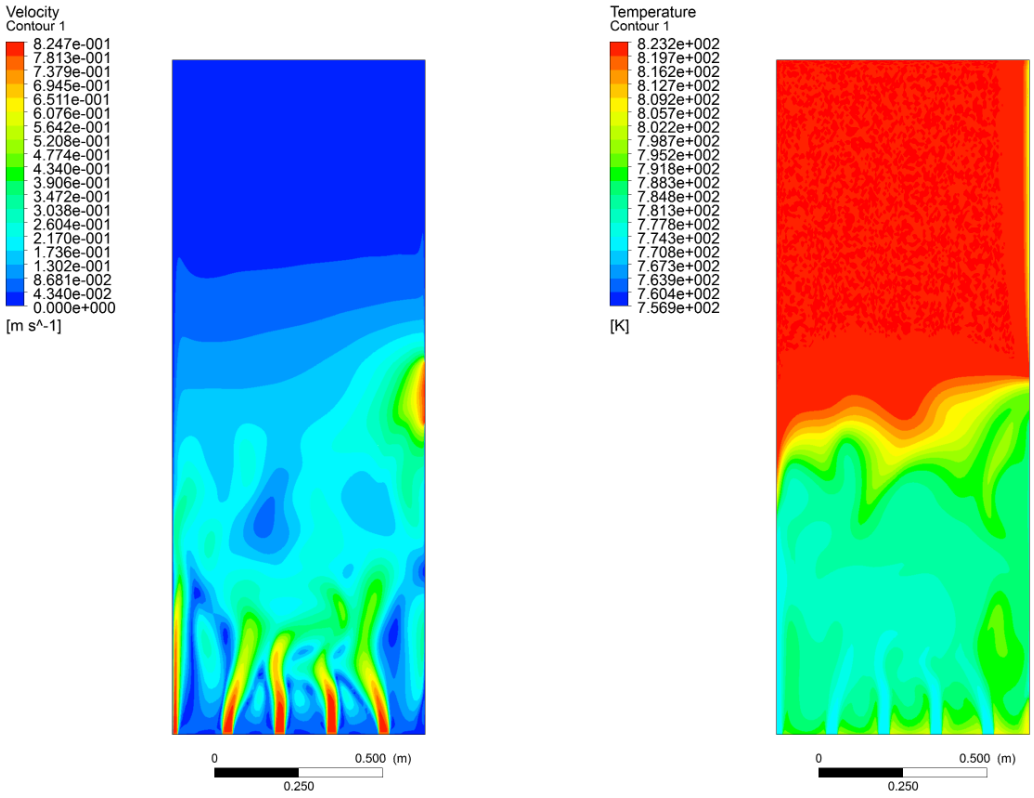

Figure 4.33: Velocity and temperature contours after five seconds for Case 2 using gallium without scaling.

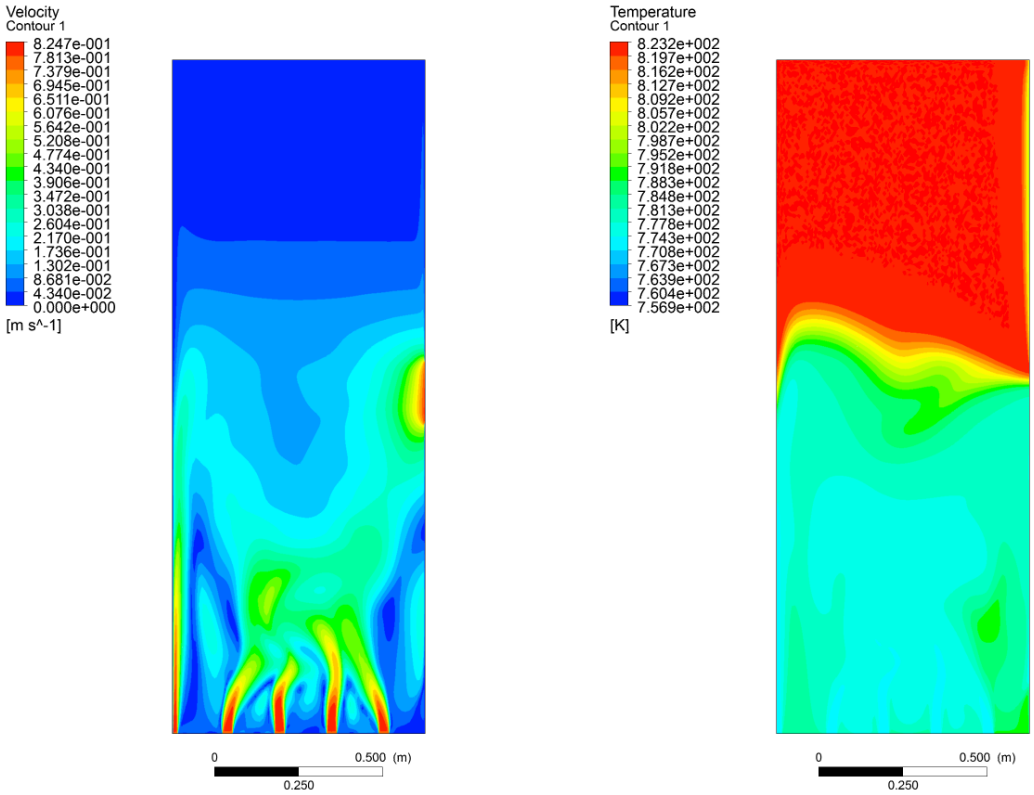

Figure 4.34: Velocity and temperature contours after eight seconds for Case 2 using gallium without scaling.

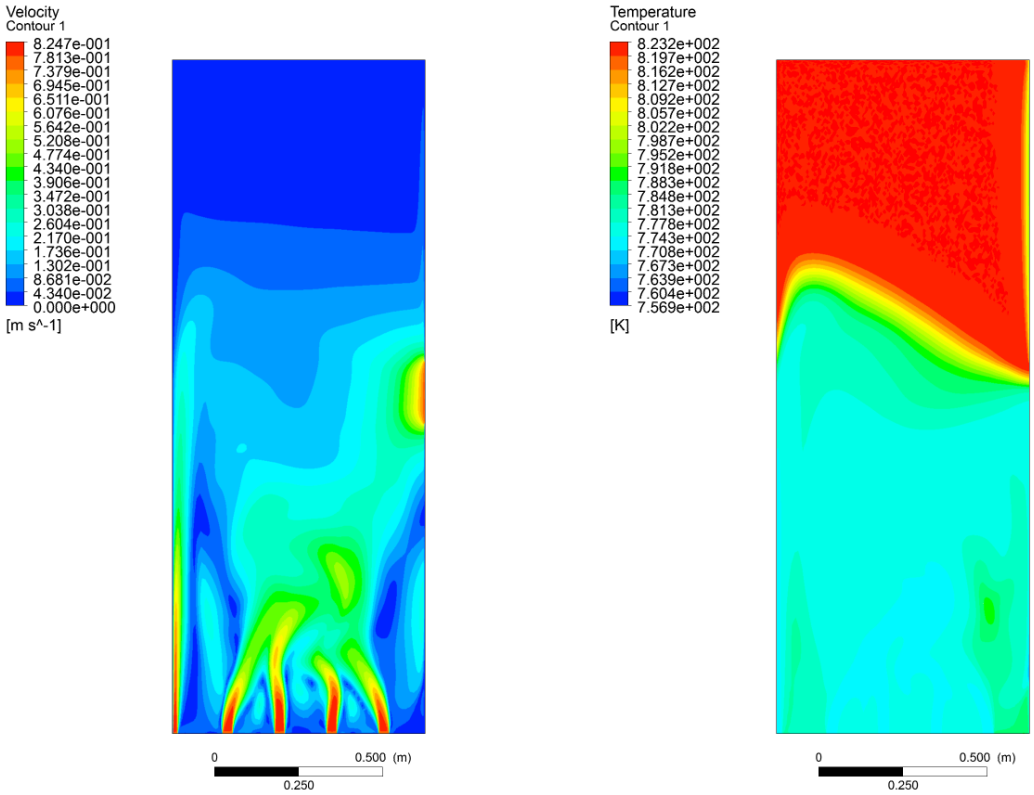

Figure 4.35: Velocity and temperature contours after ten seconds for Case 2 using gallium without scaling.

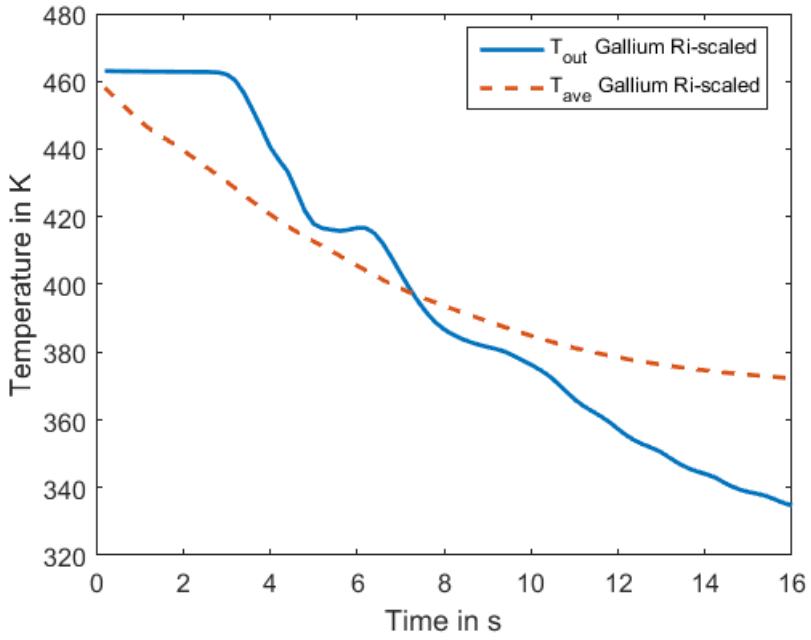

Figure 4.36: Change of average temperature, and mass flow averaged outlet temperature for Case 2 using gallium with temperatures scaled by Richardson number.

4.4.3 Case 3

Design 3 eliminates three of the 4.5 nozzles in Design 2, further increasing the inlet velocity to 2.33 m/s. The eliminated nozzles are the 1st, 3rd, and 4th full nozzles counted from the left edge. The jets in this case are so strong that no stratification occurs. The flow instead assumes the buoyancy solution as described in Section 4.2. A hot spot develops in the middle of the enclosure and remains there for well over 200 s. The magnitude of the hot spot gradually decreases until it is only slightly above the inlet temperature, as indicated by the scale in Figures 4.37 to 4.42. Figure 4.43 shows the maximum, average, and outlet temperatures over the course of 200 seconds. Both the average temperature and mass-averaged outlet temperature decrease quickly. The mass flow averaged outlet temperature essentially reaches its steady state value after 50 seconds. However, it oscillates with an amplitude of over 20 Kelvin during the first 15 seconds. These oscillations are due to flow instabilities that appear while steady flow is established. After about 15 seconds the outlet temperature is consistently below the average temperature of the enclosure because the inlet flow bypasses much of the hotter fluid once steady flow is established. The average temperature changes quickly at first and then slows as the transient progresses. Not only is hot fluid expelled as cold fluid enters the domain, heat transfer between the hot initial fluid and the incoming fluid is more pronounced when the temperature difference is large. As the maximum temperature declines after about 10 seconds, the driving force for the heat transfer from hot to cold fluid also decreases.

It should be noted that after fifty seconds, the hottest point in the domain is found in the middle of the enclosure and is completely surrounded by colder fluid. Since there is no contact between the hot fluid and the walls, the effect on the pool structure is minimized. However, the quick change in temperature at the beginning of the transient can lead to significant structural concerns. Especially the top half of the enclosure experiences a rapid change in temperature from the initial value of 823.15 K to about 790 K. This change can lead to high thermal stresses in the material in these areas.

Hot Fluid Into Cold Pool

An additional simulation was conducted on Design 3 reversing the thermal boundary conditions on the inlet and stagnant fluid. In this case, the enclosure is initially at 773.15 K and sodium at 823.15 K enters the domain at the bottom. The hot sodium entering is less dense than the ambient sodium and thus rises to the top. The inlet jet has positive buoyancy which reinforces the jet. The contour plots in Appendix C show that the flow patterns are similar for the hot into cold, and cold into hot simulations. The velocity contours match up very well and show a clockwise flow path from the nozzles to the outlet. The temperature contours reveal that the temperature differences persist longer for the injection of hot fluid into a cold pool. The hot fluid seems to leave the enclosure at higher rates than the cold fluid in the reverse case. This is likely due to the negative buoyancy in the cold injection case that leads the flow to "overshoot" the outlet. The flow with 1.5 nozzles thus seems to be dominated by inertial effects rather than buoyancy.

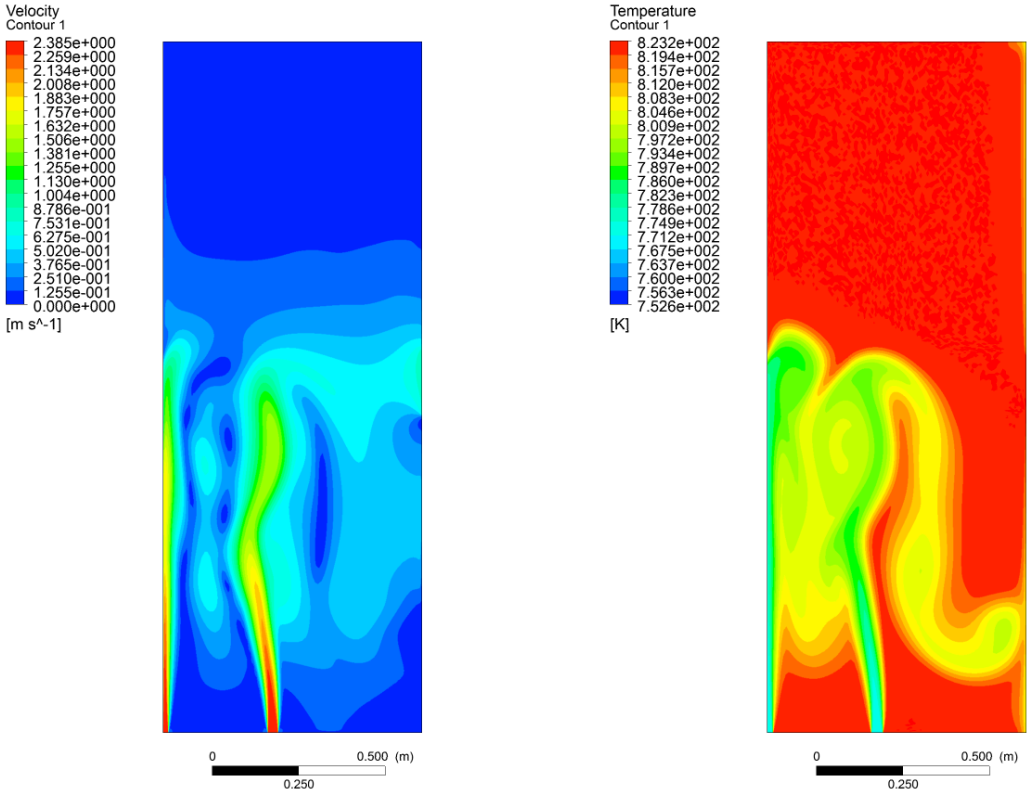

Figure 4.37: Velocity and temperature contours after two seconds for Case 3.

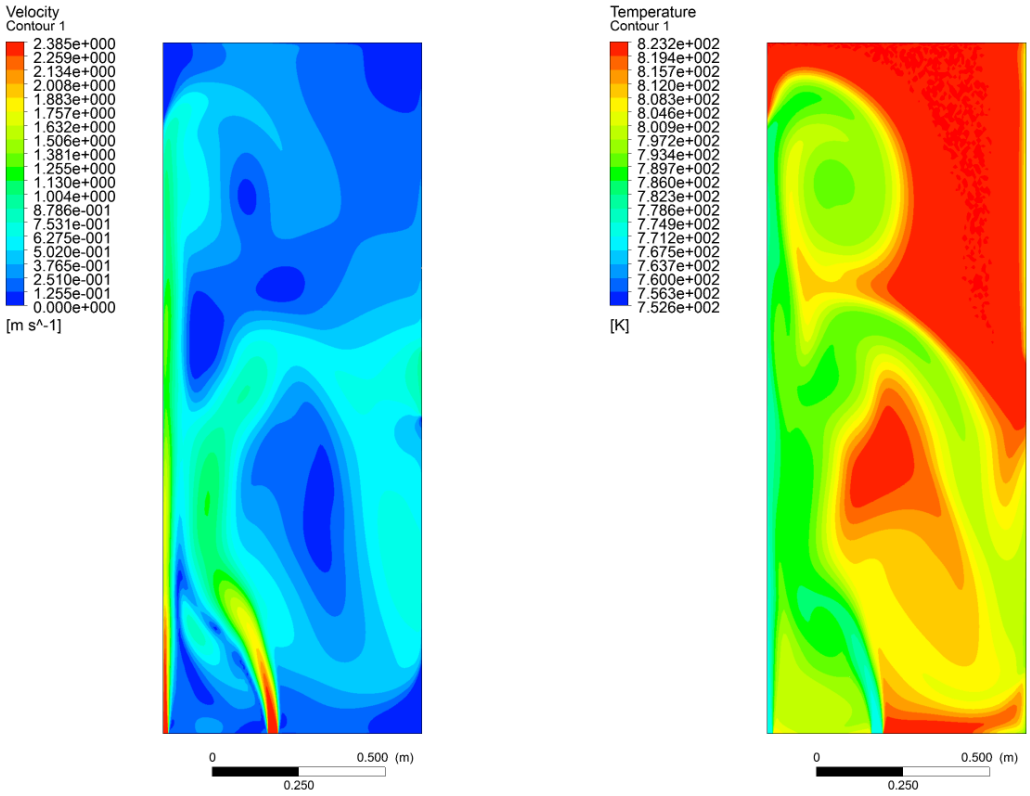

Figure 4.38: Velocity and temperature contours after five seconds for Case 3.

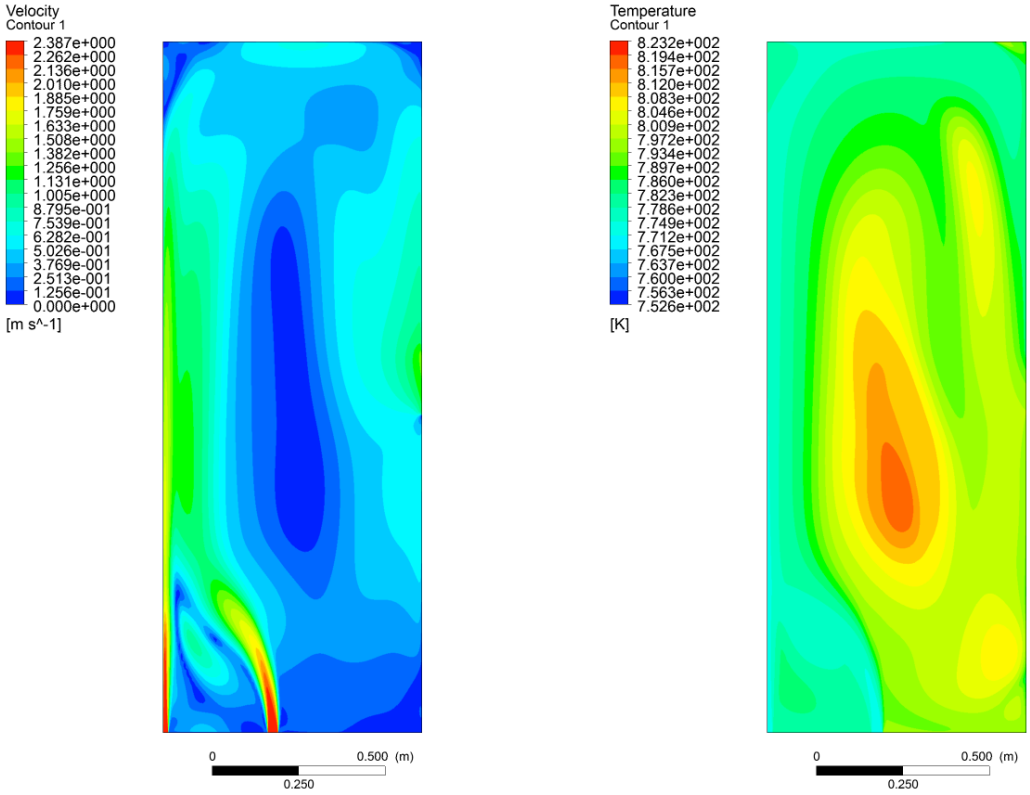

Figure 4.39: Velocity and temperature contours after ten seconds for Case 3.

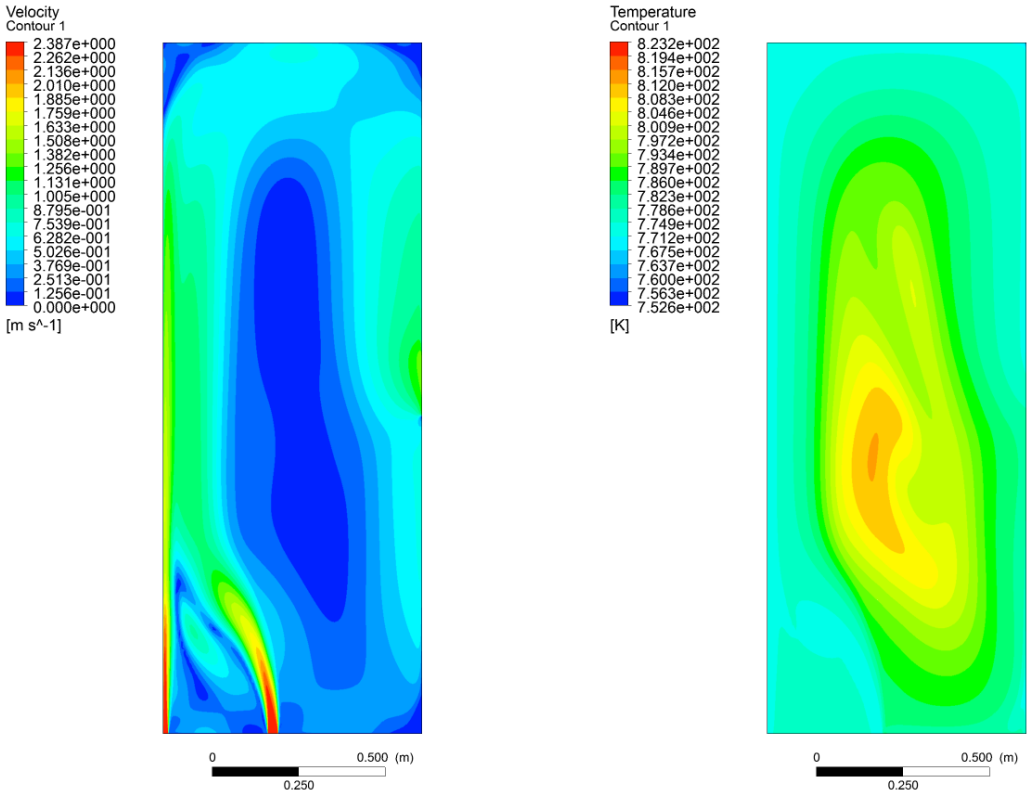

Figure 4.40: Velocity and temperature contours after twenty seconds for Case 3.

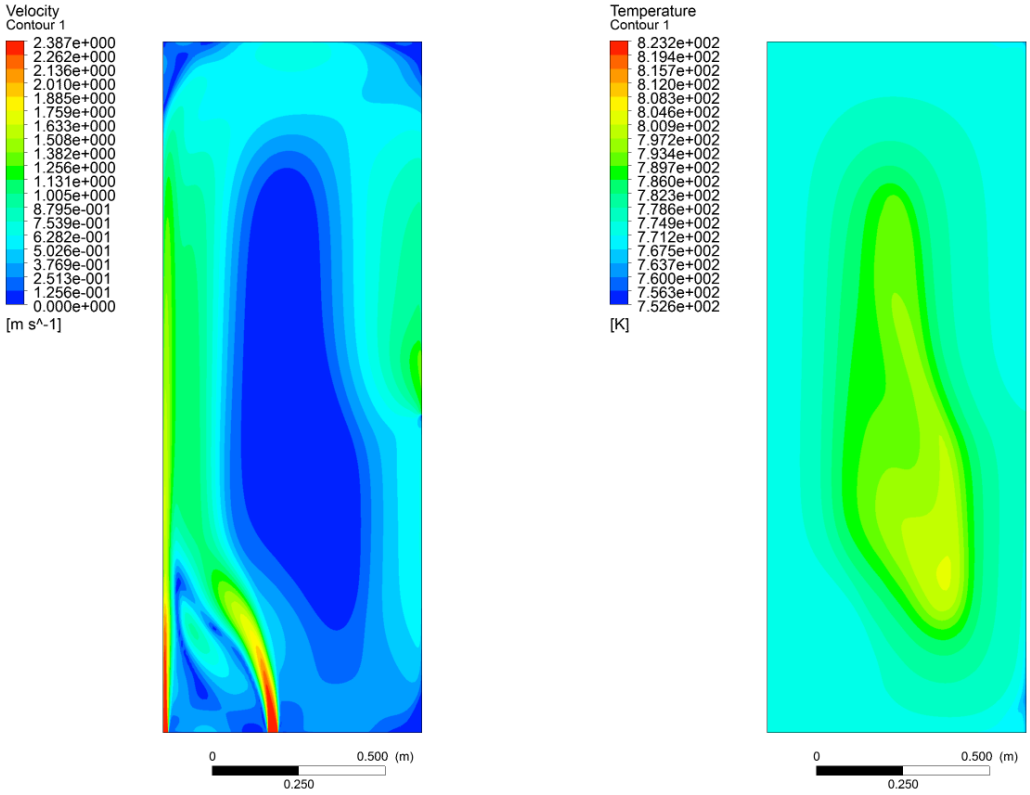

Figure 4.41: Velocity and temperature contours after fifty seconds for Case 3.

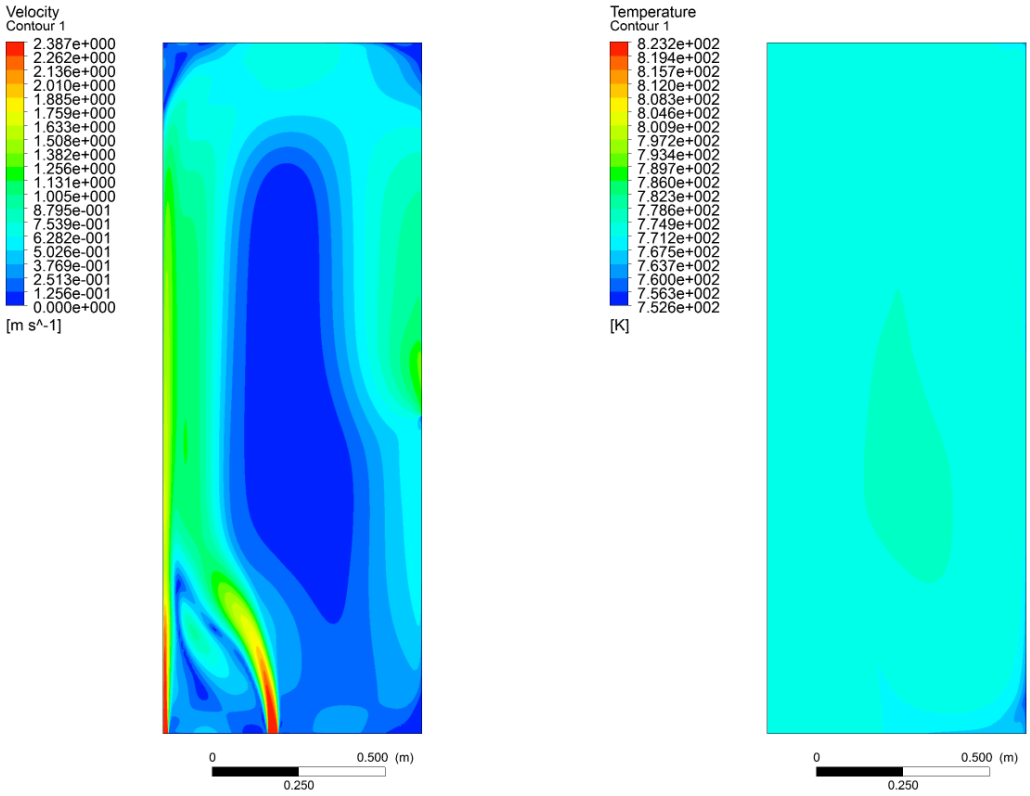

Figure 4.42: Velocity and temperature contours after two hundred seconds for Case 3.

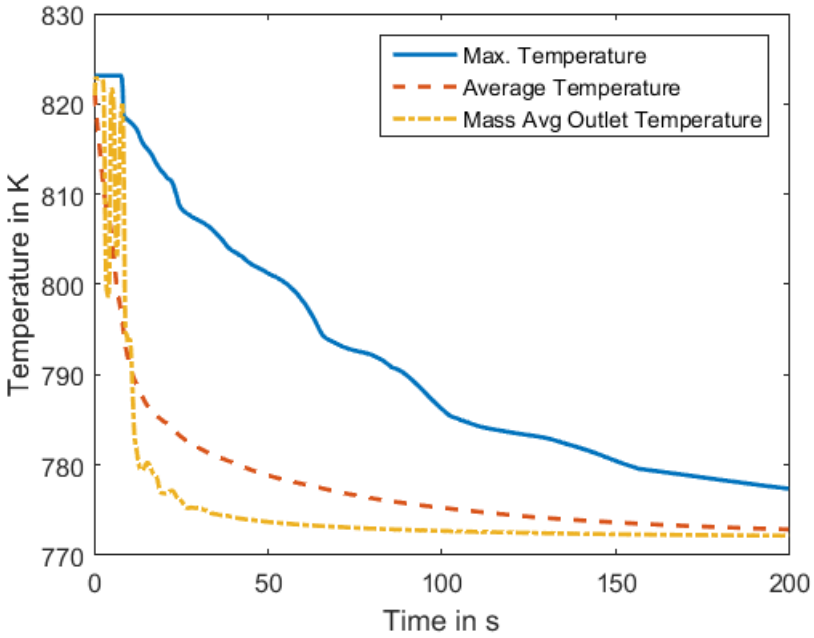

Figure 4.43: Change of maximum temperature, average temperature, and mass flow averaged outlet temperature of the upper plenum for Case 3.

4.5 Full Transient

A final simulation was performed on Design 2 studying the effect of variable inlet conditions that more closely reflect accident conditions. The inlet temperature profile was approximated from the Unprotected Loss of Flow (ULOF) accident analysis performed by Grady et al. [63]. The temperature peaks at 1103.15 K after approximately 100 seconds, and reaches a steady value of 823.15 K after 1300 seconds. The flow rate decays exponentially with a flow halving time of 10 seconds and a final value of 1.5 % of the starting velocity of 0.186 m/s. The steady state value was chosen slightly more conservative than the 2 to 3 % suggested by Tenchine et al. [65]. To reduce the high computational cost of the simulation, the mesh was changed to Mesh 3. Further, the time step was increased to 0.002 seconds to advance the solution faster in time. This resulted in residuals on the order of 10^{-4} to 10^{-5} in the continuity equation after the maximum of 40 iterations per time step. Both of these adjustment reduce the quality of the final solution but were deemed necessary to obtain results for a longer transient. It is expected that the simulation will still capture the overall trends of the underlying physics but the quantitative results should be viewed with caution.

At the beginning of the transient, the jets are still strong and are clearly visible in the contour plots of velocity and temperature (Fig. 4.44). The jets are supported by the positive buoyancy they posses. There is also some downward movement along the right side due to the cold walls. The jets completely break down at around 30 seconds due to the reduced flow rate (Fig. 4.45). This time corresponds to three flow halving times resulting in just one eighth of the initial flow rate of 0.186 m/s. After 50 seconds a new flow pattern is established (Fig. 4.46). This pattern creates a circle around the enclosure. The hot inlet flow combines along the bottom and left wall and moves upwards due to its lower density. On the right, cooled wall dense fluid moves downward and is redirected in the right bottom corner. Around the inlet nozzles the redirected cold fluid flows above the hot inlet suppressing the flow from the nozzles. This will likely cause problems in the real reactor because the flow will be largely buoyancy driven. The colder flow from the wall might cause back-flow into the reactor core that would counteract natural circulation.

After 110 seconds the flowrate has decayed to its steady state value and the enclosure becomes stratified as depicted in Fig. 4.47. The interface is much broader than in previous simulations and spans almost the entire height of the enclosure. Relatively hot sodium reaches the top of the enclosure via a wall jet on the left side. Cold fluid from the wall descends along the right wall. As the transient progresses, inlet temperatures start to decrease thus reducing the buoyancy of the jet on the left wall. After 200 s, the contours clearly show a slower jet. At 350 seconds the incoming fluid is not hot enough to rise to the top of the plenum. Comparison of the temperature for the jet and ambient fluid reveals that the incoming fluid rises higher than its thermal equilibrium height. This is due to the momentum of the jet. It is also evident, that the plenum continues to fill up from the top.

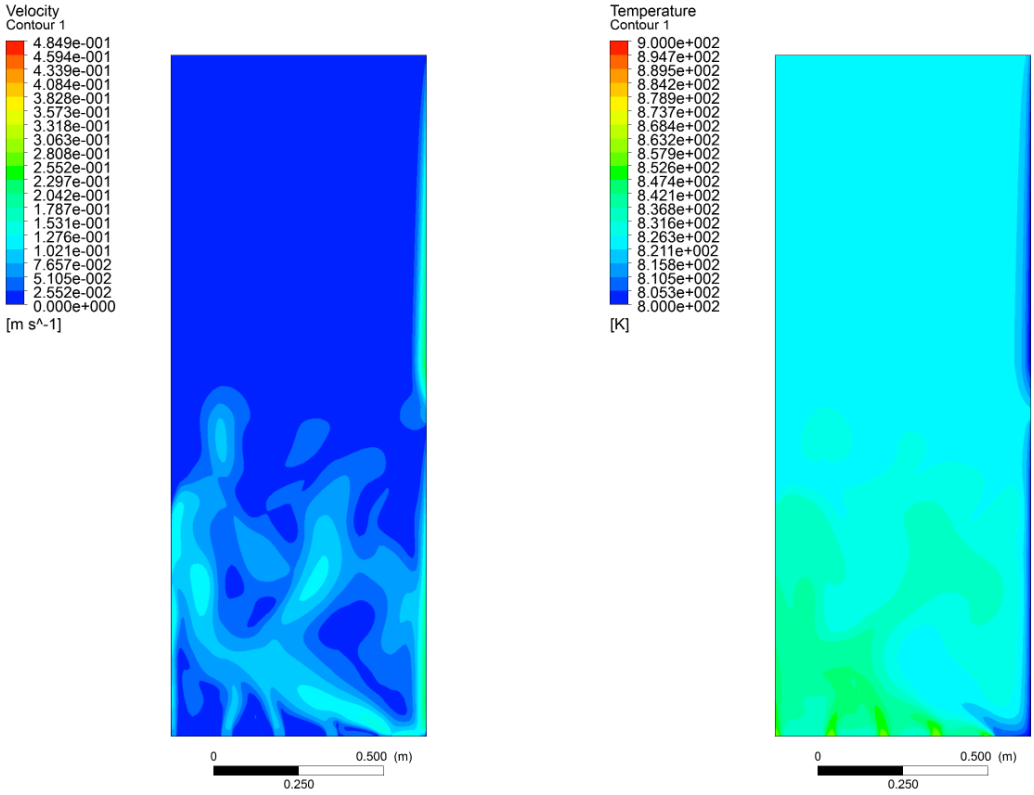

Figure 4.44: Velocity and temperature contours after 15 seconds for the ULOF scenario.

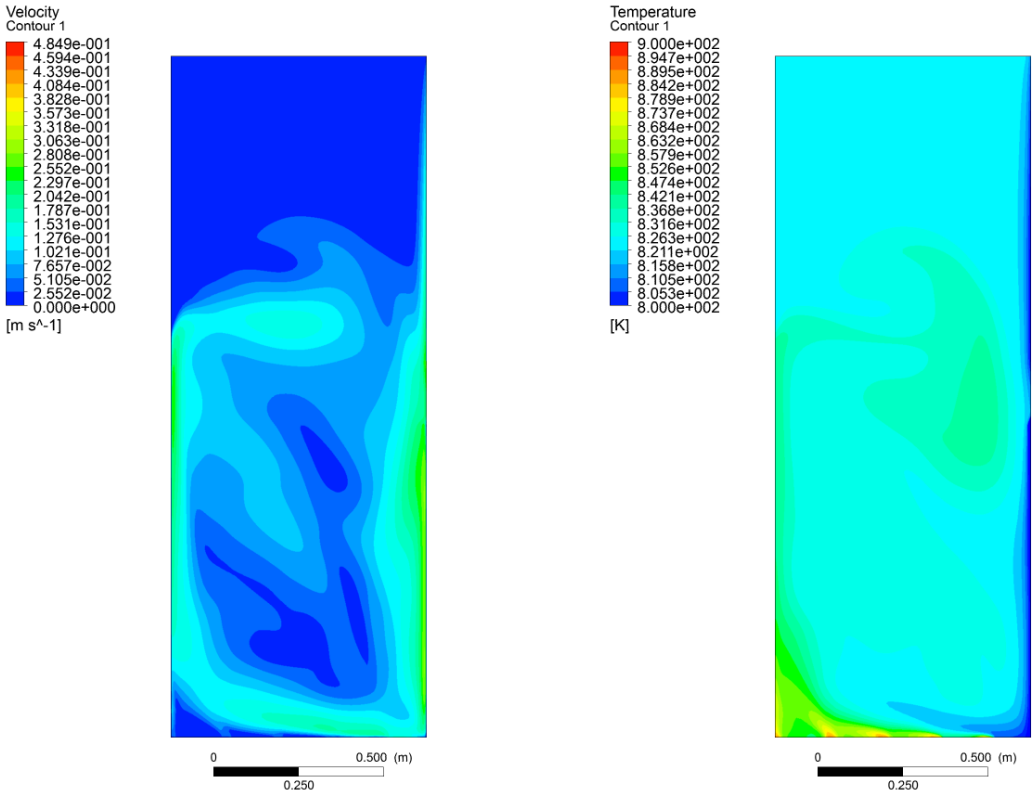

Figure 4.45: Velocity and temperature contours after 30 seconds for the ULOF scenario.

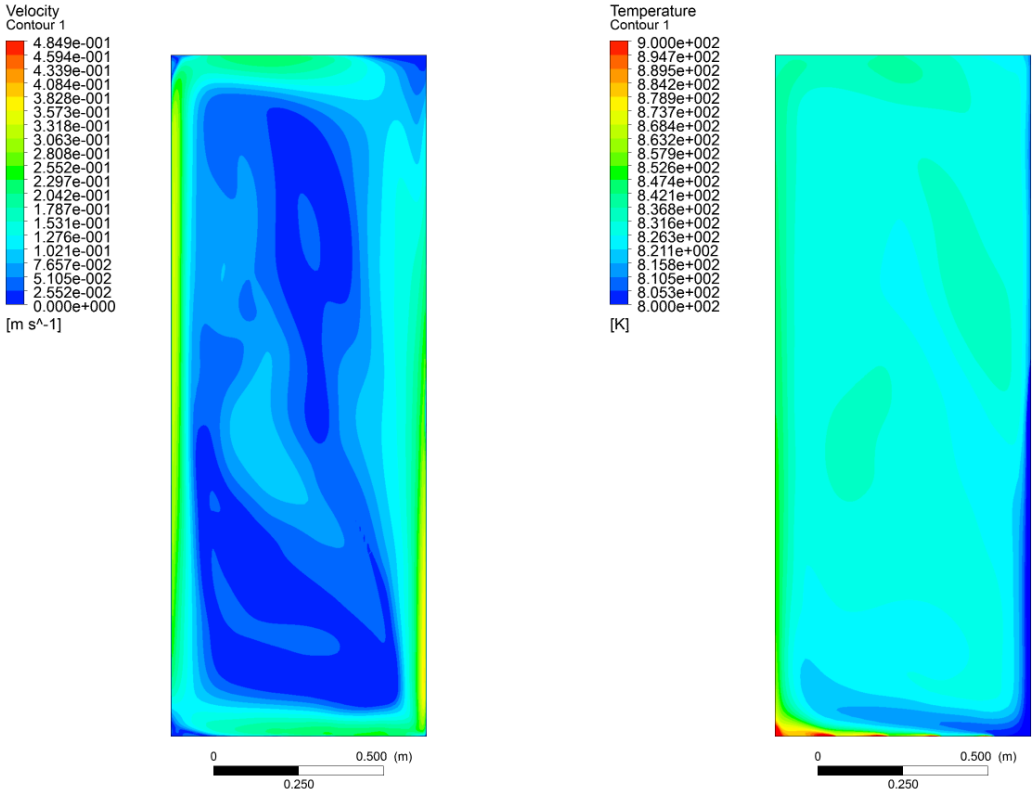

Figure 4.46: Velocity and temperature contours after 50 seconds for the ULOF scenario.

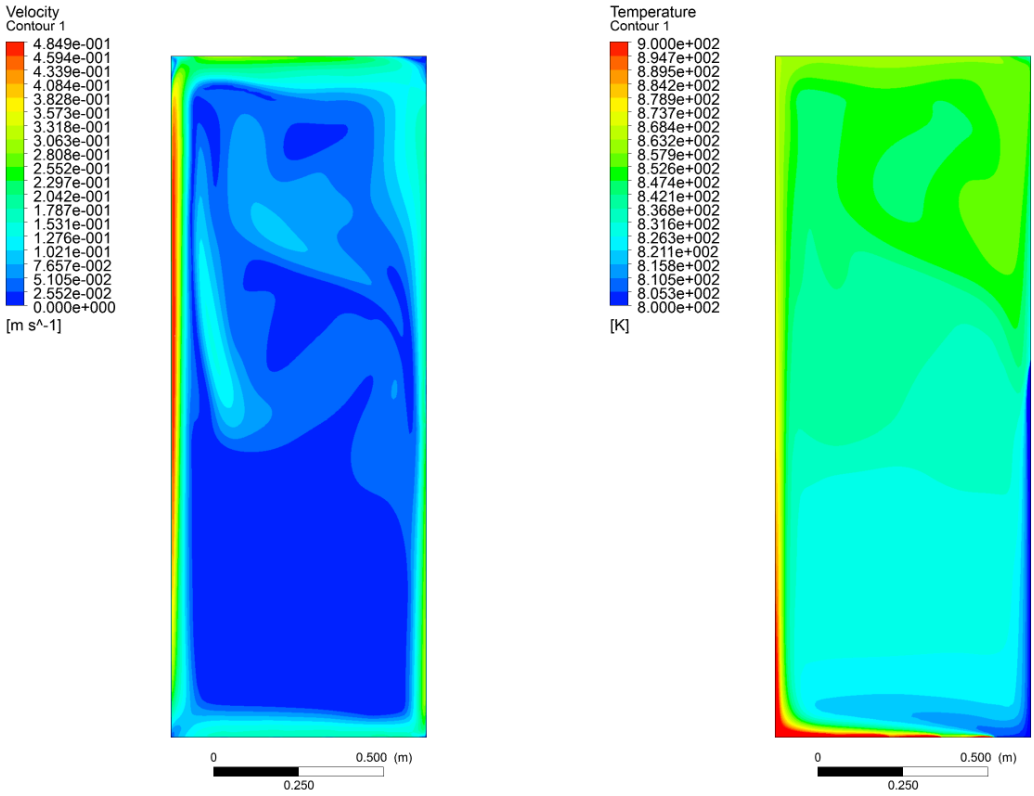

Figure 4.47: Velocity and temperature contours after 110 seconds for the ULOF scenario.

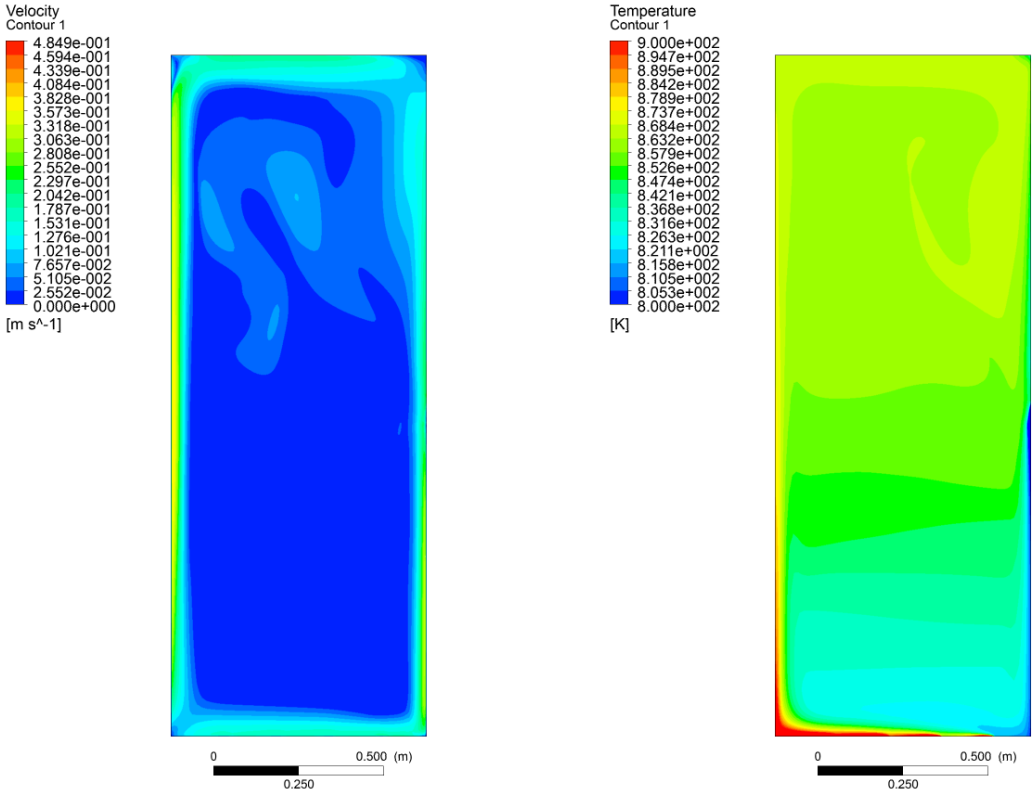

Figure 4.48: Velocity and temperature contours after 200 seconds for the ULOF scenario.

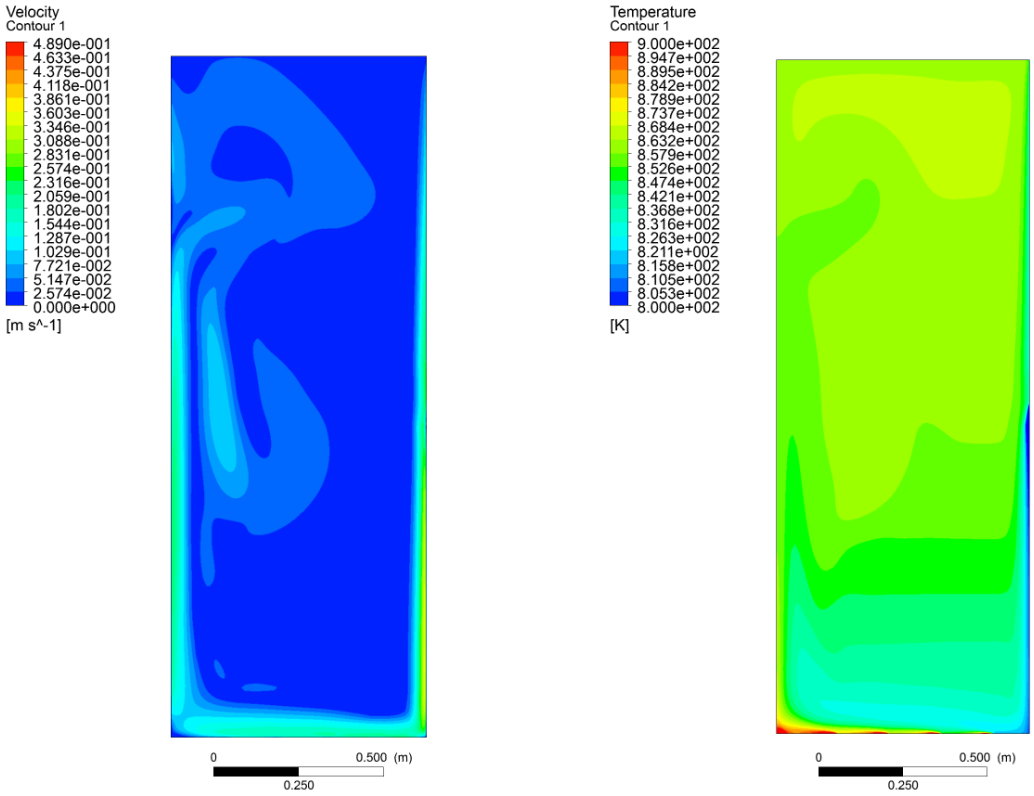

Figure 4.49: Velocity and temperature contours after 350 seconds for the ULOF scenario.

5 Analysis

5.1 Simple Transient

The results from the three cases for the simple transient show that the inlet velocity has a large influence on the stratification behavior of the upper plenum. Higher velocities lead to higher jets that do not allow a stratification interface to form. Jets from lower velocity inlets carry less momentum and are more easily stopped by the stratification layer. The results for Case 2 show clearly that the jet height increases as the stratification interface moves upward. The large jet on the left side is able to push the stratification interface upwards but it does not break through. The interface moves up more quickly for higher inlet velocities which results in a faster decrease of the average, maximum, and outlet temperatures.

The high temperature gradients present in stratified pools place significant thermal stresses on the reactor materials. These stresses can lead to failures that result in long and costly outages, or at the very least require frequent inspection. These inspections are complicated by the opaque nature of sodium. Case 3 leads to rapid temperature changes along the left and right walls. The reactor will likely feature core instrumentation equipment in this area of steep temperature gradients. Furthermore, it is expected that a cold layer will form on the right wall because it is adjacent to the relatively cooler heat exchanger. This layer will decrease the amount of thermal shock experienced by the wall in the case of a cold injection into a hot pool but will have the reverse effect if hot fluid is injected into a cold pool.

The upper core structure mentioned in the previous paragraph will also alter the flow path of incoming fluid in the reactor. From the simulations conducted for the IAEA benchmark on Monju, it can be inferred that an upper core structure would divert the flow obliquely. This diversion will slow the flow which increases the likelihood of stratification. The proposed test stand will allow for the inclusion of upper core structures to study their influence. It is recommended to conduct further simulations on this matter.

The comparison between the simulations using wall and symmetry boundary conditions shows that the general trends remain the same for both options. The average and outlet temperatures agree well for both cases. However, the stratification interface moves more quickly for the symmetry boundary than for the wall boundary for the first 10 seconds. After that the interface for the wall boundary is significantly elevated compared to the other case. These differences will have to be taken into account when translating the experimental results from the test stand to the reactor prototype.

Further differences between the test stand and the reactor will be introduced by the choice of coolant. As the scaled gallium simulation showed, the interface rises slower compared to the sodium simulation and is about 20 cm lower at times above 10 seconds. The results show that the trends in average temperature and mass-averaged outlet temperature are well captured by both sodium and gallium simulations. Overall, care will be required when transferring results from the test stand to the actual reactor.

5.1.1 Stratification Prediction

Peterson has conducted significant research into stratified volumes including analytical derivations to describe and predict stratification behavior [61, 66]. Peterson's focus is on gas spaces and large water pools (see Figure 5.1) but the results are expected to hold for liquid sodium flows as well. Scaling parameters by Peterson were also used to size the proposed sodium test loop [61].

Peterson developed Eqn. 5.1 to predict whether or not a volume is stably stratified. The equation can be derived from the non-dimensionalized vorticity transport equation if the following criteria are met [66]:

- the entrainment Richardson number is large compared to one,

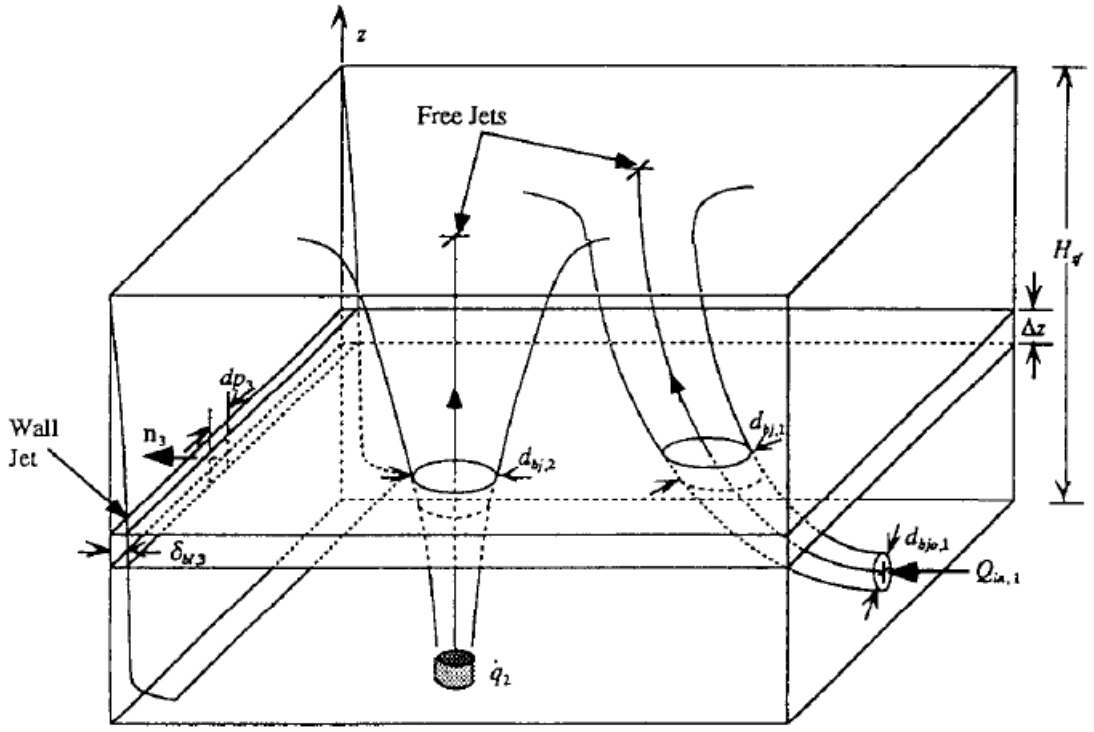

Figure 5.1: Schematic of the geometries considered by Peterson. Reprinted from [66] with permission from Elsevier.

- the inverse of the entrainment Reynolds number is small compared to the Richardson number,
- density and temperature gradients in the horizontal directions can be neglected.

$$Ri_{eH} = \frac{(\rho_a - \rho_0)gH_{sf}}{\rho_a u_e^2} = 16\frac{(\rho_a - \rho_0)gH_{sf}}{\rho_a U_0^2}\left(\frac{H_{sf}}{d_{bj0}}\right)^2\left(1 + \frac{d_{bjo}}{4\sqrt{2}\alpha_T H_{sf}}\right)^2 >> 1 \tag{5.1}$$

In Eqn. 5.1 H_{sf} is the fluid height, d_{bjo} is the inlet nozzle diameter, ρ_a and ρ_0 are the ambient density and injected fluid density, g is the gravitational acceleration, U_0 is the inlet velocity, and α_T is Taylor's entrainment constant. Based on comparison with experimental results, Peterson suggests 16 as the critical Richardson number above which stratification occurs. A similar equation was provided by Jirka [66]:

$$\frac{H_{sf}}{d_{bjo}}\frac{1}{0.22}\left(\frac{(\rho_a - \rho_0)g d_{bjo}}{\rho_a U_0^2}\right)^{1/2} > 1 \tag{5.2}$$

The above equations have been altered from their original form to yield a positive density difference (ie. reversing ρ_a and ρ_0). The correlations by Peterson, and Jirka et al. were derived for three dimensional volumes and jets. To improve the accuracy of the prediction, Peterson's derivation was replicated for a two dimensional volume as shown in Figure 5.2. According to Paillat and Kaminski the entrainment can be described by Eqn. 5.3 where Q is the flow rate per unit depth (see Eqn. 5.4), M is the momentum flux per unit depth (see Eqn. 5.5), α_{th} is the so called "top hat" entrainment constant, U_0 is the inlet velocity, and w_0 is the width of the inlet [67].

$$\frac{dQ}{dz} = 2\alpha_{th}\frac{M}{Q} \tag{5.3}$$

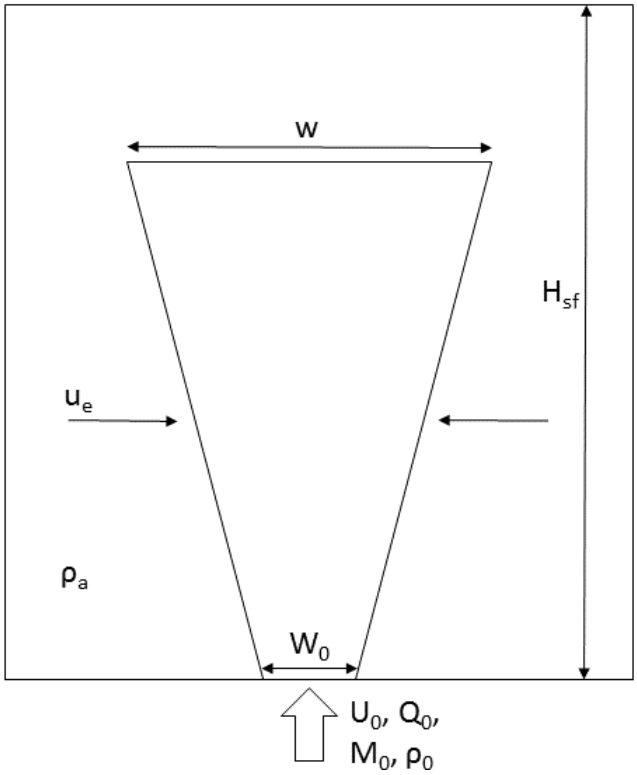

Figure 5.2: Schematic of the two dimensional enclosure considered for the derivation of Eqn. 5.9.

$$Q_0 = U_0 w_0 \tag{5.4}$$

$$M_0 = U_0^2 w_0 \tag{5.5}$$

$$\frac{M_0}{Q_0} = U_0 \tag{5.6}$$

$$\frac{M_0}{Q_0^2} = \frac{1}{w_0} \tag{5.7}$$

If momentum is conserved along the jet then M_0 can be substituted for M. The results from Case 2 with a symmetry and wall boundary condition can be used to verify whether or not this is true. Since the outlet pressure in both cases is set to zero, the inlet pressure gives a measure of the losses occurring in the domain. The pressures are 212.9 and 198.1 Pascal for the wall and symmetry simulation, respectively. The difference of 7 % is small enough to neglect wall friction on the jet. The error introduced by this approximation is likely not sufficient to alter conclusions, and favors the prediction of unstratified conditions. Integrating Eqn. 5.3 over the height of the enclosure, and rearranging yields:

$$Q\frac{dQ}{dz} = 2\alpha_{th} M_0$$

$$\frac{1}{2}\frac{d(Q^2)}{dz} = 2\alpha_{th} M_0$$

$$\int_0^{H_{sf}} \frac{d(Q^2)}{dz} dz = 4\alpha_{th} M_0 \int_0^{H_{sf}} dz$$

$$Q_H^2 - Q_0^2 = 4\alpha_{th} M_0 H_{sf}$$

$$\left(\frac{Q_H}{Q_0}\right)^2 = \frac{4\alpha_{th} M_0 H_{sf}}{Q_0^2} + 1 = \frac{4\alpha_{th} H_{sf}}{w_0} + 1 \tag{5.8}$$

Realizing that $dQ/dz = u_e$ for a two dimensional jet, using Eqn. 5.6, and substituting the result from Eqn. 5.8 into Eqn. 5.3 leads to an expression for the entrainment velocity u_e:

$$\frac{dQ_H}{dz} = u_e = 2\alpha_{th} \frac{M_0}{Q_0} \frac{Q_0}{Q_H} = 2\alpha_{th} U_0 \left(\frac{4\alpha_{th} H_{sf}}{w_0} + 1\right)^{-1/2} \tag{5.9}$$

Finally, expressing Ri_{eH} using the new entrainment velocity yields the stratification criterion for a two dimensional volume:

$$Ri_{eH} = \frac{\rho_a - \rho_0}{\rho_a} \frac{g H_{sf}}{(2\alpha_{th} U_0)^2} \left(\frac{4\alpha_{th} H_{sf}}{w_0} + 1\right) >> 1 \tag{5.10}$$

Peterson's derivation and the derivation presented in this work are derived for a single yet in a large, undisturbed medium. This is not the case for the simulated geometries. Two of the designs feature multiple inlet nozzles, and even the case with one big inlet is expected to be influenced by the walls. To account for some of these differences, all equations will be corrected using the number of nozzles in a full slice geometry. This means two inlets for Case 1, 9 for Case 2, and 3 for Case 3 after accounting for the symmetry plane. Further, the correlations provided by Jirka and Peterson will be evaluated using hydraulic diameters to account for the deviation from a circular jet. Table 5.1 shows the results for the three different correlations.

Cases 1 and 2 are correctly predicted to stratify by all correlations. However, contrary to the simulation results, Jirka's and Peterson's correlations suggest that Case 3 should also be stratified. Both correlations rank this case as the closest to unstratified conditions but ultimately still predict stratification. The newly derived correlation for a two dimensional enclosure correctly predicts that Case 3 does not stratify. The entrainment Richardson numbers for Case 2 and 3 differ by a factor of 3.6 compared to 1.58 by Peterson. The critical Richardson number changes the condition for stratification from an imprecise criterion (>> 1) to a more precise one (> 1) facilitating evaluation. It should be noted that the experimental data was obtained for hot water injection into cold pools and might not be valid for the cases investigated in this work. Even so, the new correlation most strongly indicates that Case 3 should stratify.

Table 5.1: Stratification prediction based on the equations presented in Sect. 5.1.1.

Case	Stratification	Peterson (Eqn. 5.1)		Jirka et al. (Eqn. 5.2)	Eqn. 5.10	
1	yes	78 303		60	414	
2	yes	882		8.3	47	
3	no	560		4.8	13	
Condition for Stratification		>>1	>16†	>1	>>1	>16†

† Critical Richardson number based on experimental data according to Peterson [66]

5.2 Full Transient

The simulation of the full transient reveals a different picture than the simpler transient. The walls are shielded from the stratification by jets that change temperature based on the progression of the transient. The temperature at the top right wall changes by about 50 Kelvin over the first 110 seconds. The stratification interface appears much broader than in previous simulations and has a much lower vertical temperature gradient of less than 10 K/m. The walls have relatively uniform temperatures reducing stresses due to uneven expansion.

A more critical issue in the long transient is the temperature layering that occurs at the inlet after approximately 30 seconds. Cold fluid from the right wall flows on top of the hotter inlet actively counteracting natural circulation from the core. A simulation including the core is likely necessary to determine whether or not the jets have sufficient momentum to prevent backflow. Any reduction in core flow rate would increase the core temperature and reduce the boiling margin. It is critical to maintain a sufficient natural circulation flow rate in the core to prevent this. It should be noted that the cold boundary condition on the right wall might not be accurate as it was determined from simulation results by Chang et al. that are based on a previous iteration of the AFR design [54].

6 Conclusion

In conclusion, numerous simulations were performed to aid in the design of a test loop to evaluate thermal stratification in the upper plenum of the planned Advanced Fast Reactor. The simulations reveal that stratification is strongly influenced by the velocity of the incoming fluid. Two of the three simulated velocities lead to stratified conditions in the upper plenum. The velocity of the third case with only 1.5 inlet nozzles is sufficiently high to establish a jet that reaches the top of the enclosure. This jet prevents the formation of a stable interface.

Although stratification is generally considered detrimental to the structural materials of the reactor, the case without stratification results in very quick temperature changes along the walls during the first few seconds of the simulated transient. These temperature changes will affect the material in similar fashion to a thermal stratification interface. The decision about which design to pursue will require further analysis on the impact on the structures, and include the upper core structure that was neglected in this simulation.

The stratification interface reaches the top of the enclosure in about 130 seconds for Case 2 compared to 700 seconds for Case 1. The interface passes the outlet after 8 seconds for Case 1, and approximately 5 seconds for Case 2. Due to the smaller jet, the flow path is more direct in Case 1 leading to a slower rise after the interface passes the outlet. The heat exchanger inlet temperature reduces to below 783.15 Kelvin (within 10 Kelvin of the inlet temperature) in 11, 13, 12 seconds for Cases 1, 2, and 3, respectively.

Further simulations were performed on Case 2 to evaluate the effect of the boundary conditions on the front and back walls, and of the choice of coolant on the simulation results. A symmetry boundary condition is expected to be closer to the actual reactor. The results for both boundary conditions agree well although the stratification interface shows slightly different behavior, reaching the outlet quicker with a symmetry boundary but then rising more slowly and also showing a smaller jump around the time it reaches the outlet. It seems justified to approximate the full plenum with a slice to capture the essential physics. However, further research will likely be required to develop a precise correlation between test stand and full plenum. The difference in boundary condition between the test stand and actual geometry will result in some error and cannot be neglected.

The rise of the interface is very similar for the simulation that simply switches gallium for sodium. However, if the Richardson number is preserved, the interface experiences a jump earlier compared to the other cases. It also rises more slowly than the other two cases (sodium, gallium unscaled) after that. Although trends seen in the gallium simulation transfer well to the sodium simulation, the differences are significant enough to warrant attention. Qualitatively, a gallium test stand will provide useful information into the underlying physics of the thermal stratification phenomenon. Quantification will likely need to be conducted on a sodium instead of a gallium loop.

Correlations by Peterson and Jirka were used to predict whether or not stratification occurs. Both correlations predicted that all three cases would be stably stratified. While this is true for Cases 1 and 2, Case 3 did not stratify. This shortcoming is likely due to the two dimensional geometry of the investigated plenum compared to the three dimensional structures for which the correlations were derived. Both correlations capture the trend of decreasing stratification tendency going for Case 2 to Case 3. Peterson's derivation was altered to account for a two dimensional enclosure. The new correlation predicts all three cases accurately implying that geometry plays a major role in predicting stratification.

A simulation featuring variable inlet temperature and flow rate was conducted to study the Unprotected Loss of Flow scenario. Stratification was observed after about 100 seconds but the gradients are

much lower than in the simple transient cases. Temperature layering occurs around the inlet that could reduce the natural circulation flow rate and thus reduce core cooling during an accident. It is highly recommend that this scenario receives further attention.

Finally, it can be concluded that the inlet velocity has a large influence on the stratification behavior of the upper plenum. Higher velocities suppress stratification. The movement of the stratification layer is complex and cannot easily be related to the inlet velocity. The simulations showed that gallium can be substituted for sodium in a test loop to capture the essential physics of the problem. However, quantitative results cannot be translated easily even when flow conditions are scaled by Richardson number. A new correlation was derived to predict stratification and was successfully verified against the simulation data.

Appendix

Appendix A

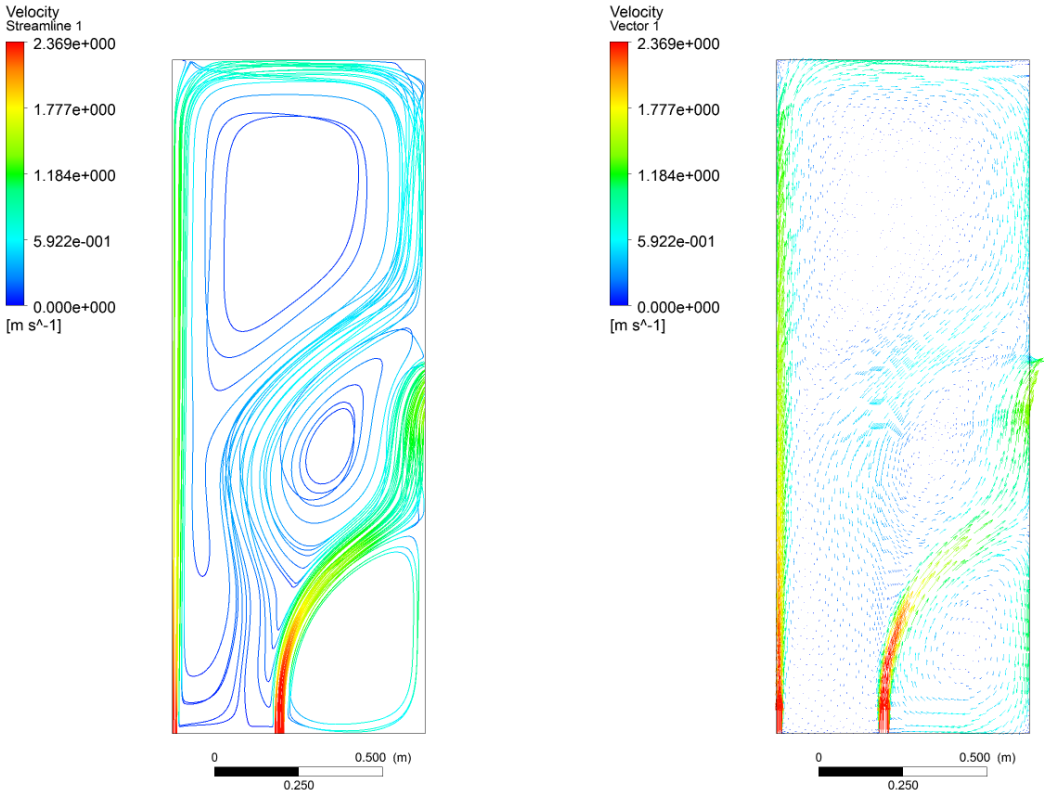

Figure A.1: Streamlines (left) and velocity vectors (right) for the steady flow case with heat losses after 160 seconds

Appendix B

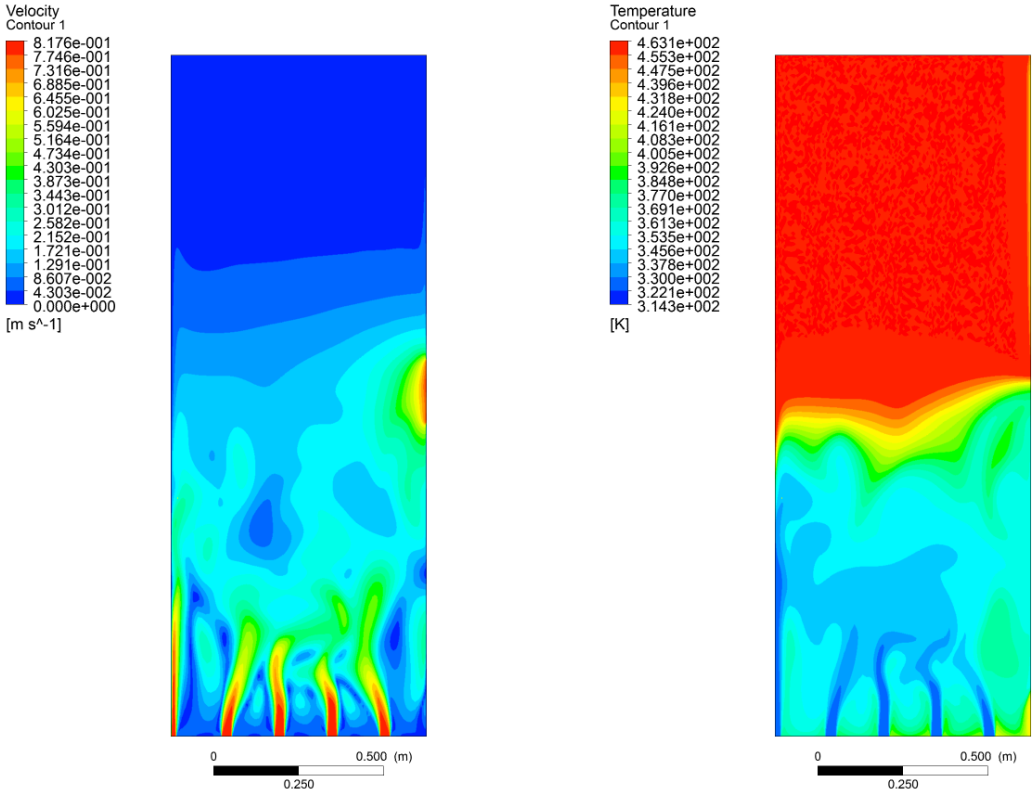

Figure B.1: Velocity and temperature contours after five seconds for the scaled simulation using gallium.

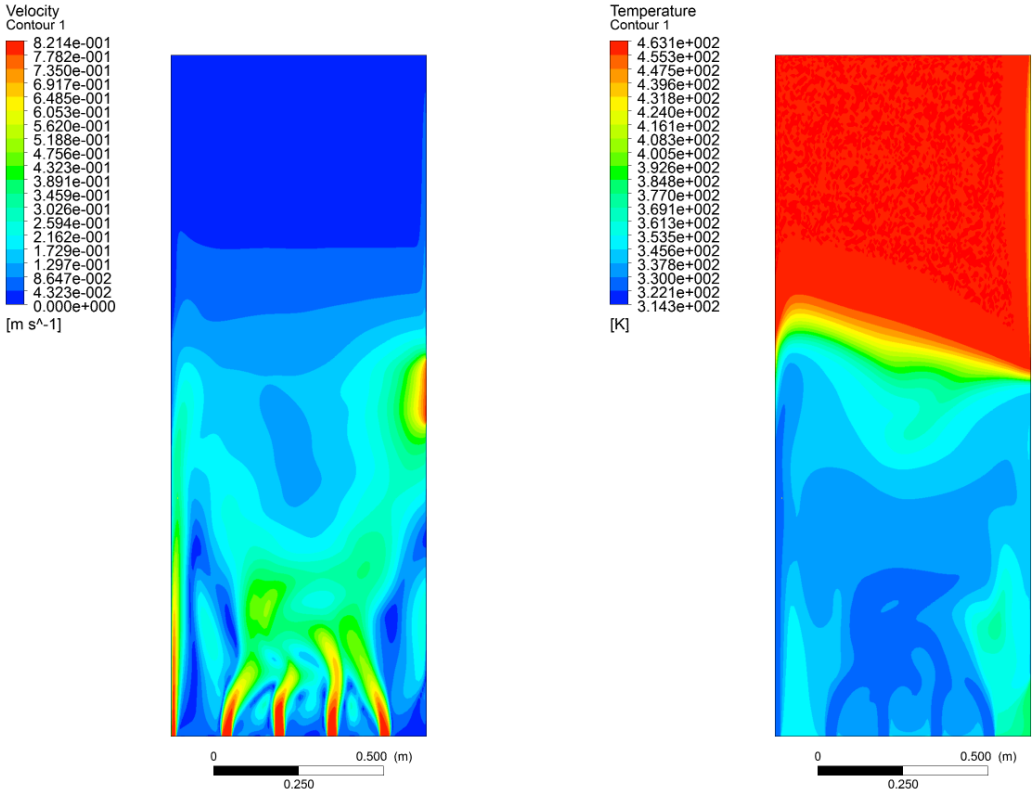

Figure B.2: Velocity and temperature contours after eight seconds for the scaled simulation using gallium.

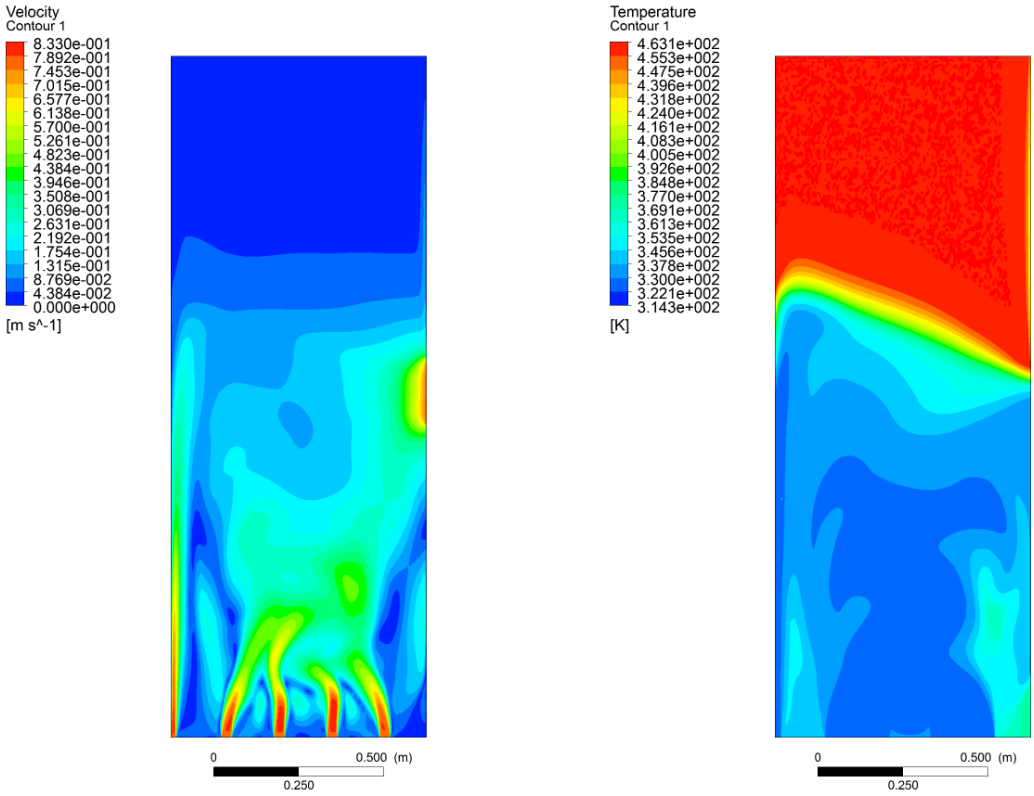

Figure B.3: Velocity and temperature contours after ten seconds for the scaled simulation using gallium.

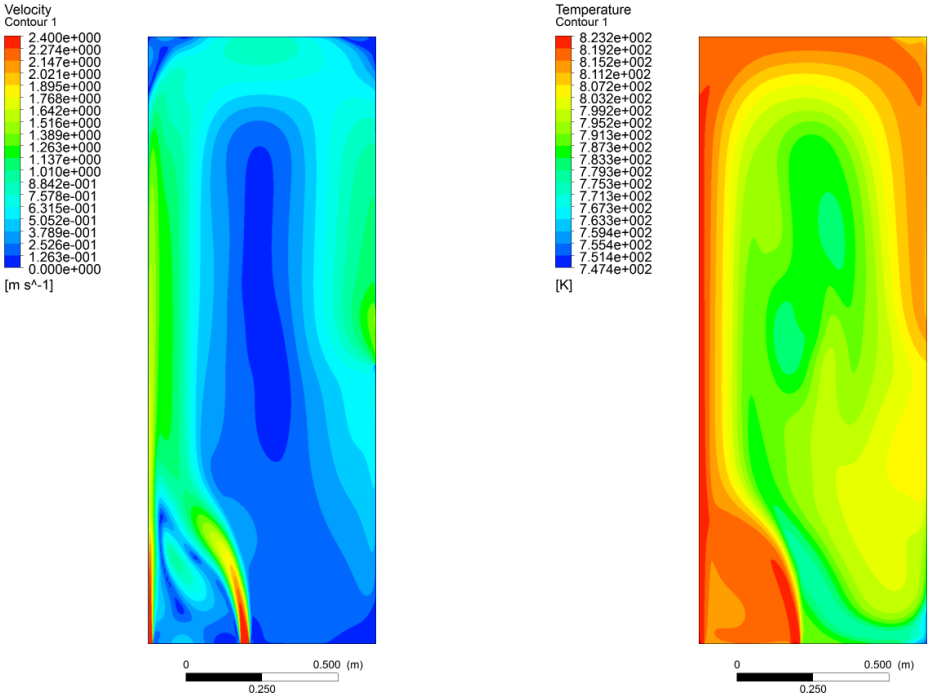

Figure C.1: Velocity and temperature contours after ten seconds for injection of hot fluid into a cold pool with 1.5 nozzles.

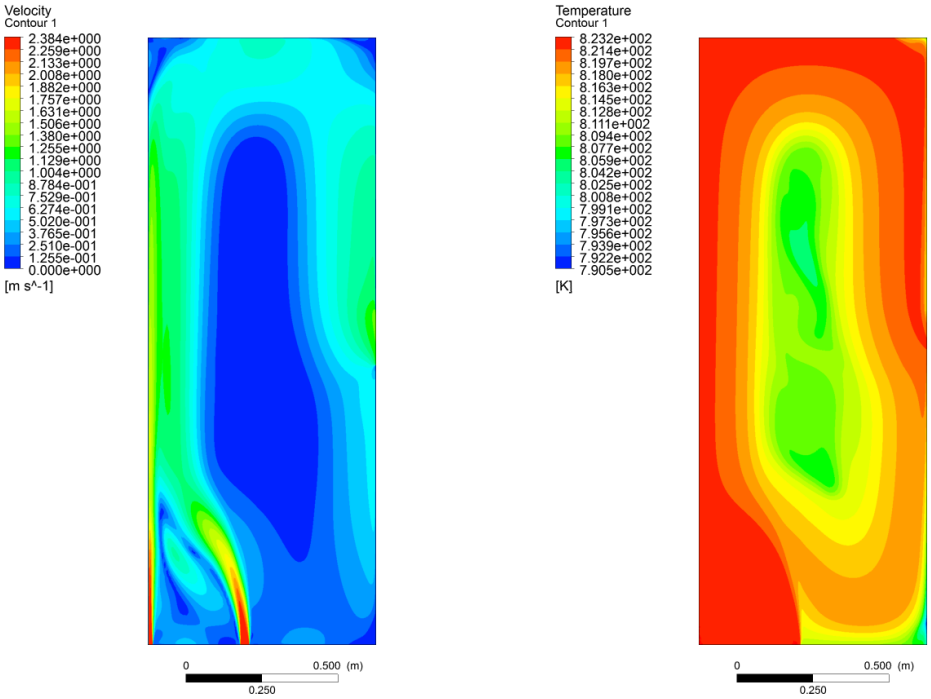

Figure C.2: Velocity and temperature contours after 96 seconds for injection of hot fluid into a cold pool with 1.5 nozzles.

References

[1] N. Apergis and J. E. Payne, "A dynamic panel study of economic development and the electricity consumption-growth nexus," *Energy Economics*, vol. 33, pp. 770–781, Sept. 2011.

[2] S. Niu, Y. Jia, W. Wang, R. He, L. Hu, and Y. Liu, "Electricity consumption and human development level: A comparative analysis based on panel data for 50 countries," *International Journal of Electrical Power & Energy Systems*, vol. 53, pp. 338–347, Dec. 2013.

[3] R. K. Pachauri, M. R. Allen, V. R. Barros, J. Broome, W. Cramer, R. Christ, J. A. Church, L. Clarke, Q. Dahe, P. Dasgupta, and others, "Climate Change 2014: Synthesis Report. Contribution of Working Groups I, II and III to the Fifth Assessment Report of the Intergovernmental Panel on Climate Change," tech. rep., IPCC, Geneva, Switzerland, 2014.

[4] "Energy and Climate Change," tech. rep., International Energy Agency, 2015.

[5] United Nations Framework Convention on Climate Change, "Paris Agreement," Dec. 2015.

[6] "Key World Energy Statistics 2015," tech. rep., International Energy Agency, 2015.

[7] T. M. L. Wigley, "Coal to gas: The influence of methane leakage," *Climatic Change*, vol. 108, pp. 601–608, Oct. 2011.

[8] J. Bouchard, "The French fast breeder reactor program," *Atomic energy*, vol. 109, no. 5, pp. 299–308, 2011.

[9] "Nuclear Technology Review 2015," tech. rep., International Atomic Energy Agency, Vienna, 2015.

[10] A. Dalla Valle and C. Furlan, "Diffusion of nuclear energy in some developing countries," *Technological Forecasting and Social Change*, vol. 81, pp. 143–153, Jan. 2014.

[11] C. Grandy, T. Kim, E. Jin, M. Farmer, H. Belch, J. Grudzinski, T. Sumner, Y. Momozaki, L. Krajtl, C. Gerardi, and others, "Advanced Fast Reactor-100-Design Overview," in *Fast Reactors and Related Fuel Cycles: Safe Technologies and Sustainable Scenarios (FR13). COMPANION CD-ROM. Proceedings of an International Conference*, 2013.

[12] J. E. Earp, "Briefing: Small modular reactors," *Proceedings of the ICE - Energy*, vol. 166, pp. 53–57, May 2013.

[13] J. Vuji, R. M. Bergmann, R. Škoda, and M. Mileti, "Small modular reactors: Simpler, safer, cheaper?," *Energy*, vol. 45, pp. 288–295, Sept. 2012.

[14] D. Bodansky, *Nuclear Energy: Principles, Practices, and Prospects*. New York: Springer, 2nd ed ed., 2004.

[15] M. Fjaestad, "Fast Breeder Reactors in Sweden: Vision and Reality," *Technology and culture*, vol. 56, no. 1, pp. 86–114, 2015.

[16] "PRIS - Country Details USA." `https://www.iaea.org/PRIS/CountryStatistics/CountryDetails.aspx?current=US`.

[17] "PRIS - Country Details Germany." `https://www.iaea.org/PRIS/CountryStatistics/CountryDetails.aspx?current=DE`.

[18] "PRIS - Miscellaneous reports - Nuclear Share." `https://www.iaea.org/PRIS/WorldStatistics/NuclearShareofElectricityGeneration.aspx`.

[19] U. Nestle, "Does the use of nuclear power lead to lower electricity prices? An analysis of the debate in Germany with an international perspective," *Energy Policy*, vol. 41, pp. 152–160, Feb. 2012.

[20] J. R. Lamarsh and A. J. Baratta, "4 - Nuclear Reactors and Nuclear Power," in *Introduction to Nuclear Engineering*, Addison-Wesley series in nuclear science and engineering, Upper Saddle River, N.J: Prentice Hall, 3rd ed ed., 2001.

[21] T. B. Cochran, H. A. Feiveson, W. Patterson, G. Pshakin, M. V. Ramana, M. Schneider, T. Suzuki, and F. von Hippel, "Fast breeder reactor programs: History and status," tech. rep., International Panel on Fissile Materials, 2010.

[22] "Ux Prices." `https://www.uxc.com/p/prices/UxCPrices.aspx`.

[23] P. Chellapandi, P. V. Rao, and P. Kumar, "Fast reactor programme in India," *Pramana*, vol. 85, no. 3, pp. 525–538, 2015.

[24] P. Hejzlar, N. E. Todreas, E. Shwageraus, A. Nikiforova, R. Petroski, and M. J. Driscoll, "Cross-comparison of fast reactor concepts with various coolants," *Nuclear Engineering and Design*, vol. 239, pp. 2672–2691, Dec. 2009.

[25] S. Chetal, V. Balasubramaniyan, P. Chellapandi, P. Mohanakrishnan, P. Puthiyavinayagam, C. Pillai, S. Raghupathy, T. Shanmugham, and C. S. Pillai, "The design of the Prototype Fast Breeder Reactor," *Nuclear Engineering and Design*, vol. 236, pp. 852–860, Apr. 2006.

[26] G. Kessler, "6 Breeder Reactors With a Fast Neutron Spectrum," in *Sustainable and Safe Nuclear Fission Energy*, Power Systems, Berlin, Heidelberg: Springer Berlin Heidelberg, 2012.

[27] C. Grandy, J. J. Sienicki, A. Moisseytsev, L. Krajtl, M. T. Farmer, T. K. Kim, and B. Middleton, "Advanced Fast Reactor-100 (AFR-100) Report for the Technical Review Panel," tech. rep., Argonne National Laboratory (ANL), 2014.

[28] "Benchmark analyses of sodium natural convection in the upper plenum of the Monju reactor vessel : Final report of a coordinated research project 2008–2012," Tech. Rep. IAEA-TECDOC-1754, International Atomic Energy Agency, Vienna, 2014.

[29] J. R. Lamarsh and A. J. Baratta, "6 - Nuclear Reactor Theory," in *Introduction to Nuclear Engineering*, Addison-Wesley series in nuclear science and engineering, Upper Saddle River, N.J: Prentice Hall, 3rd ed ed., 2001.

[30] J. D. Anderson Jr, *Computational Fluid Dynamics : The Basics with Applications*. New York: McGraw-Hill, 1995.

[31] F. Moukalled, L. Mangani, and M. Darwish, "5 The Finite Volume Method," in *The Finite Volume Method in Computational Fluid Dynamics*, vol. 113 of *Fluid Mechanics and Its Applications*, Cham: Springer International Publishing, 2016.

[32] S.-K. Choi and S.-O. Kim, "Turbulence modeling of natural convection in enclosures: A review," *Journal of Mechanical Science and Technology*, vol. 26, pp. 283–297, Jan. 2012.

[33] F. R. Menter, "Improved two-equation k-omega turbulence models for aerodynamic flows," 1992.

[34] F. R. Menter, "Review of the shear-stress transport turbulence model experience from an industrial perspective," *International Journal of Computational Fluid Dynamics*, vol. 23, pp. 305–316, Apr. 2009.

[35] D. Tenchine, D. Pialla, T. Fanning, J. Thomas, P. Chellapandi, Y. Shvetsov, L. Maas, H.-Y. Jeong, K. Mikityuk, A. Chenu, H. Mochizuki, and S. Monti, "International benchmark on the natural convection test in Phenix reactor," *Nuclear Engineering and Design*, vol. 258, pp. 189–198, May 2013.

[36] M. Shibahara, T. Takata, and A. Yamaguchi, "Numerical analysis of thermal stratification in the reactor upper plenum of MONJU with 13 sector and full sector models," in *The 14th International Topical Meeting on Nuclear Reactor Thermal Hydraulics*, (Toronto, Canada), 2011.

[37] H. Mochizuki and H. Yao, "Analysis of thermal stratification in the upper plenum of the "Monju" reactor," *Nuclear Engineering and Design*, vol. 270, pp. 48–59, Apr. 2014.

[38] H. Yao, J. Riberaud, and H. Mochizuki, "CFD computation of thermal stratification in the upper plenum of Monju reactor," in *Fast Reactors and Related Fuel Cycles: Safe Technologies and Sustainable Scenarios (FR13). COMPANION CD-ROM. Proceedings of an International Conference*, 2015.

[39] H. Ohira, U. B. Xu, U. Bieder, K. Velusamy, H. Mochizuki, S. Choi, Y. Shvetsov, T. Sofu, J. Thomas, S. Monti, S. Yoshikawa, and A. Stanculescu, "Benchmark analyses of sodium natural convection in the upper plenum of the MONJU reactor vessel," in *Int. Conf. Fast Reactors and Related Fuel Cycles: Safe Technologies and Sustainable Scenarios–FR*, 2013.

[40] T. Sofu and J. Thomas, "Analysis of Thermal Stratification in the Upper Plenum of the Monju Reactor Vessel," in *The 14th International Topical Meeting on Nuclear Reactor Thermalhydraulics*, (Toronto, Canada), September 25-30, 2011.

[41] M. Shibahara, T. Takata, and A. Yamaguchi, "Numerical simulation of dynamic flow structure and thermal stratification phenomena in LMFBR," in *Proceedings of the 19th International Conference on Nuclear Engineering*, (Chiba, Japan), 2011.

[42] U. Bieder and G. Fauchet, "Analysis of the Natural Convection Flow in the Upper Plenum of the MONJU Reactor with Trio_U," *Science and Technology of Nuclear Installations*, vol. 2013, pp. 1–11, 2013.

[43] T. Sofu, "Parametric Analysis of Thermal Stratification during the Monju Turbine Trip Test," in *Proceedings of ICAPP '12*, (Chicago, USA), pp. 779–789, June 24-28 2012.

[44] H. Ohira, K. Honda, and M. Sotsu, "Numerical Simulations of Upper Plenum Thermal-Hydraulics of Monju Reactor Vessel Using High Resolution Mesh Models," *Journal of Energy and Power Engineering*, vol. 7, no. 4, p. 679, 2013.

[45] T. Sakamoto, M. Shibahara, T. Takata, and A. Yamaguchi, "Numerical study of three dimensional thermal hydraulics effect on thermal stratification phenomena in upper plenum of MONJU," in *Proc. Korea-Japan Symposium on Nuclear Thermal Hydraulics and Safety*, (Chuncheon, Korea), 2010.

[46] T. Muramatsu and H. Ninokata, "Investigation of turbulence modelling in thermal stratification analysis," *Nuclear Engineering and Design*, vol. 150, pp. 81–93, Sept. 1994.

[47] S. Ohno, H. Ohki, A. Sugahara, and H. Ohshima, "Validation of a Computational Simulation Method for Evaluating Thermal Stratification in the Reactor Vessel Upper Plenum of Fast Reactors," *Journal of Nuclear Science and Technology*, vol. 48, pp. 205–214, Feb. 2011.

[48] S.-K. Choi and S.-O. Kim, "Treatment of turbulent heat fluxes with the elliptic-blending second-moment closure for turbulent natural convection flows," *International Journal of Heat and Mass Transfer*, vol. 51, pp. 2377–2388, May 2008.

[49] S.-K. Choi, T.-H. Lee, Y.-I. Kim, and D. Hahn, "Numerical Analysis of Thermal Stratification in the Upper Plenum of the Monju Fast Reactor," *Nuclear Engineering and Technology*, vol. 45, pp. 191–202, Apr. 2013.

[50] M. Shibahara, T. Takata, and A. Yamaguchi, "Numerical study on thermal stratification phenomena in upper plenum of LMFBR "MONJU"," *Nuclear Engineering and Design*, vol. 258, pp. 226–234, May 2013.

[51] Y. Liu, "Experimental Investigation of Thermal Stratification Phenomenon in Liquid Metal Pool," 2016.

[52] N. Tanaka, S. Moriya, and A. Wada, "Thermal-hydraulic characteristics in a liquid-metal fast breeder reactor hot plenum," *Nuclear science and engineering*, vol. 88, no. 3, pp. 445–463, 1984.

[53] D.-H. Hahn, Y.-I. Kim, C.-B. Lee, S.-O. Kim, J.-H. Lee, Y.-B. Lee, B.-H. Kim, and H.-Y. Jeong, "Conceptual design of the sodium-cooled fast reactor KALIMER-600," *Nuclear Engineering and Technology*, vol. 39, no. 3, pp. 193–206, 2007.

[54] Y. Chang, P. Finck, C. Grandy, J. Cahalan, L. Deitrich, F. Dunn, D. Fallin, M. Farmer, T. Fanning, T. Kim, and others, "Advanced Burner Test Reactor Preconceptual Design Report," Tech. Rep. ANL-ABR-1, Argonne National Laboratory (ANL), 2006.

[55] Y.-i. Kim, Y. B. Lee, C. B. Lee, J. Chang, and C. Choi, "Design Concept of Advanced Sodium-Cooled Fast Reactor and Related R&D in Korea," *Science and Technology of Nuclear Installations*, vol. 2013, pp. 1–18, 2013.

[56] Y. Chang, P. LoPinto, M. Konomura, J. Cahalan, F. Dunn, M. Farmer, L. Krajtl, A. Moisseytsev, Y. Momozaki, J. Sienicki, and others, "Small Modular Fast Reactor Design Description," Tech. Rep. ANL-SMFR-1, Argonne National Laboratory (ANL), Argonne, IL (US), 2005.

[57] S. Yoshikawa and M. Minami, "Data description for coordinated research project on benchmark analyses of sodium natural convection in the upper plenum of the MONJU reactor vessel under supervisory of technical working group on fast reactors, International Atomic Energy Agency," tech. rep., Japan Atomic Energy Agency, Tokai (Ibaraki), Japan, 2009.

[58] G. Srinivasan, K. Suresh Kumar, B. Rajendran, and P. Ramalingam, "The Fast Breeder Test Reactor—Design and operating experiences," *Nuclear Engineering and Design*, vol. 236, pp. 796–811, Apr. 2006.

[59] P. Chellapandi, P. Puthiyavinayagam, V. Balasubramaniyan, S. Ragupathy, V. Rajanbabu, S. Chetal, and B. Raj, "Design concepts for reactor assembly components of 500MWe future SFRs," *Nuclear Engineering and Design*, vol. 240, pp. 2948–2956, Oct. 2010.

[60] A. E. Waltar, D. R. Todd, P. V. Tsvetkov, and others, *Fast Spectrum Reactors*. Springer, 2012.

[61] P. F. Peterson, V. E. Schrock, and R. Greif, "Scaling for integral simulation of mixing in large, stratified volumes," *Nuclear engineering and design*, vol. 186, no. 1, pp. 213–224, 1998.

[62] A. Inc., *Fluent User's Guide*. 2016.

[63] C. Grandy, T. K. Kim, E. Jin, M. Farmer, H. Belch, J. Grudzinski, T. Sumner, Y. Momozaki, L. Krajtl, C. Gerardi, and others, "A 100 MWe Advanced Sodium-cooled Fast Reactor (AFR-100)," 2013.

[64] V. Bobkov, L. Fokin, E. Petrov, V. Popov, V. Rumiantsev, and A. Savvatimsky, "Thermophysical Properties of Materials for Nuclear Engineering: A Tutorial and Collection of Data," tech. rep., International Atomic Energy Agency, Vienna, 2008.

[65] D. Tenchine, D. Pialla, P. Gauthé, and A. Vasile, “Natural convection test in Phenix reactor and associated CATHARE calculation,” *Nuclear Engineering and Design*, vol. 253, pp. 23–31, Dec. 2012.

[66] P. F. Peterson, “Scaling and analysis of mixing in large stratified volumes,” *International Journal of Heat and Mass Transfer*, vol. 37, pp. 97–106, 1994.

[67] S. Paillat and E. Kaminski, “Second-order model of entrainment in planar turbulent jets at low Reynolds number,” *Physics of Fluids*, vol. 26, p. 045110, Apr. 2014.